TECHNICAL UNIVERSITY OF CRETE

DIPLOMA THESIS

Development of a Diagnostic Tool for Identifying Non-Adjacent Broken Bars in Industrial Cage Motors

---

Author:
Marios Salinas

Thesis Committee:
Assoc. Prof. Konstantinos Gyftakis
(Supervisor)
Asst. Prof. Georgios Peppas
Dr. Panagiotis Panagiotou

School of Electrical and Computer Engineering

October 3, 2024

ΠΟΛΥΤΕΧΝΕΙΟ ΚΡΗΤΗΣ

Διπλωματική Εργασία

Ανάπτυξη Διαγνωστικής Μεθόδου για Ανίχνευση μη Γειτονικών Σπασμένων Μπαρών σε Βιομηχανικούς Κινητήρες Κλωβού

Συγγραφέας:
Μάριος Σαλίνας

Εξεταστική Επιτροπή:
Αναπλ. Καθ. Κωνσταντίνος Γυφτάκης (Επιβλέπων)
Επίκ. Καθ. Γεώργιος Πέππας
Δρ. Παναγιώτης Παναγιώτου

Σχολή Ηλεκτρολόγων Μηχανικών και Μηχανικών Υπολογιστών

3 Οκτωβρίου 2024

TECHNICAL UNIVERSITY OF CRETE

Abstract

Development of a Diagnostic Tool for Identifying Non-Adjacent Broken Bars in Industrial Cage Motors

Rotor electrical faults, particularly the progressive degradation of rotor cage bars in induction motors, pose significant threats to both operational efficiency and safety. Early detection is critical to prevent costly downtime and mitigate safety risks. However, traditional diagnostic methods, such as Motor Current Signature Analysis (MCSA) during steady-state operation, often fail to identify non-adjacent broken bars. Although transient analysis during motor start-up can effectively detect such faults, it is impractical in many industrial applications where motors run continuously with infrequent start-ups. To overcome this limitation, this study presents a novel fault detection technique that focuses on identifying non-adjacent broken rotor bars by analysing zero-sequence stray flux during steady-state operation, collected through external flux leakage sensors strategically placed in a symmetrical arrangement.

The research is based on extensive simulations of a 1.1 MW induction motor, commonly used in industrial settings, under various load levels and fault scenarios. The study includes healthy motors, as well as motors with faults such as one broken bar, two adjacent broken bars, and two non-adjacent broken bars at half pole pitch. Simulations of the aforementioned cases were conducted using FEM software (Simcenter MAGNET) at a sample rate of 5kHz. The simulated data was then post-processed using MATLAB to accurately diagnose each fault condition and to thoroughly analyse the behaviour of non-adjacent bar breakages.

TECHNICAL UNIVERSITY OF CRETE

Abstract

Development of a Diagnostic Tool for Identifying Non-Adjacent Broken Bars in Industrial Cage Motors

Τα ηλεκτρικά σφάλματα ρότορα είναι συνηθισμένα προβλήματα που εμφανίζονται στους επαγωγικούς κινητήρες, παρουσιάζοντας συχνά βλάβες οι οποίες αργούν να γίνουν καταστροφικές. Λόγω της φύσης αυτού του τύπου βλαβών, η έγκαιρη ανίχνευση τους είναι κρίσιμη για να αποφευχθεί η δαπανηρή διακοπή λειτουργίας τους, αλλά και οποιοσδήποτε κίνδυνος ασφάλειας. Εστιάζοντας σε θραύσεις μπαρών κλωβού του ρότορα βρισκόμενες μη-γειτονικά, οι συνέπειες της βλάβης ενδέχεται να μην εμφανιστούν με την εφαρμογή παραδοσιακών διαγνωστικών μεθόδων που χρησιμοποιούν την ανάλυση χαρακτηριστικών ρεύματος στάτη κατά την λειτουργία του κινητήρα στη μόνιμη κατάσταση. Παρόλα αυτα, η ανάλυση του κινητήρα κατά την εκκίνηση χρησιμοποιώντας την ίδια μέθοδο, θα μπορούσε να σημάνει αξιόπιστα αποτελέσματα, αλλά υπάρχουν πολυάριθμες βιομηχανικές εφαρμογές οπού οι κινητήρες δεν υφίστανται συχνές εκκινήσεις. Ως εκ τούτου, στην παρούσα έρευνα παρουσιάζεται μια νέα τεχνική ανίχνευσης βλαβών για μη-γειτονικές σπασμένες μπάρες, βασισμένη στην ανάλυση της μαγνητικής ροής μηδενικής ακολουθίας κατά τη μόνιμη λειτουργία, η οποία συλλέγεται μέσω εξωτερικών αισθητήρων μαγνητικής ροής που τοποθετούνται συμμετρικά γύρω από τον κινητήρα.

Η έρευνα διεξήχθη χρησιμοποιώντας δεδομένα από προσομοιώσεις διαφορετικών περιπτώσεων κινητήρα με βάση έναν πραγματικό επαγωγικό κινητήρα των 1.1 MW που χρησιμοποιείται στη βιομηχανία. Οι περιπτώσεις που εξετάστηκαν είναι αυτές των υγιών και εσφαλμένων κινητήρων σε διαφορετικές περιπτώσεις φορτίου. Συγκεκριμένα, εξετάστηκαν κινητήρες με σφάλμα μίας σπασμένης μπάρας, δύο γειτονικών σπασμένων μπαρών και δύο μη-γειτονικών σπασμένων μπαρών με απόσταση μισού πολικού βήματος. Οι προσομοιώσεις των κινητήρων πραγματοποιήθηκαν χρησιμοποιώντας λογισμικό ανάλυσης πεπερασμένων στοιχείων (Simcenter MAGNET) με ρυθμό δειγματοληψίας στα 5kHz. Στη συνέχεια, τα δεδομένα υποβλήθηκαν σε μετεπεξεργασία χρησιμοποιώντας το λογισμικό της MATLAB για την εφαρμογή των διαγνωστικών εργαλείων μέσω ανάλυσης των σημάτων στις διαφορετικές περιπτώσεις του κινητήρα, δίνοντας έμφαση στη μελέτη της συμπεριφοράς του κινητήρα με μη-γειτονικές σπασμένες μπάρες.

Acknowledgements

I would like to express my deepest gratitude to my project supervisor, Prof. Konstantinos Gyftakis, for his invaluable guidance, unwavering support, and continuous encouragement throughout this research. His mentorship has not only shaped this work but has also inspired my passion for the field of electrical machine diagnostics.

I am also sincerely grateful to Dr. Panagiotis Panagiotou for his expertise and insightful contributions, which significantly enhanced the quality of this research and deepened my understanding of signal processing in electrical machine diagnostics.

My heartfelt thanks go to my collaborator, Nikos Trachalakis, for his dedication, collaboration, and support throughout this endeavor.

Finally, I am profoundly thankful to my family for their unwavering support, patience, and encouragement. Their belief in me has been a constant source of strength and inspiration, making this journey both possible and meaningful.

Contents

List of Figures

List of Tables

List of Abbreviations

AC	**A**lternating **C**urrent
DC	**D**irect **C**urrent
IM	**I**nduction **M**otor
EMF	**E**lectro **M**otive **F**orce
MMF	**M**agneto **M**otive **F**orce
MCSA	**M**otor **C**urrent **S**ignature **A**nalysis
SFSA	**S**tray **F**lux **S**ignature **A**nalysis
IIoT	**I**ndustrial **I**nternet **o**f **T**hings
STFT	**S**hort **T**ime **F**ourier **T**ransform
FFT	**F**ast **F**ourier **T**ransform
MUSIC	**Mu**ltiple **Si**gnal **C**lassification
FEA	**F**inite **E**lement **A**nalysis
NEMA	**N**ational **E**lectrical **M**anufacturers **A**ssociation
RPM	**R**evolutions **P**er **M**inute
RMF	**R**otating **M**agnetic **F**ield
PD	**P**artial **D**ischarge
RSH	**R**otor **S**lot **H**armonics
PSH	**P**rincipal **S**lot **H**armonics
ZSC	**Z**ero **S**equence **C**urrent
ZSF	**Z**ero **S**equence **F**lux
FEA	**F**inite **E**lement **A**nalysis
FEM	**F**inite **E**lement **M**ethod
RMS	**R**oot **M**ean **S**quare

Chapter 1

Introduction

1.1 Motivation

The mighty interest that lies behind the development of condition monitoring strategies which are able to successfully address the failures occurring during the operation of an electric motor, stems from the industrial needs of trustworthy IMs. IMs, being the workhorses of industrial applications, are expected to perform efficiently under various harsh conditions. The goal of the diagnostic community is to ensure uninterrupted productivity, as any disruption in their operation can lead to significant financial losses, not only due to repair costs but also from the loss of productivity and potential damage to other connected machinery [1][2].

In particular, the detection and diagnosis of faults such as broken rotor bars are crucial. Broken bars are among the most prevalent faults in IMs, and their impact on motor performance is well documented.[3][4] They can lead to a wide variety of issues, including increased energy consumption, decreased motor efficiency, and even mechanical damage that can compromise the safety and longevity of the entire system [5]. The ability to accurately detect such faults before they escalate is, therefore, not just a matter of operational efficiency, but of strategic importance for maintaining competitive advantage in the industrial sector.

Furthermore, the increasing complexity and scale of industrial operations demand diagnostic tools that are not only accurate but also capable of identifying more subtle and less obvious faults. Non-adjacent broken bars represent such a challenge, as traditional diagnostic methods such as MCSA [6], often struggle to detect these faults early enough, before severe consequences take place[7].

The proposed diagnostic tool addresses this gap by focusing specifically on the detection of non-adjacent broken bars separated by half a pole pitch. This innovation is significant because it offers a solution to a problem that has been difficult to address with conventional methods. By improving the accuracy and reliability of fault detection in rotor cage IMs, this tool not only

enhances motor performance but also contributes to the broader goals of reducing maintenance costs, extending the lifespan of equipment, and ensuring uninterrupted industrial processes.

Moreover, this research aligns with the ongoing trends towards smart manufacturing and the Industrial Internet of Things (IIoT) [8], where real-time monitoring and predictive maintenance are becoming the norm. The ability to integrate such advanced diagnostic tools into existing motor monitoring systems represents a step forward in the evolution of industrial automation and maintenance strategies. Therefore, the development of this diagnostic tool is not just a technical achievement but also a contribution to the future of industrial reliability and efficiency.

1.2 Background

Rotor electrical malfunctions in cage IMs are frequently presented as broken or cracked rotor bars and end rings. These faults are often classified as hidden faults, since in the initial stages of failure, the impact on motor performance is minimal, making early detection challenging[9].

Scientifically, it has been shown that a bar breakage, can lead to the overloading of adjacent bars, resulting in higher current densities[10]. Thus, the adjacent bars are expected to break next due to their incapability of handling larger current densities. Despite that, there are numerous observed cases where non-adjacent bars were found broken, especially in large industrial motors that have their rotor cages made out of copper][11].

Traditional diagnosis techniques such as MCSA during steady-state operation may not reliably indicate the presence of non-adjacent broken bars. This occurs due to the fact that fault signatures may be obscured or not easily distinguishable from the healthy motor condition, leading to a false negative diagnostic alarm. The aforementioned situation has been shown to arise when two bar breakages happen to be located in positions separated by half a pole pitch owing to the cancellation of the magnetic imbalance caused by the two broken bars [12]. As a result, this leads to the absence of distinctive sidebands in the stator current spectrum or the appearance of weak signatures that are difficult to discern from normal variations [13][14].

According to the research conducted to date, the most effective methods for detecting non-adjacent broken rotor bars are the ones utilised during transient conditions, such as motor start-up. Prominent techniques in the literature include the STFT, Wavelets Method [15], MUSIC [16] and Dragon Transform [17]. In particular, the effectiveness of the aforementioned methods rely on the amplification of the magnetic asymmetry, caused by the skin effect and high rotor currents during start-up, which produces a distinct harmonic pattern over time.

Nevertheless, many industrial applications involve IMs that do not frequently undergo start-ups, as the motor's lifespan is linked to the number of starts. These motors typically operate

continuously for extended periods, rendering transient analysis methods impractical. Thus, there is a need for reliable detection methods capable of identifying broken bars, regardless of their location, during steady-state operation. Frequency extraction [18] has emerged as a promising method for these cases, though it is associated with high computational costs due to its two-stage signal processing approach.

1.3 Thesis Objectives

This study introduces the use of zero-sequence flux as a novel approach for monitoring non-adjacent broken bars in IMs during steady-state operation. This method is developed and validated through finite element analysis, examining motors across a range of power and voltage levels. Unlike the already existing zero-sequence current analysis method, the zero-sequence flux method is versatile and can be applied to any rotor cage IM, regardless of the stator winding configuration. Additionally, this method overcomes limitations related to spectral distortion caused by the stator winding distribution, offering a more reliable and comprehensive solution for fault detection in industrial applications, when compared with its counterpart method.

Furthermore, this thesis aims to provide a thorough understanding of the processes used in this research, including the implementation of signal processing techniques. It also seeks to enhance the understanding of IMs, their associated diagnostic techniques, and the application of FEA in motor fault detection. Through these objectives, the study not only proposes a new diagnostic method but also contributes to the broader knowledge base in the field of motor diagnostics.

1.4 Thesis Outline

- **Chapter 2 - Induction Machines:** This chapter offers a theoretical introduction to IMs, including a historical overview and a detailed explanation of their operation. The discussion will cover the fundamental principles behind IMs, their design, and their widespread use in various industrial applications.
- **Chapter 3 - Faults:** In this chapter, the various types of faults that can occur in IMs are discussed. The section will cover stress mechanisms, insulation types, and will focus particularly on rotor faults in Cage IMs. The impact of these faults on motor performance and reliability will also be discussed.

- **Chapter 4 - Diagnostic Methods:** This chapter reviews the diagnostic techniques used in this thesis for detecting broken bar faults in IMs. Both steady-state and transient operation methods will be explored, providing a comprehensive overview of the tools and methods used to identify and diagnose motor faults.
- **Chapter 5 - Finite Element Analysis:** The chapter introduces the theoretical background of Finite Element Analysis (FEA), detailing its mathematical foundations and its applications in engineering. The discussion will focus on how FEA is utilized in the context of motor diagnostics, setting the stage for its use in the subsequent chapters.
- **Chapter 6 - Motor Modelling:** This chapter focuses on the development of the motor model used in the simulations. It covers the process of defining the motor's geometry, setting the simulation parameters, and provides an extensive guide on how the model was constructed. This practical guide will serve as a valuable resource for understanding the steps involved in motor modeling.
- **Chapter 7 - Study Results and Analysis:** In this chapter, the results of the simulations conducted on various motor instances are presented. The performance of different diagnostic methods is compared, and the findings are discussed in depth. This analysis provides critical insights into the effectiveness of the proposed zero-sequence flux method.
- **Chapter 8 - Conclusions and Future Work:** The final chapter summarizes the overall findings of the research, drawing conclusions from the study results. It also outlines potential future directions for extending this research, suggesting areas where further investigation could enhance the effective application of the proposed diagnostic methods.

Chapter 2

Induction Machines

2.1 Energy Conversion and the Electric Machine

The continuous progress of technology is inextricably linked to the concept of energy conversion, a process that plays a crucial role in human daily life. From the early days of the industrial revolution to the present era, the need for efficient electromechanical energy conversion has become even more pressing. Therefore, by seeking ways to meet humanity's needs for electrical and mechanical power, the concept of the electrical machine is discovered [19].

An electric machine is a device that converts electrical energy into mechanical energy and vise versa, through the action of a magnetic field. Such a device, when used to convert electrical power into mechanical power is called a motor, while when used to convert mechanical power into electrical power is called a generator. In this context, electric machines emerge as key players in electromechanical energy conversion, making them pivotal for the production, transmission, and utilisation of electrical energy.

2.2 The Induction Electric Machine

The Induction or Asynchronous Machine is a key subcategory of AC Machines, distinguished by its method of operation, which relies on the principle of electromagnetic induction. Unlike other types of AC machines, such as the Synchronous Machine, that requires an external source of DC current in order to produce its excitation current, the induction machine induces its excitation current into the rotor through the rotating magnetic field generated by the stator windings [20]. This design not only makes it robust and reliable but also widely used in various industrial and commercial applications due to its simplicity and efficiency. As a subset of AC motors, IMs play a crucial role in converting electrical energy into mechanical energy in a vast array of equipment and machinery.

2.3 Historical Background

The development of the IM is deeply rooted in the foundational discoveries of electromagnetic theory. In 1831, Michael Faraday made a groundbreaking contribution to science with his discovery of electromagnetic induction, establishing the principle that a changing magnetic field can induce an electric current in a conductor. This discovery laid the groundwork for understanding how electrical energy could be converted into mechanical energy.

Building on Faraday's work, James Clerk Maxwell formulated the laws of electromagnetism, known as Maxwell's equations, in the 1860s. These equations provided a comprehensive mathematical framework for understanding electric and magnetic fields, further solidifying the theoretical foundation of electromagnetism.

With these powerful tools at their disposal, two of the greatest scientists of all time, Galileo Ferraris and Nikola Tesla, were able to independently invent the IM in 1885 and 1887, respectively [21]. Their contributions harnessed the principles of electromagnetic induction and rotating magnetic fields, leading to the creation of the IM, a device that revolutionized the way electrical energy is used to power machinery and transformed industries worldwide. Their inventions are shown in Figure 2.1 and 2.2.

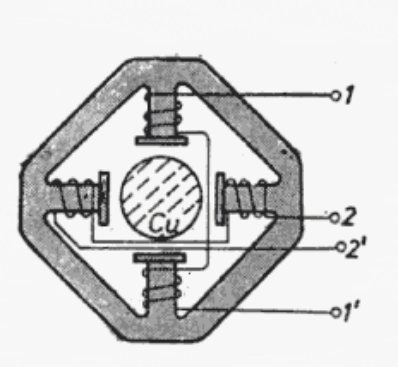

FIGURE 2.1: Ferraris' Motor (1885) [22]

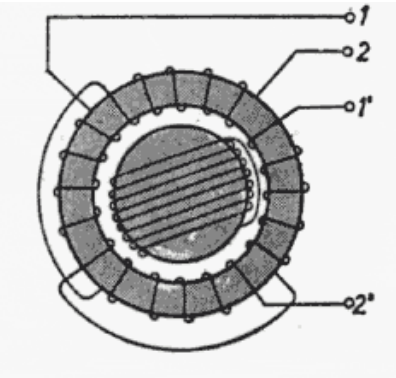

FIGURE 2.2: Tesla's Motor (1887) [22]

The aforementioned IM prototypes utilized a set of electromagnets arranged at right angles to each other. As seen in the figures, these electromagnets were powered by two alternating currents, 90° out of phase with each other, with each current's pole terminals being shown as 1-1′ and 2-2′. This phase difference between the currents generated a rotating magnetic field, which is essential for the operation of the motor. Ferraris's design allowed for the direction of the motor's rotation to be easily reversed by simply reversing the polarity of one of the alternating currents. This innovative concept of creating a rotating magnetic field laid the foundation for the development of the self-starting IM, which became a cornerstone in the field of electrical engineering.

2.4 Squirrel-Cage Induction Machine

The core structure of an IM (Figure 2.3) consists of two main components: the stator and the rotor. The rotor's design plays a crucial role in defining the motor's characteristics, leading to various types of induction machines tailored to specific operational requirements. Among these, squirrel cage IMs represent a significant and widely used subcategory. Named after the squirrel-cage-like structure of their rotor, these motors are renowned for their durability, simplicity, and efficiency. Their robust design and ease of maintenance make them the preferred choice for many industrial and commercial applications. As the primary focus of this study, three-phase squirrel cage IMs will be explored in depth, emphasizing their operational principles, performance characteristics, and widespread utility in modern electrical systems [23].

FIGURE 2.3: Squirrel-Cage IM [24]

2.4.1 Rotor

The rotor, as the rotating part of the motor, is a critical component of an IM, responsible for converting electrical energy into mechanical motion. In squirrel cage IMs, the rotor consists of conductive bars, which are molded inside the rotor's core (Figure 2.4).

Rotor Bars

The conductive bars in the rotor of a squirrel cage IM are typically made from materials chosen based on the motor's power rating. For lower power applications, generally well below 1 MW, aluminum is commonly used due to its cost-effectiveness, light weight, and sufficient electrical conductivity for these power levels [25]. In contrast, for higher power applications, copper is preferred because of its superior electrical conductivity, which minimizes energy losses and allows for more efficient operation. The rotor bars are short-circuited by end rings to form a structure resembling a squirrel cage. This design is integral to the motor's operation, as the rotating magnetic field produced by the stator induces currents in the rotor bars, creating a magnetic field that interacts with the stator's field to produce torque.

Additionally, the rotor bars are skewed, meaning they are slightly angled rather than perfectly straight. This skewing is crucial for reducing undesirable effects such as cogging and harmonic distortions, which can negatively impact the motor's smooth operation [23].

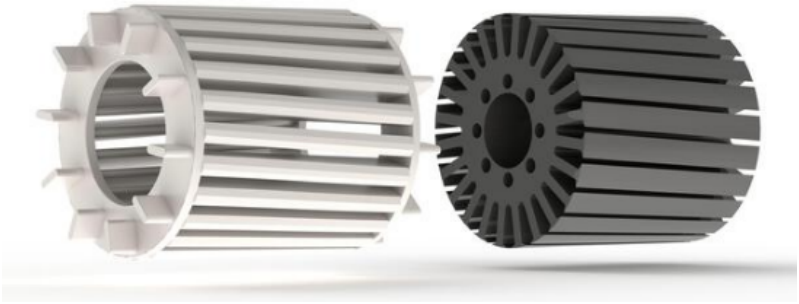

FIGURE 2.4: Rotor's Exploded View (Cage and Core) [26]

NEMA classes for Rotor Design

The NEMA is an organization that sets industry standards for electrical equipment, including motors. NEMA standards are widely recognized and used to ensure consistency, safety, and interoperability across different manufacturers and products. For electric motors, NEMA has developed classifications that define design specifications such as frame sizes, enclosures, and performance characteristics. These standards help ensure that motors meet specific operational requirements and can be reliably used in various industrial and commercial applications. By providing a common framework, NEMA standards facilitate the selection, installation, and maintenance of electric motors across different sectors [27].

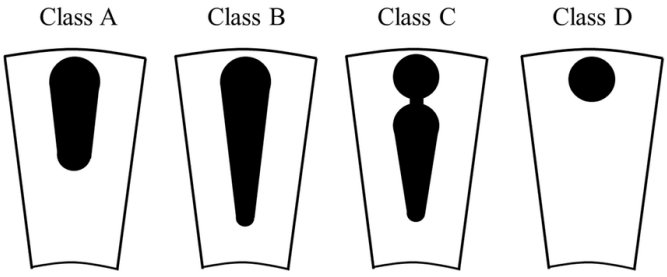

FIGURE 2.5: NEMA Rotor Design Classes [28]

NEMA classes categorize electric motors according to their starting torque and the type of load they are designed to accelerate. The four standard NEMA design classes (Figure 2.5) are:

Class A motors have a maximum 5% slip with a high to medium starting current, normal locked rotor torque, and normal breakdown torque. These characteristics make them well suited for a wide vareity of applications and they are often found powering fans and pumps.

Class B motors, like Class A, have a maximum slip of 5% and normal breakdown torque. However, they are distinguished by their low starting current and high locked rotor torque. These characteristics make Class B motors ideal for applications that require normal starting torque, making them particularly well-suited for HVAC systems. They are commonly used to power pumps, blowers, and fans, where reliable and efficient operation is essential.

Class C motors feature a maximum slip of 5%, low starting current, high locked rotor torque, and normal breakdown torque. These attributes make them particularly effective for applications with high starting torque requirements and significant inertia, such as conveyors and positive displacement pumps. Their design ensures reliable performance during startup and under varying load conditions, making them well-suited for demanding industrial tasks where high initial torque is essential.

Class D motors are characterized by a slip range of 5% to 13%, low starting current, and very high locked rotor torque. These features make them ideal for applications that demand exceptionally high starting torque and can handle substantial inertia, such as hoists and cranes. Their design supports reliable operation in conditions where heavy loads are started and controlled, ensuring effective performance in demanding industrial environments.

Rotor Core

The rotor core of a squirrel cage IM is meticulously designed to enhance performance and efficiency. It is constructed from laminated sheets (Figure 2.6), a design choice that minimizes induced eddy currents and improves the motor's overall efficiency by reducing heat generation.

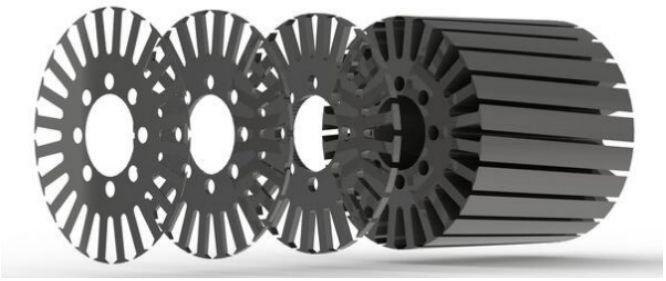

FIGURE 2.6: Rotor Core Laminations [29]

2.4.2 Stator

The stator (Figure 2.7) is the stationary part of the cage motor and consists of a cylinder core with slots and a series of windings. When the stator windings are energized by a polyphase (three or more phases) alternating current supply, they generate a rotating magnetic field that

induces a corresponding rotating magnetic field in the rotor, thereby producing the torque required to drive the load.

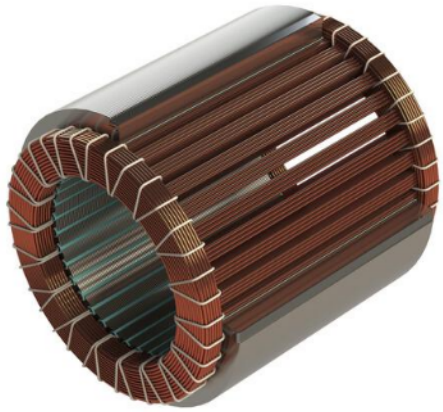

FIGURE 2.7: Stator [30]

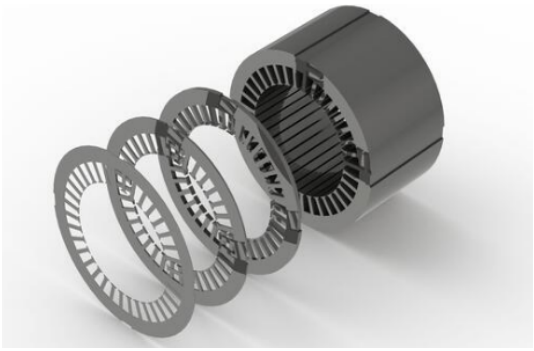

FIGURE 2.8: Stator Laminations [30]

Stator Core

The stator's cylindrical core is constructed from a ferromagnetic material and features slots to hold the windings. Similar to the rotor, the stator core is laminated (Figure 2.8), which helps minimize eddy current losses.

Windings

The windings in an IM are made up of conductors placed within the core slots of the stator. These conductors can be connected either in parallel or in series, depending on the desired electrical characteristics. When two conductors are connected in series, they form a conductor loop. Multiple such loops connected in series create the complete winding.

The windings in low-voltage motors (below 1kV) are typically made using enameled copper cables with a diameter of less than 2.5mm. These windings can be constructed either manually or with the help of winding machines, depending on the specific requirements and scale of production.

In larger-scale motors operating at more than 1 kV, such as the motor studied in this dissertation, form-wound coils (Figure 2.9) are typically used. These coils are made from enameled rectangular wires, which offer better space utilization and improved electrical characteristics compared to round wires. The coils can be manufactured either manually or with the help of winding machines, depending on the production process.

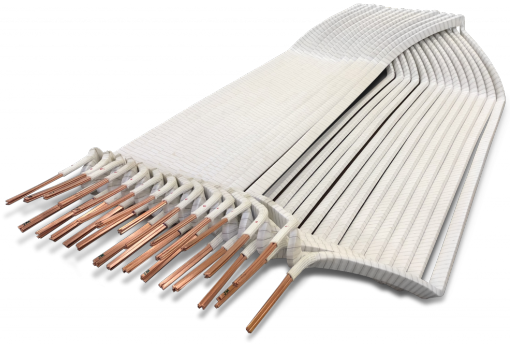

FIGURE 2.9: Form-Wound Coils [31]

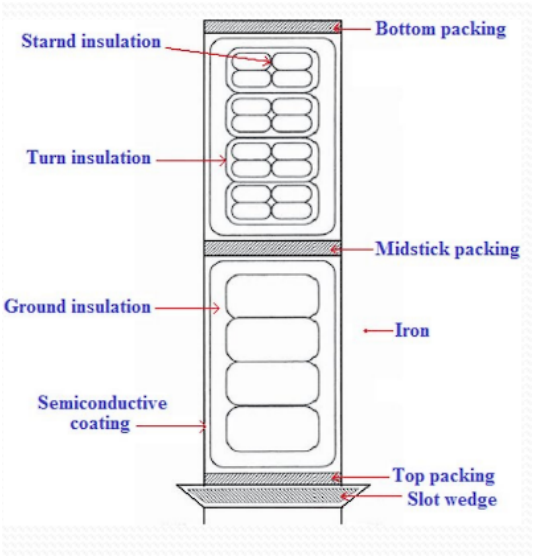

FIGURE 2.10: Cross-Sectional View of a Double-Layered Slot with Form-Wound Coils [32]

Winding Procedure

For low voltage motors, the stator slot, which houses the multiple enameled conductors, is first lined with an insulation sheet to ensure electrical isolation and protection. The conductors are then placed securely within the insulated slot. Once the conductors are in place, a wedge is inserted at the top of the slot. This wedge holds the conductors firmly in position, preventing them from shifting due to centrifugal forces during motor operation, thereby ensuring the stability and integrity of the winding structure.

For high-voltage motors, the formed coils are inserted into the stator slots according to the winding configuration, whether it is a single-layer or double-layer winding. As shown in Figure 2.10, these coils are precisely positioned within the slot and are surrounded by multiple layers of insulation to ensure electrical safety and optimal performance.

The coils are first insulated with a strand insulation, followed by a turn insulation to provide additional electrical separation between individual turns. The entire coil is then surrounded by ground insulation, which prevents electrical leakage to the stator core.

The slot also features a semi-conductive coating on the inner surface, which reduces the risk of partial discharges between the coil insulation and the iron core. To secure the coils in place, a bottom packing is placed at the base of the slot, and a top packing is applied above the coils. Additionally, a mid-stick packing may be used between layers of coils to ensure uniform pressure and stability. Finally, a slot wedge is inserted at the top of the slot to lock the coils in

position, preventing any movement due to mechanical vibrations or centrifugal forces during operation. This combination of insulation, packing, and mechanical support ensures the reliable operation of the motor under high-voltage conditions.

Winding Geometry

The windings placed must be symmetrically positioned to create the necessary pole pairs. In a three-phase winding configuration, various winding techniques can be employed, such as the example displayed below (Figure 2.12).

Additionally, the electrical phase angle is determined by the number of pole pairs in the motor. Based on this, the mechanical phase angle is calculated, and the windings are carefully positioned accordingly. This relationship is expressed as:

$$\theta_{el} = 2p \cdot \theta_{mech} \tag{2.1}$$

Showing a simple three-phase, 2-pole motor (Figure 2.11), the winding is arranged in such a way that each phase is separated by 120 electrical degrees, creating a balanced three-phase system.

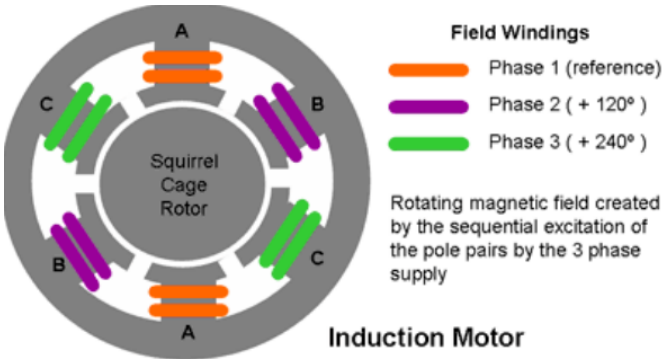

FIGURE 2.11: Winding Geometry and Pole Pairs [33]

FIGURE 2.12: Inside View of Stator Windings [34]

In this configuration, three sets of windings — labeled as Phase 1 (reference), Phase 2 (+120°), and Phase 3 (+240°) — are distributed symmetrically around the stator core. As the three-phase AC supply energizes these windings in sequence, it creates a rotating magnetic field.

Motor Frame

As shown in the Figure 2.13, the frame that is usually made out of cast-iron, forms the outer housing of the motor, providing structural support and protecting the internal components

from environmental factors like dust, moisture, and physical impact. It also serves as a conduit for heat dissipation generated by the motor during operation, ensuring durability and long-term performance. The frame is equipped with mounting points to secure the motor to its base, as well as a lifting eye for easy transportation and installation.

Cooling Fan

The cooling fan (Figure 2.13) is mounted on the shaft at the non-drive end of the motor, positioned behind the end bell. Its primary function is to maintain optimal operating temperatures by circulating air over the surface of the motor and through its internal parts. This airflow dissipates the heat generated by the stator and rotor, preventing overheating and ensuring efficient performance. The fan cover protects the cooling fan from external objects and debris.

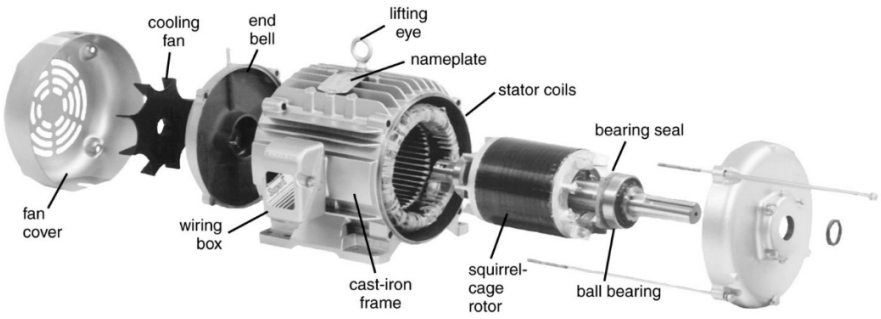

FIGURE 2.13: Exploded View of a Three-Phase Cage Motor [35]

Terminal Box

The Terminal box is mounted on the motor's frame. It contains the terminal connections where the incoming electrical supply lines are connected to the motor's windings. Besides providing a safe and organized space for these connections, the wiring box plays a crucial role in determining the winding configuration of the motor, whether it is star or delta. This configuration directly affects the motor's operating characteristics, such as voltage, current, and torque.

The terminal box also protects the electrical connections from external factors like dust, moisture, and mechanical damage, maintaining the motor's electrical integrity and preventing potential faults or short circuits. Proper labeling and secure fastening within the box ensure that maintenance and reconfiguration can be done safely and efficiently.

Bearing

The bearing is a crucial component located at both ends of the rotor shaft, supporting the shaft while allowing it to rotate smoothly with minimal friction. The bearings are enclosed within the bearing seal to prevent the ingress of dust, dirt, and moisture, which could damage the

bearing surfaces. They help to maintain the alignment of the rotor within the stator, reducing wear and prolonging the life of the motor by providing a stable, low-resistance path for the rotational movement of the rotor.

2.5 Basic Principles of Operation for IMs

As previously mentioned, IMs operate on the principle of electromagnetic induction, a phenomenon discovered by Michael Faraday in 1831. The core of their operation lies in the interaction between the magnetic field generated by the stator windings and the currents induced in the rotor bars. When a three-phase AC is applied to the stator windings, it creates a rotating magnetic field. This rotating field induces a voltage in the rotor, which in turn generates a current within the rotor bars. Due to the significantly higher conductivity of the rotor bars compared to the ferromagnetic core of the rotor, the induced currents flow through the bars.

Once the operating principle of an IM is met, Lorentz forces are generated in the rotor bars. These bars are symmetrically arranged around the circumference of the rotor in opposite pairs. As a result, the forces produced create a torque that drives the rotation of the rotor. The required mechanical torque of the motor is expressed as follows:

$$T_{mech} = T_L + J\frac{d\omega}{dt} \tag{2.2}$$

Where T_{mech} represents the mechanical torque that the motor must generate to overcome the opposing load torque and any resistances to start and maintain the desired rotational motion. T_L denotes the load torque that the motor must overcome to perform its work. The symbol J stands for the combined moment of inertia of the rotor and the load it drives. Finally, $\frac{d\omega}{dt}$ refers to the rate of change of angular velocity, representing how quickly the rotor's speed is changing over time.

2.5.1 The Asynchronous Operation

The term "asynchronous" is a Greek word having a negative prefix "a-" meaning "not" and "synchronous," meaning "occurring at the same time". In the context of IMs, it describes a process that does not happen simultaneously or in sync; specifically, the rotor speed does not match the speed of the stator's rotating magnetic field.

Synchronous Speed

The symmetrical three-phase alternating voltage applied to the stator windings creates a magnetic field that rotates at an angular speed directly proportional to the frequency of the applied

voltages. This angular speed is known as "synchronous speed" and can be calculated using the following equation:

$$\omega_s = \frac{2\pi f_s}{p} \quad (rad/sec) \tag{2.3}$$

Where f_s is the electric frequency and p denotes the number of pole pairs in the motor.Using the above equation, the synchronous speed in revolutions per minute (RPM) can be determined as follows:

$$n_s = \frac{60 f_s}{p} \quad (RPM) \tag{2.4}$$

Rotating Magnetic Field

The rotating magnetic field is the result of the superposition of the magnetic fields generated by the three-phase currents in the stator windings. Mathematically, this field is a sinusoidal function in both time and space, rotating at the synchronous speed determined by the supply frequency and the number of poles of the motor. As mentioned earlier, the stator of a three-phase IM consists of a number of a number of overlapping windings offset by an electrical angle of 120 degrees. The three windings consist of the same number of turns and have the same resistance. The RMF produced can be mathematically expressed as [36]:

$$B(x,t) = B_{max} \cdot sin\left(\omega t + \pi \frac{x}{\tau_p}\right) \tag{2.5}$$

Where τ_p is the polar distance between two adjacent poles, x is the distance on the inner circumference of the stator's cross-section, calculated from a random point and t is the time.

Operation Zones

The RMF in an IM induces currents in the rotor cage, which then interact with it to produce electromagnetic torque. This torque causes the rotor to turn in the same direction as the RMF, following Lenz's Law, which dictates that the induced currents act to oppose the changes that generate them. As a result, the rotor attempts to match the speed of the rotating magnetic field. If the rotor were to achieve the same speed as the RMF, the relative motion between them would cease, leading to a drop in induced current and, consequently, a loss of electromagnetic torque. However, due to mechanical losses and other factors, the rotor never fully reaches synchronous speed in practical applications, allowing the motor to continuously generate torque.

As shown in Figure 2.14, when the motor is under load and in the **Motoring Zone**, the slip increases as the load increases, causing the rotor's speed to decrease. As a result, the induced current and the torque produced by the motor also increase. This process continues until a certain point known as the **Breakdown Point** is reached. At this point, the motor produces its maximum torque, while beyond this point, the torque begins to decrease and the motor enters the **Unstable Region**, marking the breakdown torque as the highest torque the motor can generate. The operational range from synchronous speed to the breakdown point is termed the **Stable Region**, where the motor operates reliably.

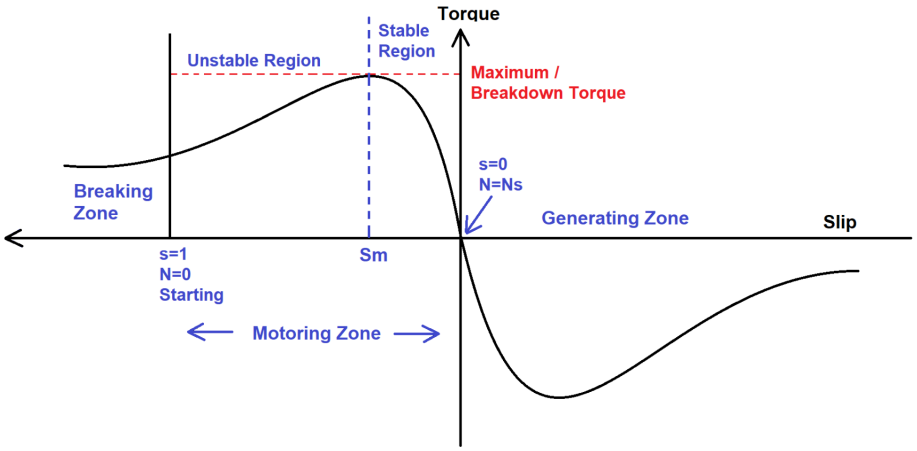

FIGURE 2.14: Torque-Speed Curve of an IM [37]

In case of the rotor operating at a faster rate than the RMF, the machine is now considered as a generator and enters the **Generating Zone**, as it feeds electric energy into the grid via the stator and the slip becomes negative.

Lastly, a unique operating condition called **Braking Zone** is occurring in specific circumstances where the motor attempts to lift a load that generates a larger electromagnetic torque than the motor itself. In such cases, the rotor is forced to rotate in the opposite direction of its intended rotation. In this braking region, the slip remains positive but is significantly higher than in normal motor operation. The motor, in this state, draws energy both from the electrical supply through the stator and from the mechanical load on the shaft, converting all incoming energy into heat within the motor, having as a result the immediate breakdown of the motor.

Slip

During the nominal operation of an induction machine, the rotor speed typically remains close to the synchronous speed. When the machine operates as a motor, its nominal speed is slightly lower than the synchronous speed. Conversely, if the machine is functioning as a generator, its nominal speed exceeds the synchronous speed.

The magnetic field generated in the rotor due to the induced voltage is naturally alternating. To reduce the relative speed with respect to the stator, the rotor begins to move in the same direction as the stator's magnetic field, attempting to align itself with the rotating field. However, in practice, the rotor never fully aligns with the stator's magnetic field and instead moves slightly slower than the synchronous speed of the stator's field. The difference between the synchronous speed n_s and the rotor speed n is known as slip, which varies depending on the load. An increase in load causes the rotor to slow down further, thereby increasing the slip, while a decrease in load allows the rotor to speed up, reducing the slip. If the rotor speed is denoted as n, the slip (s) is calculated using the following expression:

$$s = \frac{n_s - n}{n_s} = \frac{\omega_s - \omega}{\omega_s} \tag{2.6}$$

Where n_s is the synchronous speed, ω_s is the synchronous angular speed and ω is the rotor speed. This equation holds true since speed (RPM) and angular speed (rad/sec) are directly related by a constant factor, as can be seen from the equations 2.3 and 2.4. As a result, the relationship between the slip in terms of speed and angular velocity remains consistent and equivalent.

Additionally, given that the speed of the induced quantities on the rotor is $n_r = n_s - n$, then from the equation 2.6 the frequency of those quantities is expressed as:

$$f_r = s f_s \tag{2.7}$$

2.5.2 Equivalent Circuit

The equivalent circuit of an IM (Figure 2.15) consists of the stator windings, representing all three phases, the iron core, and the rotor circuit, also modeled for each phase. This comprehensive representation accounts for the electrical and magnetic interactions within the motor, including the stator and rotor resistances, reactances, and the mutual coupling between the stator and rotor through the core.

The main compartments of the equivalent circuit are:

- R_1: Ohmic resistance of the stator winding which is responsible of the copper losses of the stator windings.
- X_1: Stator leakage reactance
- R_o: Core losses
- X_o: Magnetising reactance

- X_2': Rotor leakage reactance
- R_2': Rotor resistance, which is responsible of the joule losses of the rotor.
- $R_2'\left[\frac{1-s}{s}\right]$: Equivalent electromechanical power resistance

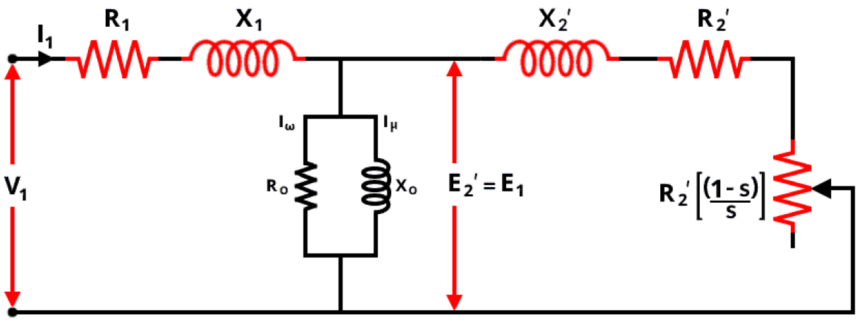

FIGURE 2.15: Equivalent circuit of an IM [38]

Power Losses

The diagram in Figure 2.16 illustrates the various power losses that occur during the operation of an induction motor. The total input power, represented as active power to the stator also known as P_{el}, enters the motor and is partially dissipated as stator copper losses due to the resistance in the stator windings, as well as stator iron losses within the magnetic core. The remaining active power is then supplied to the rotor. In the rotor, additional power losses occur, including rotor losses from the rotor. Finally, mechanical losses occur at the shaft due to friction. The net mechanical power is then converted into useful output power at the shaft, also known as shaft power or P_{em}. This shaft power represents the effective mechanical power available for performing work. The diagram clearly demonstrates the sequential flow of power through the motor and highlights the points where losses occur, ultimately reducing the total power available from the input to the output and affecting the overall efficiency of the motor.

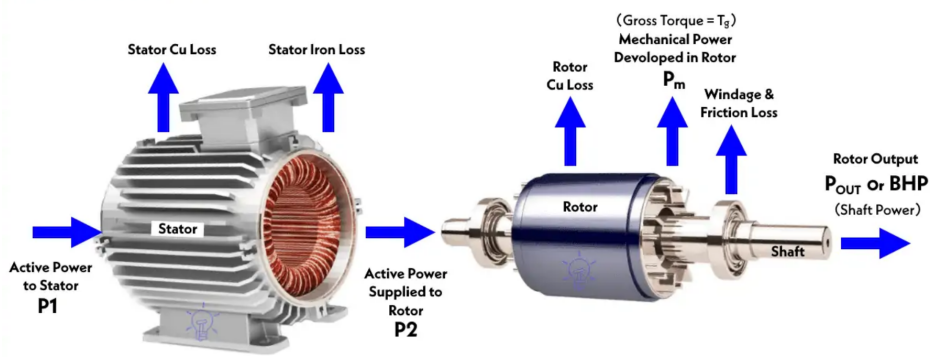

FIGURE 2.16: Power losses during the operation of an IM [39]

Chapter 3

Faults

Industrial electric motor systems are responsible for nearly 60% of the global electric power consumption, with IMs accounting for approximately 80% of this total [40]. This significant energy demand underscores the critical importance of improving the performance and reliability of IMs, making it a vital area of ongoing research. However, despite their robustness and efficiency, IMs are not immune to faults, which can lead to reduced performance, unexpected downtime, and increased operational costs. Understanding the nature and causes of these faults is essential to ensuring the longevity and efficiency of these motors, thereby optimizing energy consumption and reducing maintenance expenses in industrial applications [41].

3.1 Root Causes of Faults

3.1.1 Construction Imperfections

The root causes of faults in electric motors generally arise from construction imperfections, which can introduce asymmetries even in newly manufactured machines. One of the most common construction-related issues is static eccentricity [42], which occurs when the inner surface of the stator is not perfectly circular or when the rotor is incorrectly positioned within the stator during assembly. This misalignment results in the rotor not being perfectly centered, leading to an uneven air gap between the rotor and stator. It is termed "static" eccentricity because the center of rotation remains fixed over time (Figure 3.2). Another significant construction flaw is the porosity [43] in the stator and rotor cores and rotor cage. Porosity refers to the presence of small voids or air pockets within the laminated steel cores, which can occur during the manufacturing process, particularly during the casting of the rotor cage (Figure 3.1) or the assembly of the stator and rotor core laminations. These voids can weaken the structural integrity of the cores, reduce magnetic efficiency, and lead to localized heating, ultimately contributing to motor failure.

FIGURE 3.1: Severe case of porosity in the end ring of the aluminum casted rotor cage [44]

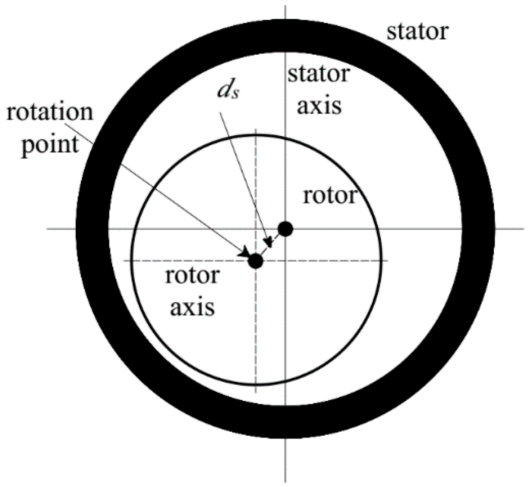

FIGURE 3.2: Static Eccentricity [45]

3.1.2 Degradation & Ageing

Beyond construction imperfections, the components most susceptible to degradation and aging are those exposed to the stress mechanisms collectively referred to as TEAM [46](Thermal, Electrical, Ambient, and Mechanical). The most affected components include the rotor, stator, and bearings, among others. These critical parts endure constant stress from heat, electrical currents, environmental conditions, and mechanical forces, making them particularly vulnerable to wear and faults over time.

Rotor Degradation

The rotor's life expectancy is closely tied to the frequency of motor starts. Frequent starting, which is often required by the nature of the task, significantly impacts rotor longevity. This is because, during startup, the stator draws up to five times the normal operating current, imposing substantial thermal and electrical stress on the rotor cage. Due to the skin effect that takes place, the upper part of the bars gets more thermally stressed than the lower part. To further elaborate, the rotor cage of a squirrel-cage IM is subjected to significant centrifugal forces during operation. The mechanical stress exerted on the rotor bars and end rings is particularly intense as these components work to withstand the forces that keep them in place. This stress is most pronounced when the rotor reaches its maximum speed, typically during the stable region of operation, as the centrifugal force is proportional to the square of the rotor's speed. Consequently, these forces contribute to the long-term mechanical strain on the rotor cage, impacting its durability and potentially leading to fatigue or failure over time.

Finally, the type of load the IM is expected to handle plays a critical role in determining its lifespan. High-inertia loads, which are particularly difficult to accelerate during the startup

phase, further accelerate rotor wear and deterioration, as the rotor must endure greater electrical, mechanical and thermal stresses in these conditions.

Stator Degradation

The stator is particularly vulnerable to the degradation of its winding insulation. Thermal losses generated during motor operation are especially harmful to the insulation material, as they gradually weaken its integrity. Additionally, sudden temperature changes cause the copper conductors to expand faster than the insulation material, leading to mechanical stress and further accelerating degradation. High moisture levels and chemical reactions also pose significant threats to the stator windings, as they can deteriorate the insulation material over time. Another major issue for stator insulation is Partial Discharges (PDs), which occur due to voids or gaps in the insulation material caused by manufacturing imperfections and the non-uniform distribution of the electric field within the motor. These PDs lead to a gradual breakdown of the dielectric properties of the insulation, ultimately rendering it ineffective over time [47].

Bearing Degradation

Most bearings used in electric motors operate under harsh conditions, making them vulnerable to fatigue, mechanical vibration, misalignment, contamination, overloading, corrosion, incorrect lubrication, and other factors leading to the premature wear of this component [48].

3.1.3 Human Factor

Finally, human errors are also significant contributors to motor faults. These include selecting the wrong type or size of motor, inadequate maintenance, whether it be infrequent or focused on the wrong components, improper operation and, in some cases, incorrect diagnosis. Misjudgments in any of these areas can lead to sub-optimal motor performance and increase the likelihood of faults.

3.2 Stator Insulation

Industrial surveys have consistently shown that the electrical insulation used in stator and rotor windings is the component most prone to failure [49][50]. This vulnerability arises because the organic materials in the insulation, such as polyesters, epoxies, and polyamide-imides, have significantly lower mechanical strength and thermal capacity compared to the metals that make up the majority of the electrical machine. As a result, insulation testing is routinely performed to identify machines with weakened insulation, allowing for proactive maintenance and reducing the risk of in-service failure.

3.2.1 Insulation Types

The stator insulation is designed with specific characteristics to prevent short circuits, manage the thermal losses from the winding conductors, and minimize the effects of vibration-induced stress. As mentioned in Chapter 2 and shown in Figure 2.10, there are three main types of insulation in stator windings, each with distinct properties [51].

Strand Insulation, which protects individual strands within a conductor.

Turn Insulation, which separates turns of the winding to prevent electrical short circuits between them.

Groundwall Insulation, which provides the final and most critical barrier between the winding and the grounded stator core, ensuring the overall electrical integrity of the motor. If the groundwall insulation fails, mechanical protection systems disconnect the motor from the grid to prevent further damage or hazards.

3.2.2 Chemical Background of Insulation Deterioration

The deterioration of electrical insulation is largely driven by chemical processes, particularly oxidation and depolymerization. Over time, oxidation causes the polymer chains within resin insulation to break down by introducing acid groups in the polymeric insulation, reducing their tensile strength, flexibility and increasing the conductivity of the insulation. This process can be accelerated by the presence of excessive heat, oxygen, and other environmental factors, leading to the embrittlement and hardening of insulation. Furthermore, depolymerization, a chemical reaction in which polymer chains break into shorter segments, occurs at elevated temperatures, even in the absence of oxygen. This deterioration mechanism is slower than oxidation, but its effects become significant over time. These chemical changes weaken the insulation material, increasing the likelihood of electrical failure, which can ultimately result in short circuits or other critical failures within the motor [52].

Life Expectancy of Insulation

The main ageing factors of insulation materials are thermal and thermo-mechanical stresses. For this reason, mathematical models where developed in order to estimate the lifetime of insulation materials.

The lifespan of the insulation material enduring thermal stress with a constant temperature T can be expressed by the following equation [53]:

$$L_T(T) = L_o e^{\frac{B}{T} - \frac{B}{T_o}} \tag{3.1}$$

Where L_o represents the lifetime at a reference temperature T_o and B is the activation energy constant of the degradation process. This model relates the thermal ageing to the rate of a temperature dependent chemical reaction, through the use of the Arrhenius equation.

For the case of thermo-mechanical stress, this stress arises from the uneven temperature distribution in the wire during thermal cycling. As the motor heats up and cools down, the conductor and insulation materials expand and contract at different rates due to their distinct thermal properties. The conductor, typically made of copper, expands more rapidly than the surrounding insulation. This mismatch in expansion and contraction rates creates mechanical stress on the insulation, which can lead to cracks, degradation, and eventual failure of the insulation material over time, further compromising the motor's electrical performance.

It has been demonstrated that a higher rate of temperature increase results in greater non-uniformity in the conductor's temperature. Consequently, the thermo-mechanical stress becomes directly related to the rate of temperature change over time v. This relationship can be modeled by the following equation [54]:

$$L_M(v) = (1 + k|v|)^{-N} \tag{3.2}$$

Where L_M is the lifespan of the insulation under constant temperature change v, while k and N are the parameters that can be configured with conducted accelerated stress tests.

For finding the simultaneous impact of thermal and thermo-mechanical stresses, the winding insulation lifetime could be properly modeled by adding a correction term G [55]. Therefore, the lifetime L can be represented as a multiplication of the equations 3.1, 3.2 and the correction term $G(T, v)$ 3.4.

$$L(T, v) = L_T(T) L_M(v) G(T, v) \tag{3.3}$$

$$G(T, v) = (1 + k|v|)^{N(\frac{B}{T} - \frac{B}{T_o})} \tag{3.4}$$

3.3 Fault Types

Faults in Rotor Cage IMs can be classified into different categories depending on the motor component affected, most notably the rotor and the stator.

Rotor Faults can be divided into three main categories: electrical faults, magnetic faults, and mechanical faults. Electrical faults in the rotor typically involve open circuits such as broken

or cracked cage bars and end rings. Magnetic faults are associated with issues like iron deformation or magnetic anisotropy, which affect the rotor's magnetic performance and lead to inefficiencies. Mechanical faults include issues such as eccentricity, where the rotor is misaligned within the stator, either statically, dynamically or both. Bearing faults, another mechanical issue, can range from localized defects to distributed defects, leading to vibrations, noise, and eventual motor failure.

Stator faults primarily include electrical faults and magnetic faults. Electrical faults in the stator involve issues such as open circuits, inter-turn faults, or short circuits between phases or to the ground. Lastly, Magnetic Faults, are related to iron core deformation.

The diagram below provides a visual representation of the most common types of faults that occur in the aforementioned components (Figure 3.3).

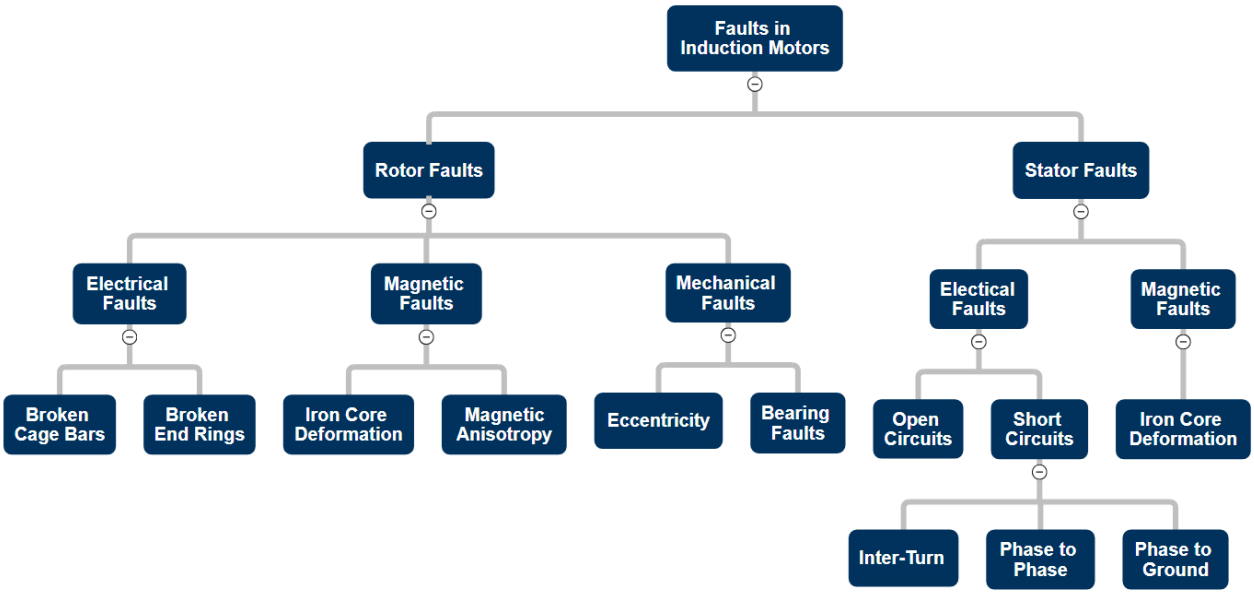

FIGURE 3.3: Faults in IMs [56]

3.4 Broken Cage Bars & End Rings

Broken cage bars and end rings are common faults in squirrel cage IMs, typically resulting from a combination of stresses that accumulate over time. These faults arise from several key factors, including thermal stresses caused by constant heating and cooling cycles, which lead to expansion and contraction of the rotor materials. Electromagnetic forces also impose significant magnetic stresses, especially when there is asymmetry in the magnetic field, which can result from construction imperfections or irregularities in the motor's operation.

In addition, environmental factors such as high moisture levels can lead to corrosion, further weakening the rotor bars and end rings. Mechanical stresses, such as loose windings or faulty

bearings, exacerbate the problem, as these issues create vibrations and imbalances that place additional strain on the rotor's components. Over time, these combined stresses contribute to the degradation of the cage bars and end rings, eventually leading to cracks and breakages that impair the motor's performance.

Rotor cages in IMs are typically made from either aluminum or copper, depending on the motor's scale, and the location of bar breakage tends to vary based on this material characteristic. In low to medium scale motors, the rotor cage is generally constructed from cast aluminum (Figure 3.1). Breakage in aluminum cages commonly occurs in areas where casting imperfections, such as voids or pores, are present. These imperfections create zones of higher resistance, leading to localized overheating, which weakens the material over time. As a result, in aluminum cages, bar breakages can occur unpredictably across the cage. Additionally, aluminum rotor faults are generally irreparable due to the casting nature of the cage [57].

On the other hand, copper rotor cages are more commonly used in larger motors. In these designs, the copper bars are inserted into slots in the rotor core, and the end rings are welded to the bars. Breakages in copper rotor cages typically occur at the junction between the bars and the end rings, where repeated thermal expansion and contraction stress the welded connections. While copper rotor faults can be repaired if detected early, the consequences of such failures can be severe. A broken copper bar may bend and come into contact with the stator windings, causing significant damage and potentially leading to catastrophic failure [36].

Chapter 4

Diagnostic Methods

As previously discussed, the operation of electric machines reveals significant imperfections due to their construction, aging, and human factors. Given the rapid upward trend in energy demand in our era, adaptation is necessary to find ways to improve energy efficiency. At this juncture, the concept of the science of fault diagnosis in electric machines is introduced, aiming to investigate their behavior in various faulty scenarios.

The field of Fault Diagnosis is a critical subcategory of condition monitoring that specifically focuses on identifying and analyzing faults in machinery. In fault diagnosis, the fault has already occurred, and the primary goal is to detect and understand the nature of the fault through a systematic process. By extracting valuable information about the fault, this method helps in determining the root cause, assessing its impact, and guiding necessary corrective actions to prevent further damage or failure.

The fundamental concept of fault diagnosis is to detect a fault in its early stages. This means that while the machine remains fully operational, the diagnostic process identifies the fault before it escalates into a serious issue that could cause significant damage or lead to complete motor failure.

4.1 The Diagnostic Procedure

All diagnostic methods share a common starting point: faults in an IM will inevitably create asymmetries, which are reflected in its magnetic field. These asymmetries manifest in the motor's electrical, magnetic, and mechanical signal waveforms. By applying the appropriate signal processing techniques, depending on the nature of the signal, the effects of the fault can be identified. These effects typically appear as unwanted harmonics or irregularities in the signal, which provide clear indicators of the fault's presence and severity.

The process of diagnosing faults in IMs involves several critical factors that must be considered to ensure an effective and timely response. A diagnostic procedure typically involves multiple

steps, each aimed at understanding the fault's nature, severity, and potential impact on the system. As shown in Figure 4.1, key characteristics of a diagnostic procedure include the speed of diagnosis, severity estimation, financial cost, and whether the process is conducted online or offline. Additionally, the level of intrusion, the type of monitoring equipment used, and the decision-making process—whether automatic or manual—are also important aspects to consider. Each of these factors contributes to the overall efficiency and effectiveness of the diagnosis, guiding maintenance strategies and helping to determine the best course of action for service or replacement.

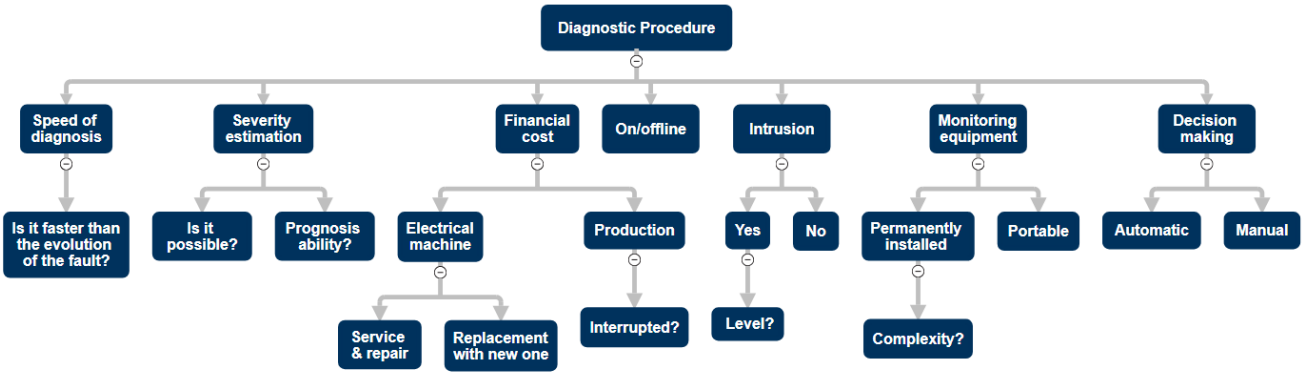

FIGURE 4.1: Diagnostic Procedure Characteristics [58]

4.2 Motor Current Signature Analysis (MCSA)

One of the most widely used diagnostic techniques is Motor Current Signature Analysis (MCSA) [6], which involves analyzing the harmonic content of the stator current. This method is primarily utilized for monitoring and performing spectral analysis of the stator current mostly in steady-state operation, but it can be also used in transient conditions. MCSA is favored by many diagnostic engineers due to its low implementation cost, minimal equipment requirements, and ability to provide continuous remote and online monitoring. Its cost-effectiveness and versatility make it an essential tool for identifying faults in IMs in real-time.

However, despite its effectiveness, MCSA has shown several limitations in certain specific applications. As a result of its widespread use, its drawbacks have become more evident, particularly in contexts where its general approach may not be ideal. This has led many researchers to propose alternative, more specialized signal processing techniques to address these limitations. The primary issue with MCSA stems from its broad application across diverse scenarios, as no single diagnostic tool can excel in every situation. Consequently, more tailored methods are being developed to enhance accuracy and reliability in areas where MCSA falls short.

4.2.1 Faulty Diagnostic Conclusions

False Positive

Sometimes, the use of MCSA can lead to incorrect diagnostic conclusions due to the aforementioned reasons. In some cases, the motor may be identified as faulty (false positive) when, in fact, it is completely healthy. Such errors often arise in situations where external factors, like load torque oscillations, introduce interference into the signals being analyzed. Another contributing factor is magnetic anisotropy, which causes fluctuations in the motor's rotating magnetic field, distorting the diagnostic results.

Additionally, physical components like the cooling fan and rotor cooling axial ducts can also interfere with the motor's current signals. Specifically, when the number of axial ducts matches the number of magnetic poles in the motor, signal disturbances are more likely to occur [59]. Similarly, the number of fan blades can introduce harmonic distortions in the electrical signals, further complicating the analysis and potentially leading to false diagnostic outcomes.These interferences highlight the limitations of MCSA and the need for specialized techniques in certain applications to avoid such diagnostic errors.

False Negative

In more critical and costly scenarios, the motor may be mistakenly considered healthy when, in fact, it has an underlying fault that, if left undetected, could eventually lead to complete motor failure. These false negatives are especially dangerous because they give a false sense of security, delaying necessary repairs and increasing the risk of catastrophic damage. One common cause of such false negatives is non-adjacent rotor bar breakages, which can be difficult to detect using the MCSA. When two broken bars are positioned at half a pole pitch from each other, their magnetic asymmetries effectively cancel each other out, causing the harmonic distortion they would normally produce to disappear. As a result, the harmonic index, which is typically used for fault detection, becomes undetectable. This is one of the reasons why this thesis proposes a more reliable fault detection method, which will be discussed in later sections. Additionally, outer bar breakages in double-cage rotors can also go undetected, further complicating accurate diagnostics.

It has also been demonstrated that diagnosing the motor under no-load or light-load conditions can lead to false negative results, as the motor's faults may not fully manifest under such conditions. Similarly, misestimating the motor's speed can mask underlying faults, further contributing to inaccurate diagnostics. These challenges underscore the need for more precise and reliable fault detection methods to prevent costly and dangerous failures.

4.2.2 Harmonic Index

Rotor Fault Detection

By monitoring the stator current in steady-state operation and performing spectral analysis using FFT (Fast Fourier Transform), the resulting electromagnetic analysis reveals specific harmonic indices near the basic supply frequency f_s, that are key for identifying broken rotor bar and endring faults [60]:

$$f_{bb} = (1 \pm 2ks) f_s \quad , k \in \mathbb{N} \tag{4.1}$$

Additionally, to analyze fault harmonic indices that are close to other stator harmonics, particularly the 3rd and 5th harmonics, the following equation has been shown to effectively identify the fault indices [61]:

$$f_{bb2} = \left[\frac{k}{p}(1-s) \pm s \right] f_s \quad , \frac{k}{p} \in \mathbb{N} \tag{4.2}$$

Eccentricity Detection

Based on the interaction between rotor slots and poles in three-phase IMs, it has been established that the frequency index of these faults can be determined using the following formula [62]:

$$f_{ecc} = \left[(R \pm n_d) \left(\frac{1-s}{p} \right) \pm 2n_{sa} \pm n_{ws} \right] f_s \tag{4.3}$$

Where R represents the number of rotor bars, and n_d is known as eccentricity order: If $n_d = 1, 2, 3...$ dynamic eccentricity is present, while $n_d = 0$ indicates that there is only static eccentricity. The constant n_{sa} corresponds to the motor's saturation levels, while n_{ws} is related to the characteristics of the stator windings.

Additionally, the RSH (Rotor Slot Harmonics) or PSH (Principal Slot Harmonics) that occur in IMs can also be expressed by the same equation 4.3 where $n_d = 0$ and without any saturation ($n_{sa} = 0$) [62]:

$$f_{PSH} = \left[R \left(\frac{1-s}{p} \right) \pm n_{ws} \right] f_s \tag{4.4}$$

As we can see from 4.3 and 4.4, the eccentricity harmonic index does not always hold true for fault detection. It has been shown that induction motors naturally exhibit PSH when the rotor

slot number is an integer multiple of the motor's pole number. This relationship is expressed by the following equation [63]:

$$R = 2p\left[3(m \pm q) \pm r\right], \quad m \pm q = 0, 1, 2, 3..., \quad r = 0, 1 \tag{4.5}$$

By that, we draw the conclusion that the equation 4.3 becomes unreliable for detecting eccentricity in certain conditions. Specifically, when the motor naturally exhibits PSH, it becomes impossible to detect static or dynamic eccentricity. In such cases, only mixed eccentricity can be detected, making the equation unsuitable for distinguishing pure static or dynamic eccentricity.

In the case of mixed eccentricity, an additional frequency component will appear in the stator line current spectrum, expressed as [64]:

$$f_{ecc2} = \left[f_s \pm k f_r\right], \quad k = 1, 2, 3..., \quad f_r = \frac{1-s}{p} f_s \tag{4.6}$$

This equation highlights the presence of new harmonic components that emerge as a result of mixed eccentricity, with f_r representing the rotor's rotational frequency and k as an integer multiplier that captures higher order side-band harmonics.

Stator Fault Index

To detect stator winding faults, the following equation was proposed [65]:

$$f_{sc} = \left(k_r R \frac{1-s}{p} \pm 2k_{sat} \pm k_s\right) f_s \tag{4.7}$$

In this equation, k_r, k_{sat} and k_s are integers representing the rotor, saturation, and stator, respectively, and R is the number of rotor slots.

4.3 Torque Analysis

Monitoring the output torque is another effective method for detecting rotor electrical faults. Fault signatures from broken bars can be identified using FFT analysis of the torque signal, and are represented by the following equation [66]:

$$f_{bb} = 2ksf_s \tag{4.8}$$

Where k is a positive integer. In addition to this, broken bars generate distinctive signatures around 300 Hz. Even in the absence of a fault, harmonics are typically observed in this frequency range due to the interaction between the stator and rotor fields. However, in the presence of a broken bar fault, these harmonics become more pronounced and can be expressed by the following equation [66]:

$$f_{bb2} = 300 \pm 2ks f_s \tag{4.9}$$

Diagnosis within this frequency range is particularly advantageous because it is less influenced by variations in motor speed and slip, simplifying the identification of faults. This stability makes it a valuable tool for reliable fault detection.

4.4 Magnetic Flux Analysis

Magnetic fault analysis primarily relies on the fact that the presence of a fault creates asymmetry in the magnetic field. Consequently, numerous studies have proposed monitoring the magnetic flux using flux sensors, focusing on either radial, axial, or both flux components [67, 68, 69]. The magnetic flux can be detected either from the air-gap inside the motor (between rotor and stator) or outside capturing the stray flux leakage. The first method is highly intrusive, requiring the motor to be opened for sensor installation, or the sensor must be integrated during the manufacturing process. In contrast, the second method is non-intrusive, as it involves detecting the stray flux by placing the sensor on the motor's frame without disrupting the motor's operation. However, the drawback of stray flux monitoring is that it captures slightly weaker signals because the sensor is positioned outside the motor frame, resulting in weaker signals compared to airgap flux sensors, which are located closer to the source of the flux.

In most cases, MCSA signatures are also detected in the radial flux spectrum, as the flux is directly influenced by the current. This correlation further supports the use of flux monitoring as a valuable diagnostic tool for identifying magnetic faults, reinforcing the connection between current analysis and magnetic field behavior.

4.4.1 Stray Flux Signature Analysis (SFSA)

The stray flux in a motor consists of two distinct components that escape in different directions: the radial leakage flux, which exits outside the yoke, and the axial flux, which leaks through the rotor shaft. External search coils are strategically positioned to capture these flux leakages. When a sensor is placed on the radial surface of the motor frame, it can measure stray flux in both the axial and radial directions [68, 69]. Alternatively, if the sensor is positioned on the axial end surface, enclosing the shaft, it will capture the axial stray flux specifically [70, 71]

(Figure 4.2). These sensors typically consist of coils with numerous turns to enhance the voltage transformation ratio, thereby improving sensitivity and yielding more accurate diagnostic results.

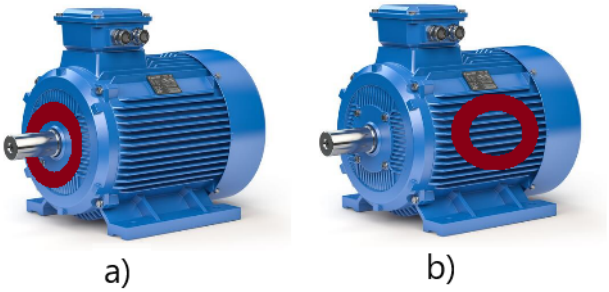

FIGURE 4.2: Sensor placements for detecting: a) Axial Stray Flux b) Radial and Axial Stray Flux [72]

4.4.2 Harmonic Index

As mentioned earlier, the magnetic flux shares the same spectral characteristics as the stator current. The main difference between those two is the existence of odd triplets in the magnetic flux, as well as the homopolar RSH. Those harmonics are not present in the stator current as they are cancelled due to the formation of the windings to create the magnetic poles in space.

The aforementioned equations (4.1 and 4.2) representing the current harmonic content of a motor with broken bars, are seen also in the stray flux leakage detected. A recent study has demonstrated that rotor electrical faults amplify harmonics closely linked to the mechanical speed of the rotor [73]. This relationship is described by the following equation:

$$f_{bb3} = \left[n \pm m \frac{(1-s)}{p} \right] f_s, \quad n, m \in \mathbb{N} \tag{4.10}$$

Additionally, side-bands will appear at these harmonics related to the mechanical speed, as shown in equation 4.10. These side-bands are expressed as:

$$f_{bb4} = \left[n \pm m \frac{(1-s)}{p} \pm 2ks \right] f_s, \quad n, m, k \in \mathbb{N} \tag{4.11}$$

4.5 Zero-Sequence Method

The Zero-Sequence method is applied in conjunction with the previously mentioned techniques, such as MCSA and SFSA, to provide a more comprehensive signature for analysis.

This method enhances diagnostic capabilities because the signal produced is the sum of three phase components—whether current or flux—each separated by 120 electrical degrees.

4.5.1 Zero-Sequence Current

The ZSC is calculated as the direct sum of the three-phase instantaneous currents, which can be monitored in both star and delta-connected motors:

$$i_{ZSC} = i_a + i_b + i_c \tag{4.12}$$

For delta-connected induction motors, it is necessary to measure all three phase currents individually and then sum the resulting waveforms to obtain the ZSC. However, in star-connected induction motors, if the neutral point is available, the ZSC can be directly monitored through the neutral current, requiring only a single current sensor. If the neutral is not connected, the current may be zero, and no useful information can be gathered from the ZSC measurement in this case [74].

Past works have proven that the analysis of ZSC is superior to the analysis of a single current signal, especially for detecting broken bar fault signatures (Equation 4.2). This happens because the fundamental of the ZSC exists at $3f_s$. The main advantages recorded for searching for side-bands around the fundamental ZSC harmonic, based on the signature expressed by equation 4.2, are the following [75]:

- The fault generates two main harmonics in the ZSC ($3f_s - 2sf_s$ and $3f_s - 4sf_s$) instead of one in the MCSA ($f_s - 2sf_s$).
- Since the fundamental frequency of the Zero-Sequence Component (ZSC) occurs at three times the frequency of the current's fundamental, the signal amplitude is significantly higher. This increase in amplitude, in accordance with Faraday's law of induction, enhances the quality of the signal. As a result, the higher amplitude provides a clearer and more robust signal for processing, making it easier to detect and analyze faults with greater accuracy.
- As the frequency increases, the skin effect in the rotor becomes more pronounced, causing current to concentrate near the surface of the rotor bars. This intensifies the magnetic asymmetry near the air gap, which in turn enhances the fault signatures. The stronger magnetic asymmetry at higher frequencies results once again in more distinct and detectable signals for fault diagnosis.

4.5.2 Zero-Sequence Flux

The ZSF is calculated from signals obtained by three radial stray flux search coils, symmetrically positioned around the motor to create a 120-degree electrical phase difference. Compared to the ZSC, the ZSF offers similar advantages, with the added benefit of providing additional fault signatures. The conclusions drawn from this method are based on the same signature equation 4.2, which forms the foundation of this study. A detailed discussion of these conclusions, along with the results from the signal processing, will be presented in Chapter 7.

4.6 Transient Current Signature Analysis

When the motor accelerates from a standstill to its steady-state operation, the transient phase can be analyzed to gather valuable diagnostic insights. During this period, fault-related frequency components shift over time, and by tracking their movement, different diagnostic conclusions can be made. Although this method is less practical for many applications—since stopping and restarting a motor to capture its transient signal can be costly—it enables the detection of faults that may not be as evident during steady-state operation and avoid problems that MCSA or other methods may present.

This fault diagnosis method can be applied to current signatures captured during the motor's transient operation. Once captured, the current signal is analyzed using advanced signal analysis techniques, specifically time-frequency transforms. Unlike traditional methods that aim to detect a harmonic at a fixed frequency, this approach focuses on identifying the evolution of fault harmonics over time during the transient state. This evolution creates distinctive patterns that are strongly associated with specific faults, offering a more reliable diagnosis compared to conventional tools.

For instance, in the case of broken rotor bars, a characteristic 'V' shape appears in the time-frequency analysis of the starting current, a signature unique to this fault. Such a pattern would not be present for other types of failures. Each type of fault produces its own unique pattern, allowing for precise fault detection and diagnosis [76].

Chapter 5

Finite Element Analysis

The Finite Element Analysis (FEA) is a numerical method widely used in engineering to solve complex problems by approximating solutions based on a model's data. In FEA, the physical domain is broken down into smaller, discrete elements, and the governing equations are converted into a finite set of variables. The solution is then calculated independently for each element, providing a highly detailed and precise approximation of the system's overall behavior. This technique is extensively applied across various fields, including stress analysis, heat transfer, fluid dynamics, and, most notably, electromagnetic fields, which is the focus of this analysis [77].

In the case of IMs, Simcenter MAGNET, a leading FEA tool, is used to solve the motor's differential equations by discretizing the motor's domain into a grid of finite elements. This software allows for accurate simulation of the motor's electromagnetic behavior by breaking the space within the motor into finite elements and solving the corresponding differential equations in each one. The solution within each element is approximated by linear or higher-order polynomial functions, which adapt to the boundary and initial conditions of the problem.

During this process, the solution for each element is influenced by adjacent elements, and iterative computations refine the value at the center of each element. Once the individual solutions are computed, they are assembled to form a global solution that accurately represents the motor's overall electromagnetic behavior. This method captures the intricate interactions within the motor and ensures a comprehensive understanding of its performance.

5.1 FEA and Fault Diagnostics

The use of non-invasive condition monitoring and diagnostic techniques has become a state-of-the-art approach to enhancing the reliability of electrical machines. One critical aspect of the diagnostic process is the study of asymmetrical magnetic fields in induction motors (IMs). A reliable diagnostic method must be rooted in a comprehensive understanding of the machine's electrical, magnetic, and mechanical behavior in both healthy and faulty states [60].

The primary goal of computer simulations, particularly FEA, is to model the magnetic field distribution and operating characteristics of the motor in order to predict changes in performance due to various faults. By simulating different fault conditions, FEA enables the anticipation of how changes in motor parameters affect overall performance. These simulation results play a crucial role in accurately interpreting measured data during diagnostic procedures, which form a key part of a motor's supervisory and maintenance system [78].

As mentioned earlier, FEA is a highly reliable method for the modeling and analysis of IMs. However, certain limitations must be taken into account. One of the most significant drawbacks is that FEA provides an approximation of the motor's behavior rather than an exact representation. This is due to the fact that FEA relies on discretizing the motor's domain into finite elements, and the accuracy of the solution is dependent on the size and number of these elements (Figure 5.1). In practice, it is impossible to model the entire system with infinite precision, so the results are always an approximation influenced by factors such as mesh density, boundary conditions, and numerical rounding errors. Additionally, FEA requires significant computational resources and time, particularly for complex geometries or detailed simulations, which can limit its practicality in certain scenarios.

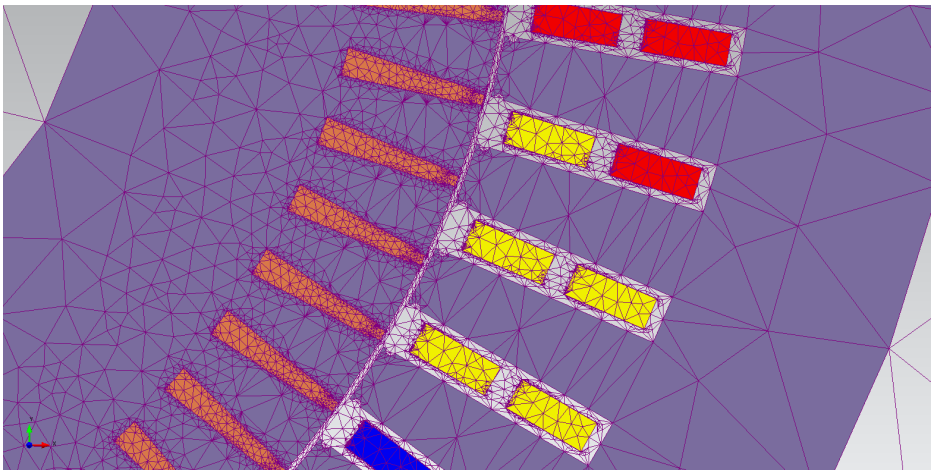

FIGURE 5.1: 2D Mesh of IM model using linear triangular elements using Simcenter MAGNET software

5.2 Mathematical Foundation of Electromagnetic Analysis [79]

Electromagnetic analysis fundamentally revolves around solving Maxwell's equations under given boundary conditions. The differential equations outlined in this section establish the essential principles that govern the boundary-value problems addressed by FEA. As will be demonstrated, vector analysis forms the foundation of electromagnetic theory, providing the tools necessary to model and solve these complex problems accurately.

Maxwell's equations are the foundational set of equations that describe all macroscopic electromagnetic phenomena. These equations can be expressed in both differential and integral forms, but for the purposes of this discussion, we will focus on the differential form. Electromagnetic problems are generally divided into two primary categories based on the nature of their fields: Electrostatic and Magnetostatic Fields and Time-Harmonic Fields. Each category governs specific aspects of electromagnetic behavior and requires different approaches for analysis and solution within the framework of FEA.

5.2.1 General Differential Form

By applying Gauss's and Stokes' theorems, the differential form of Maxwell's equations can be derived. These theorems help translate the integral form of Maxwell's laws into their differential counterparts, making them applicable to points in space where all field quantities and their derivatives are continuous. This allows for a more localized understanding of the electromagnetic field behavior at any given point.

For general time-varying fields, Maxwell's equations in differential form are given by:

Faraday's Law

$$\nabla \times E = -\frac{\partial B}{\partial t} \tag{5.1}$$

Maxwell-Ampere Law

$$\nabla \times H = \frac{\partial D}{\partial t} + J \tag{5.2}$$

Gauss's Law

$$\nabla \cdot D = \varrho \tag{5.3}$$

Gauss's Law - Magnetic Field

$$\nabla \cdot B = 0 \tag{5.4}$$

Equation of Continuity

$$\nabla \cdot J = -\frac{\partial \varrho}{\partial t} \tag{5.5}$$

Where:

E = Electric Field Intensity (V/m)

D = Electric Flux Density (C/m^2)

H = Magnetic Field Intensity (A/m)

B = Magnetic Flux Density (Wb/m^2)

J = Electric Current Density (A/m^2)

ϱ = Electric Charge Density (C/m^3)

5.2.2 Electrostatic and Magnetostatic Fields

When the field quantities do not vary with time, the field is then called static. When this happens the equations 5.1, 5.2 and 5.5, are written as:

$$\nabla \times E = 0 \tag{5.6}$$

$$\nabla \times H = J \tag{5.7}$$

$$\nabla \cdot J = 0 \tag{5.8}$$

While 5.3 and 5.4 remain the same. In this case there is no interaction between electric and magnetic fields. Therefore, there could be either a electrostatic case described by 5.3 and 5.6 or a magnetostatic case described by 5.4 and 5.7, where 5.8 is a natural consequence of 5.7.

Delving deeper in the magnetostatic problem case, there are constitutive relations that describe the macroscopic properties of the medium being considered. For the magnetostatic case this relation is:

$$B = \mu H \tag{5.9}$$

Where μ is the permeability of the medium. This parameter is a tensor for anisotropic media and a scalar for isotropic media. For inhomogenous media it is a function of position, whereas for homogenous media it is a constant.

5.2.3 Vector Potential for Magnetostatic Field [36]

To solve Maxwell's equations, one may convert the first-order differential equations involving two field quantities into second-order differential equations involving only one field quantity. This will be shown below considering the magnetostatic case.

As mentined earlier, the magnetostatic field is governed by 5.4 and 5.7. Equation 5.4 can be satisfied by representing the magnetic flux density B as:

$$B = \nabla \times A \tag{5.10}$$

Where A is called the magnetic vector potential. By substituting 5.10 into 5.7 and with 5.9, that yields the second-order differential equation:

$$\nabla \times \left(\frac{1}{\mu} \nabla \times A \right) = J \tag{5.11}$$

For a linear and isotropic medium 5.11 becomes:

$$-\frac{1}{\mu} \nabla^2 A = J \tag{5.12}$$

In the case of time-harmonic problems the magnetic fields are time varying. For this reason there will be eddy currents in every medium that is characterised by a conductivity value σ. The electric current density J is connected to the electric field intensity E by the constitutive relation:

$$J = \sigma E \tag{5.13}$$

By combining 5.10 to 5.1 the resulting equation is:

$$\nabla \times E = -\nabla \times \frac{\partial A}{\partial t} \tag{5.14}$$

Finally, by combining the equations 5.12 and 5.14 the result is:

$$-\frac{1}{\mu} \nabla^2 A = J - \sigma \frac{\partial A}{\partial t} \tag{5.15}$$

When analyzing a motor operating under load conditions, the kinetic equation comes into play:

$$T = J\frac{\partial^2\theta}{\partial t^2} \tag{5.16}$$

Where J is the moment of inertia , θ is the angular displacement and T is the torque. The torque is expressed as the summation of the following:

$$T = T_{em} + T_L + T_F \tag{5.17}$$

Where T_{em} is the electromagnetic torque, T_L is the load's torque and T_F is the opposing torque due to friction.

5.3 FEA Implementation via Software

The simulation analysis in Finite Element Analysis (FEA) can follow either a linear or non-linear approach, depending on the material properties and problem complexity. In linear analysis, the simulation software uses a fixed relative permeability value, defined by the user for each material. However, in non-linear analysis, the program incorporates the material's B-H curve, allowing for a more accurate representation of magnetic saturation effects.

A crucial aspect of the simulation process is the inclusion of an external circuit that reflects the motor's actual circuit, ensuring accurate modeling of the motor's behavior. The key steps involved in implementing FEA for the analysis of an IM are outlined as follows:

1. **Geometry Definition**: The process begins by defining the geometry of the IM within a graphical environment, either as a 2D or 3D model, depending on the analysis requirements. This step is essential for representing the physical structure of the motor accurately.

2. **Mesh Generation**: Once the geometry is defined, the model is subdivided into smaller, finite elements by creating a mesh. The mesh resolution can be adjusted to balance accuracy and computational cost. At this stage, the type of analysis (linear or non-linear) is selected, and additional parameters, such as material properties and boundary conditions, are input into the model.

3. **Solver Execution**: After preparing the mesh and entering all relevant data, the solver takes over. This is the computational engine that solves the system of equations governing the motor's behavior, using numerical methods to compute electromagnetic fields, currents, and other critical parameters.

4. **Post-Processing**: Once the solution is obtained, the results are analyzed using a post-processor. This step allows for the interpretation and visualization of data, such as field distributions, torque, and losses. Post-processing tools help evaluate the motor's performance under various conditions, facilitating informed decisions about design improvements and fault detection.

These steps collectively form the workflow for performing FEA in the analysis of induction motors, ensuring that the results are both accurate and actionable.

Chapter 6

Motor Modelling

6.1 Motor Characteristics

This chapter focuses on the simulation model characteristics of a high-voltage industrial IM using advanced modeling techniques. The motor under investigation is a squirrel-cage IM, a widely used motor type in industrial applications that require constant speed, self-starting capabilities, and low maintenance. The key characteristics of the simulated motor are detailed in Table 6.1.

Parameter	**Rotor Cage IM**
Voltage	6.6 kV
Power	1.14 MW
Current	117.4 A
Pole Pairs	3
Stator Slots	54
Rotor Slots	70
Stator Connection	Star

TABLE 6.1: Motor's Rated Parameters

6.2 Model Geometry

The geometry of the model, as shown in Figure 6.1, was designed using Simcenter MAGNET software. The air gap between the stator and rotor was modeled as multiple air layers to ensure precision in the electromagnetic analysis. Additionally, an external air layer was included around the stator core to simulate open-space conditions and further enhance the accuracy of the simulation.

The air gap between the rotor and stator core was divided into three distinct sub-layers, each with specific characteristics. The layer closest to the rotor was part of the simulation's motion component, capturing the dynamic interaction between the rotating rotor and the stator. The middle air-gap layer was modeled as a standard ring, representing the typical separation between the rotor and stator. Lastly, the layer adjacent to the stator core represented both air and insulation, serving as a dual-purpose component: it accounted for the air gap as well as the insulation material that fills the stator slots.

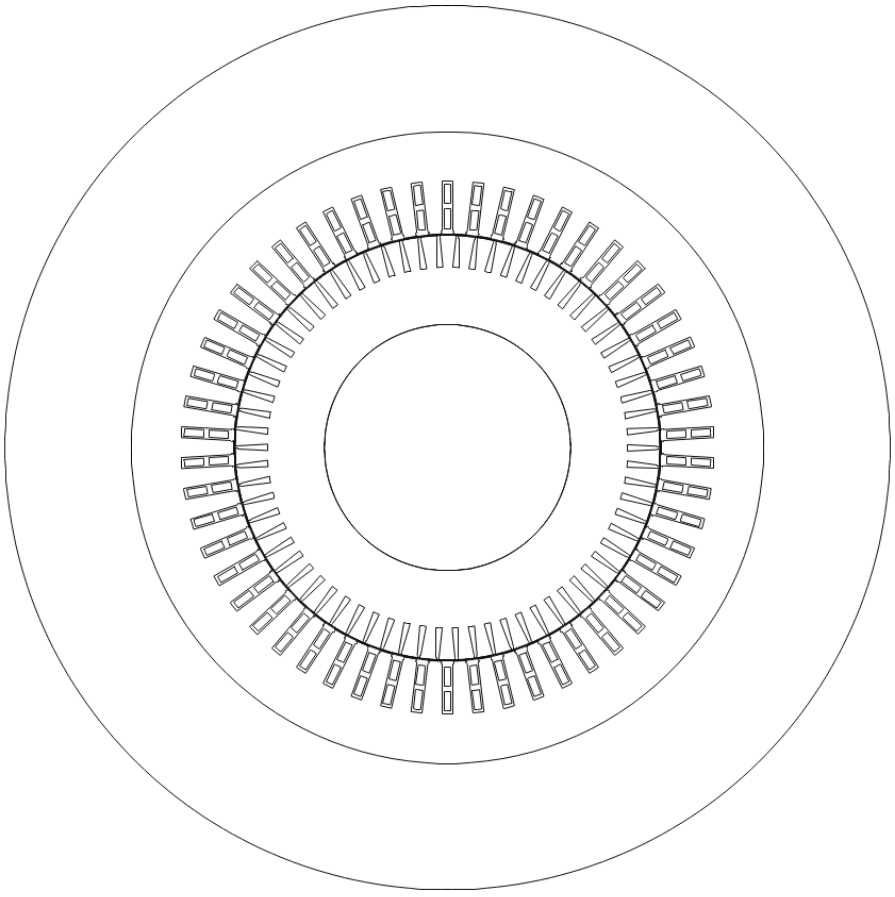

FIGURE 6.1: IM model outline

6.3 Rotor Cage IM Modeling Tutorial - Simcenter MAGNET

The first step after launching Simcenter MAGNET is to create a new .mn project and set the length unit to millimeters. This can be done by right-clicking on **project_name.mn** → **Properties** → **Units** → **Length** and then choose **millimeters** from the drop-down menu.

6.3.1 Outline Creation

Outer and Inner Diameters

To begin the motor design and create the outline of the IM (Figure 6.1), the outer and inner diameters of the stator and rotor must first be defined, along with the circles that will divide the rotor, air gap, and stator. Based on the desired air gap length, adjustments must be made to the rotor and stator radii, reducing each by half of the total air gap length. For example, in this model, with a rotor radius of 280 mm and a stator radius of 430 mm, to achieve a required air gap of 1.8 mm, 0.9 mm should be subtracted from both the rotor and stator radii. To ensure more accurate results, these adjustments should be applied to the core lengths, not the slot lengths, as this will provide a more precise representation of the motor's geometry and air gap characteristics.

In the **Draw** menu, select **Circle** and specify the radius and center point using the keyboard input bar (first, enable keyboard input bar in **Tools** → **Keyboard Input Bar**), or by clicking with the mouse.

Stator and Rotor Slots

For the stator slot design, start by drawing a line from the center origin through to the outer diameter. Select the **Add Line** command from the **Draw** menu. Then, define the center point of origin through the keyboard input bar. Using the keyboard input twice, create the line from the position (0,0) to the stator's outer diameter at (0,xxx). This initial line will serve as the reference point for the stator slot creation.

Next, create half of the stator slot. Once complete, select the edges of the half-slot and use the **Mirror Edges** option (**Draw** → **Mirror Edges**). to reflect the slot design and complete the full stator slot (Figure 6.2).

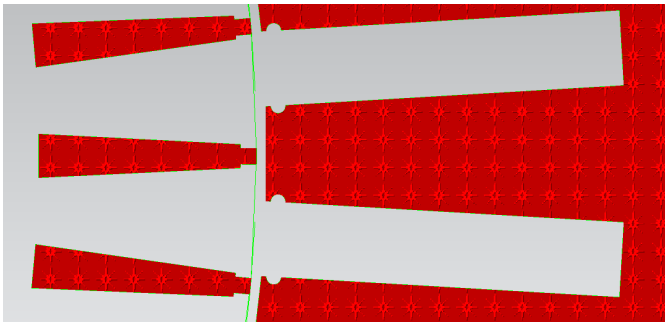

FIGURE 6.2: Rotor Slots and Stator Teeth (highlighted)

To create the remaining stator slots more efficiently, use the **Rotate Edges** option. Select the entire prototype stator slot and then choose the **Rotate Edges** option from the Draw menu. Specify the rotation angle and the number of copies (stator slots). For this model, the rotation angle is 6.667 ° as the stator slots must be evenly spaced ($\frac{360°}{54} = 6.667°$), where 54 is the total number of stator slots.

For the creation of the rotor slots, the same steps used for the stator slots are followed. First, using the reference line, design half of the rotor slot, mirror the edges to complete the full slot, and use the **Rotate Edges** option to create the remaining rotor slots. Adjust the rotation angle and number of copies according to the number of rotor slots to ensure even spacing. (Figure 6.2).

Double-layer Stator Windings

Following a similar process to the creation of the stator and rotor slots, the windings for the double-layered stator slots are created based on the dimensions provided by the motor's blueprint or user preferences. In this case, each stator slot contains two winding layers—one at the top and one at the bottom. These winding slots are created inside the stator slot, as illustrated in Figure 6.3.

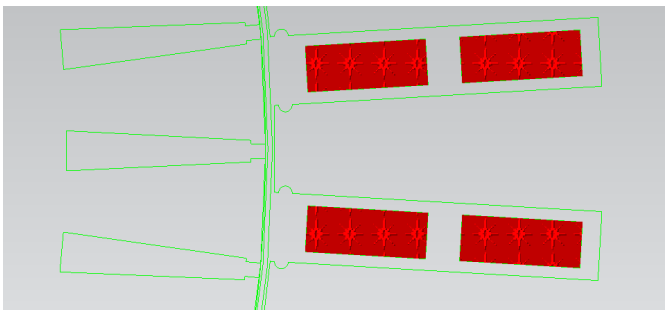

FIGURE 6.3: Double-Layer Windings (highlighted)

Air-Gap

After creating the outer and inner air gap circles, the air gap thickness should be divided into three separate air gap rings, forming three distinct air gap boundaries. To achieve this, two additional circles should be created using the same method, with the keyboard input bar.

6.3.2 Component Creation

Stator and Rotor Component

For this step, first select the **Select Construction Slice Surfaces** option to begin. Start by selecting the stator, then click on the **Make Component in a Line** option and choose the preferred material. Rename the component to 'Stator' (or another preferred name), specify the material and give the active distance. Repeat the same process to create the rotor component.

In the studied model, the material used is M-19 29 Ga. After selecting the material, you can further refine the simulation by adjusting its properties, such as the B-H curve, mass density, hysteresis, thermal conductivity, and other relevant characteristics to achieve the most accurate representation of the motor's behavior.

Rotor Bar and Double-Layer Winding Components

Similarly, create the first rotor bar component following the same steps as outlined earlier. To create the remaining rotor bars, navigate to the **Object** tab and select the rotor bar component. Then, go to the **Model** option and choose **Rotate Components**, specifying both the angle of rotation and the number of copies needed. Use the same approach for creating the double-layer components.

Shaft and Outer Field Components

The shaft and outer field components are created in the same manner as the previously mentioned components. In this model, both the shaft and the outer field are defined as air.

Air-gap and Stator Slot Air Components

Typically, the stator slot that contains the windings includes insulation material. However, in this model, the insulation material is also represented as air. The same applies to the three air-gap layers, which are modeled with air as the material.

Remove Drawings

Once all components are created, click on **Select Construction Slice Edges**, press **Ctrl + A** to select all, and then press **Delete** to remove the drawings.

Motion Component

To specify the moving components for the simulation, first select the shaft, rotor core, rotor bars, and the first air-gap layer closest to the rotor. Then, navigate to the **Model** menu and choose the **Make Motion Component** option. Under the **Source Type**, select **Load Driven**, and in the **Load** menu, define the load characteristics according to the simulation needs. An example of this setup is shown in Figure 6.4.

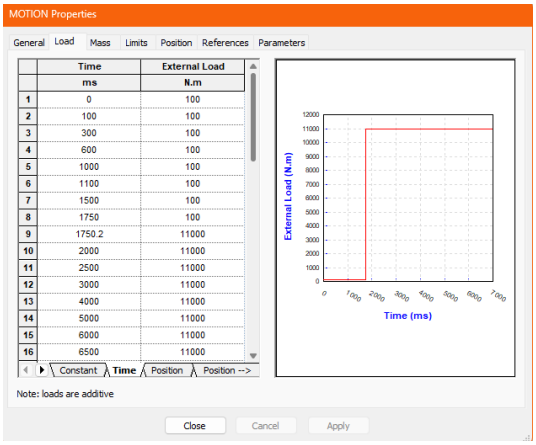

FIGURE 6.4: Load Characteristics in Motion Properties

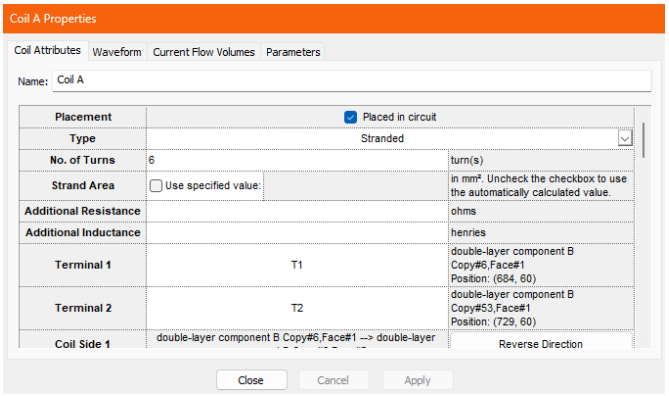

FIGURE 6.5: Coil Properties

6.3.3 Coil Creation

Stator Windings

After creating the coil components, the first step is to differentiate the windings for each phase by assigning a distinct color to each (this can be done by selecting **Override Material Colour** in the component properties). Next, select all windings belonging to the same phase from the **Object** tab, then go to the **Model** menu and choose **Make Simple Coil**. Ensure that after a winding component is selected from one pole, the next winding component selected must be from the opposing pole, alternating back and forth. This guarantees that the coil's direction is consistent for each pole, which is critical for the motor's proper operation. The coil direction can be seen in Figure 6.6

Once the coil is created, select it from the **Object** tab and input the name and the number of turns (Figure 6.5). Same applies for the creation for the coils of the other two phases.

Rotor bars

For the rotor bars, the same method used for coil creation should be applied, but this time as units. Unlike the stator windings, the coil direction in rotor bars is not relevant for the analysis (Figure 6.6).

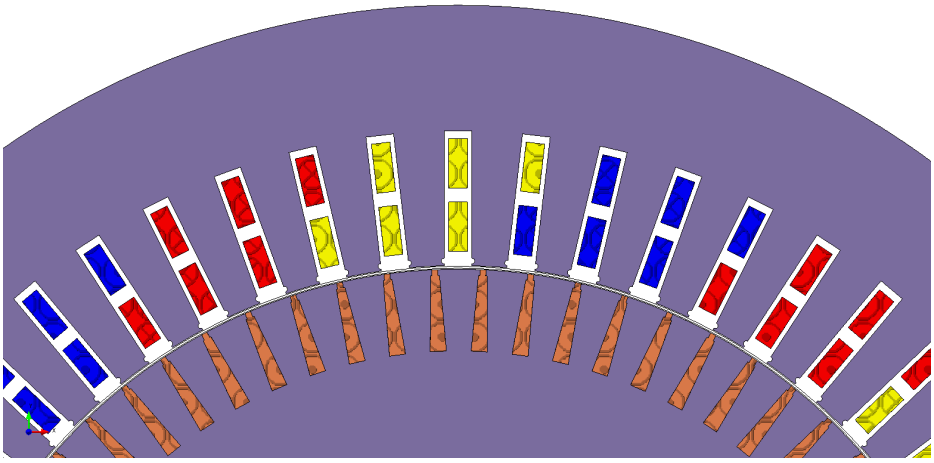

FIGURE 6.6: Stator Coils for Phases A,B,C and Rotor Bars (With Coil Directions)

6.3.4 Circuit View

After creating the circuit view, the previously defined coils can be added to the circuit along with the necessary voltage sources and resistances. The final circuit configurations for both the rotor bars and the stator coils are illustrated below in Figures 6.7 and 6.8, respectively.

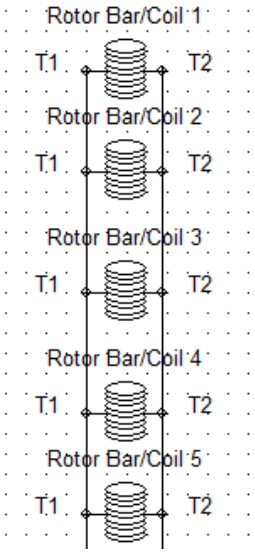

FIGURE 6.7: Rotor Bars in Circuit

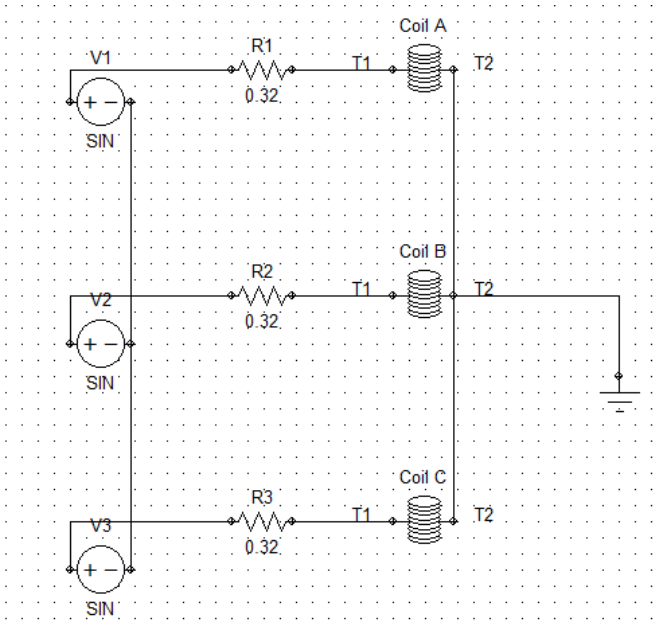

FIGURE 6.8: Stator Coils in Circuit

Figure 6.7 shows the arrangement of 5 rotor bar coils as an example, out of the total 70 rotor bars. All rotor bars follow the same connection pattern as depicted in the figure.

Figure 6.8 depicts the stator coil connections, where each phase is supplied by a voltage source in a balanced three-phase star configuration. Resistors are added in series with each coil to represent the circuit's resistance and to stabilize the simulation. These connections ensure accurate representation of the electrical behavior of the motor during operation.

To achieve the nominal line voltage of 6600 V (RMS) for the star connection, the phase voltage is set to the value of 5388 V. This is calculated using the formula:

$$V_{phase} = \frac{6600\ V}{\sqrt{3}} \approx 3810\ V$$

Since 3810 V is the RMS value of the phase voltage, the peak phase voltage needed for the voltage source is:

$$V_{peak} = 3810\ V \cdot \sqrt{2} \approx 5388\ V$$

This peak voltage is then used in the simulation. Additionally, the frequency of the voltage is set, along with the phase shift for each of the three voltage sources, separated by 120 °. The properties of one of the three voltage supplies are shown in Figure 6.9.

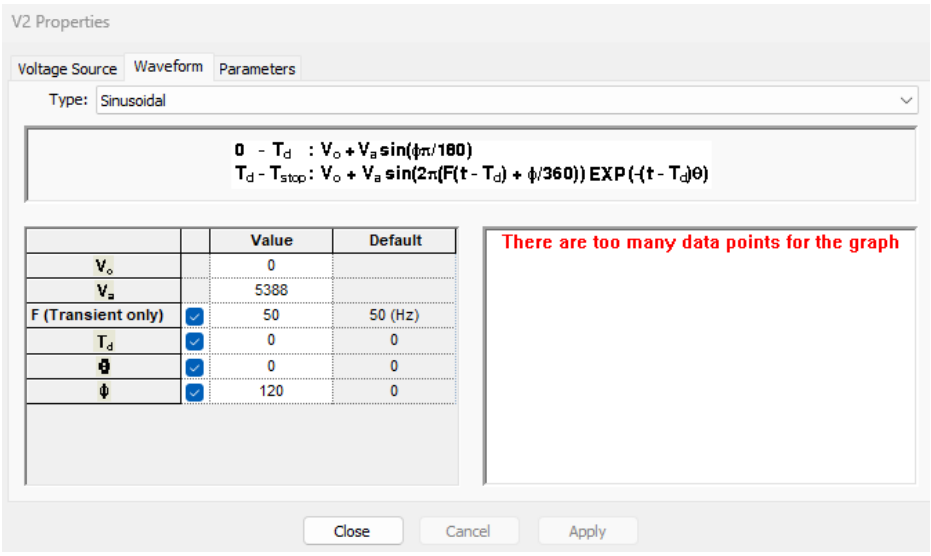

FIGURE 6.9: Voltage Source Properties

6.3.5 Sensor Placement

To detect and calculate the zero-sequence radial leakage flux, three search coils were placed outside the motor model, positioned 120 electrical degrees apart from each other. Each sensor coil has 1000 turns and a diameter of 110 mm. Additionally, these sensors were connected in the circuit with a large resistance of 10^{12} Ohms (Figure 6.10). This high resistance is used to minimize the current flow through the coils, effectively making them act as ideal voltage sensors. This ensures that the measured voltage is directly proportional to the time derivative of the magnetic flux, providing accurate readings of the flux variations without significantly loading the circuit.

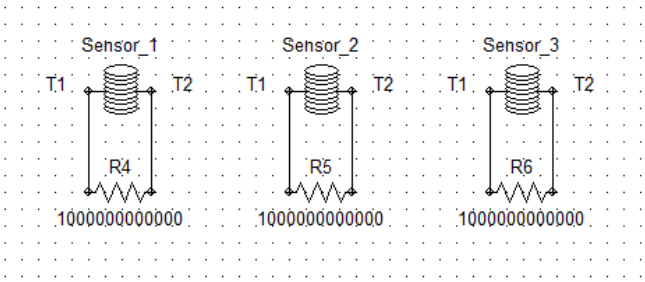

FIGURE 6.10: Sensor Circuit

The final rotor cage IM model with the flux sensors is shown in Figure 6.11 below.

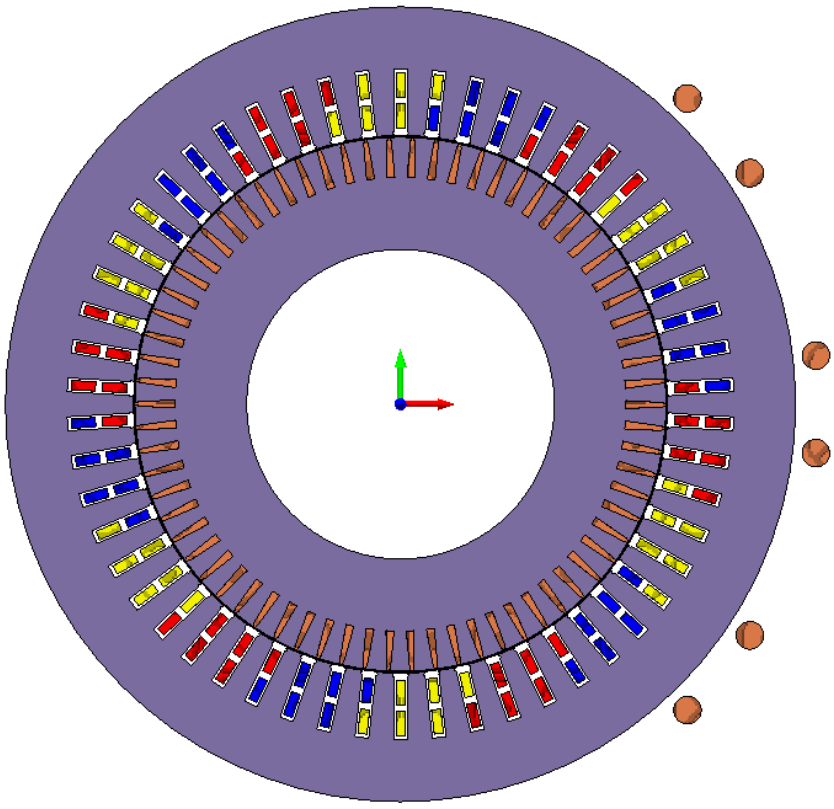

FIGURE 6.11: Final rotor cage IM model with sensors

Chapter 7

Study Results and Analysis

7.1 Studied Cases

The motor instances studied varied primarily based on the number and configuration of rotor bar breakages, as well as the load levels applied. Simulations were conducted for the following conditions: a healthy motor, a motor with a single broken bar, a motor with two adjacent broken bars, two non-adjacent broken bars separated by half a pole pitch (positions 1 and 5), and another case with two non-adjacent broken bars also separated by half a pole pitch (positions 1 and 6). The last two cases are tested because in this motor it is not possible to have exactly half-pole pitch distance between two bars, so the closest distance is selected. Each of these fault scenarios was tested at three different load levels: no-load (100 Nm), representing the torque required to overcome mechanical losses, half the nominal load (5.5 kNm), and the nominal load (11 kNm).

7.2 Performance Characteristics

For the studied cases mentioned above, performance characteristics were first analyzed under steady-state operation using MATLAB signal analysis software, after extracting the data from the simulation software. The results for various fault scenarios at three different load levels are summarized in the tables 7.1, 7.2 and 7.3:

Simulated Cases	I_{ph} (A)	n (rpm)	Slip	P_{in} (MW)	P_{em} (MW)	Performance (%)
Healthy	117.42	996.28	0.0037	1.189	1.142	96.0
1 broken bar	117.81	996.20	0.0038	1.233	1.142	92.6
2 broken bars (adj)	118.19	996.10	0.0039	1.197	1.142	95.3
2 broken bars (1-5)	117.97	996.12	0.0039	1.195	1.142	95.5
2 broken bars (1-6)	117.99	996.13	0.0039	1.195	1.142	95.5

TABLE 7.1: Steady state performance characteristics under nominal load (11 kNm)

Simulated Cases	I_{ph} (A)	n (rpm)	Slip	P_{in} (MW)	P_{em} (MW)	Performance (%)
Healthy	67.69	998.19	0.0018	0.695	0.570	82.0
1 broken bar	67.72	998.15	0.0018	0.698	0.571	81.8
2 broken bars (adj)	67.99	998.11	0.0019	0.700	0.571	81.4
2 broken bars (1-5)	67.79	998.12	0.0019	0.698	0.570	81.7
2 broken bars (1-6)	67.72	998.12	0.0019	0.698	0.570	81.7

TABLE 7.2: Steady state performance characteristics under half load (5.5 kNm)

Simulated Cases	I_{ph} (A)	n (rpm)	Slip	P_{in} (MW)	P_{em} (MW)	Performance (%)
Healthy	39.74	999.92	0.00007	0.432	0.007	1.6
1 broken bar	39.69	999.92	0.00007	0.433	0.007	1.6
2 broken bars (adj)	39.69	999.92	0.00007	0.433	0.007	1.5
2 broken bars (1-5)	39.70	999.92	0.00007	0.433	0.007	1.6
2 broken bars (1-6)	39.7	999.92	0.00007	0.433	0.007	1.6

TABLE 7.3: Steady state performance characteristics under no load (100 Nm)

The data presented in Table 7.1 indicate that the motor's performance remains relatively consistent across all fault conditions under nominal load, with the most significant drop observed in the case of a single broken bar, where efficiency decreases to 92.6%. This suggests that the presence of even a single broken bar has a more substantial impact on the motor's performance compared to other fault scenarios. When comparing these results with those in Table 7.2 and Table 7.3, it becomes evident that load level significantly influences all performance parameters.

The most prominent trend is the reduction in slip as the load decreases, allowing the motor speed to approach synchronous speed. This is especially apparent under no-load conditions, where slip is nearly zero and the motor operates at its closest to synchronous speed. In this scenario, the motor's efficiency drops dramatically to just 1.6%, as it is primarily working to overcome the inherent mechanical losses, represented by the minimal torque requirement of 100 Nm. This highlights the motor's inability to operate efficiently at no-load due to the absence of significant external mechanical work. Overall, this performance analysis demonstrates that the impact of rotor faults becomes less pronounced at lower loads due to the low slip value, while the effect of load on slip and efficiency is substantial, with the motor performing most efficiently at higher loads, where it can fully utilize its capacity.

7.3 Magnetic Flux Distribution

The FEA model of the motor revealed the resulting magnetic flux distribution, showcasing the six poles of the motor. In the healthy motor instance, and during nominal operation, the magnetic flux distribution exhibits a symmetrical and uniform pattern (Figure 7.1). The flux lines are evenly spread across the stator and rotor, forming well-defined magnetic poles that align perfectly with the motor's six-pole configuration. This uniform distribution is indicative of balanced operation, where each pole contributes equally to the electromagnetic torque production.

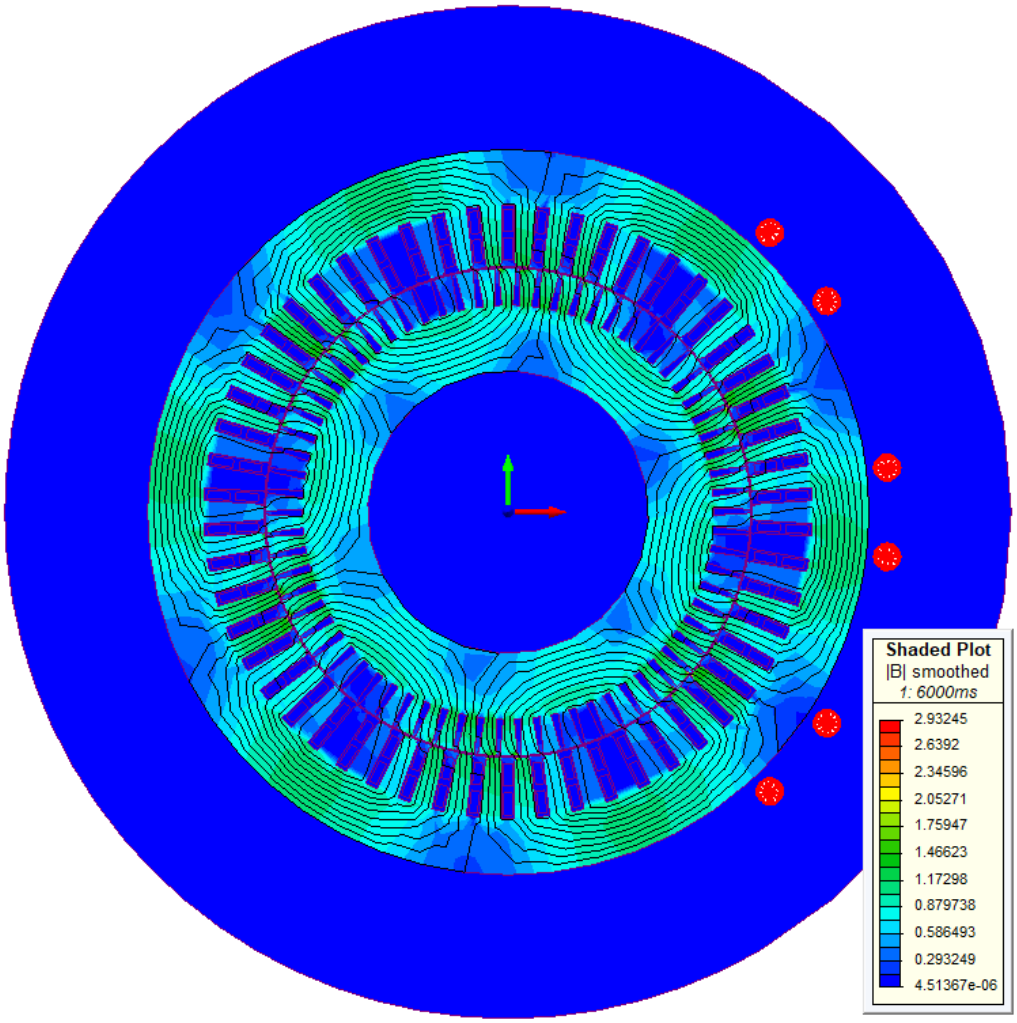

FIGURE 7.1: Spatial distribution of the magnetic flux while at steady state under nominal and healthy operation

7.3.1 Rotor Bar Breakages

When analyzing the FEA model's magnetic field, it was observed that rotor bar breakages significantly increase the flux density in the regions surrounding the damaged bars. This effect is most pronounced during the motor's start-up phase, as the current drawn at this time is nearly six times greater than during steady-state operation. This surge in current is necessary for the motor to overcome inertia and initiate rotation, which requires a substantial amount of energy. The concentrated asymmetry is clearly illustrated in Figure 7.2, for all faulty cases.

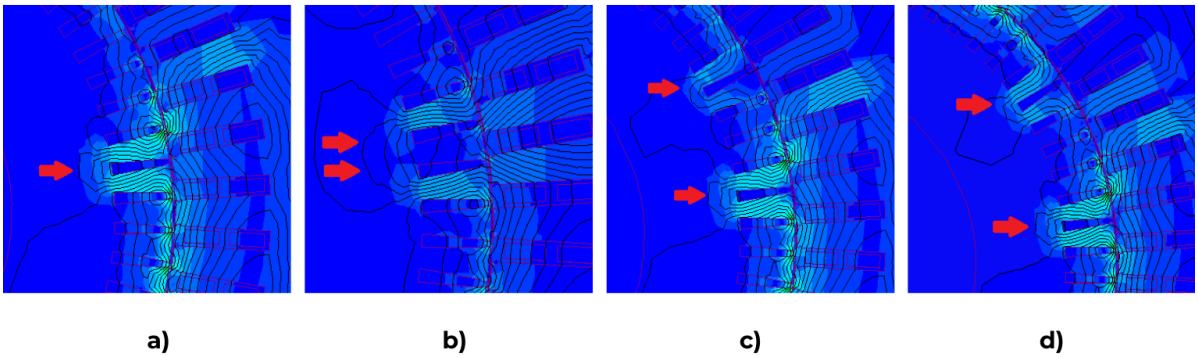

FIGURE 7.2: Spatial flux distribution near the bar breakages: a) 1 broken bar, b) 2 adjacent broken bars, c) 2 non-adjacent broken bars (1-5), d) 2 non-adjacent broken bars (1-6). Broken bars are indicated by red arrows

7.4 Analysis of the Stator Current

The initial step in this study involves a comprehensive analysis of the stator current for all the previously described scenarios. This analysis encompasses both the steady-state and the transient starting phase of the motor, providing insights into the motor's behavior under various operating conditions and fault scenarios.

7.4.1 Current Density in Rotor Bars

The current density distribution in the rotor bars under nominal load can be shown using a field circle graph to visually represent the current density in each rotor bar across the rotor's perimeter. The graph (Figure 7.3) clearly illustrates how the current density increases significantly in the bars adjacent to the broken ones. This localized rise in current density is particularly evident in the scenarios with one and two broken bars, where the neighboring bars compensate for the loss of conductivity. As a result, these adjacent bars experience a much higher current load compared to those further away from the faults. The figure highlights this phenomenon, showing the current density distribution for each tested case, including the healthy motor and the motors with different configurations of broken bars.

However, for loads lower than the nominal 11 kNm, this phenomenon of increased current density in the adjacent bars is not as prominent. The stress on the rotor bars and the corresponding flux distribution become more uniform at reduced loads, minimizing the localized effects observed near the broken bars. This is why the analysis is primarily focused on the nominal operating condition, where the load is high enough to magnify the disparities in current distribution caused by rotor bar faults.

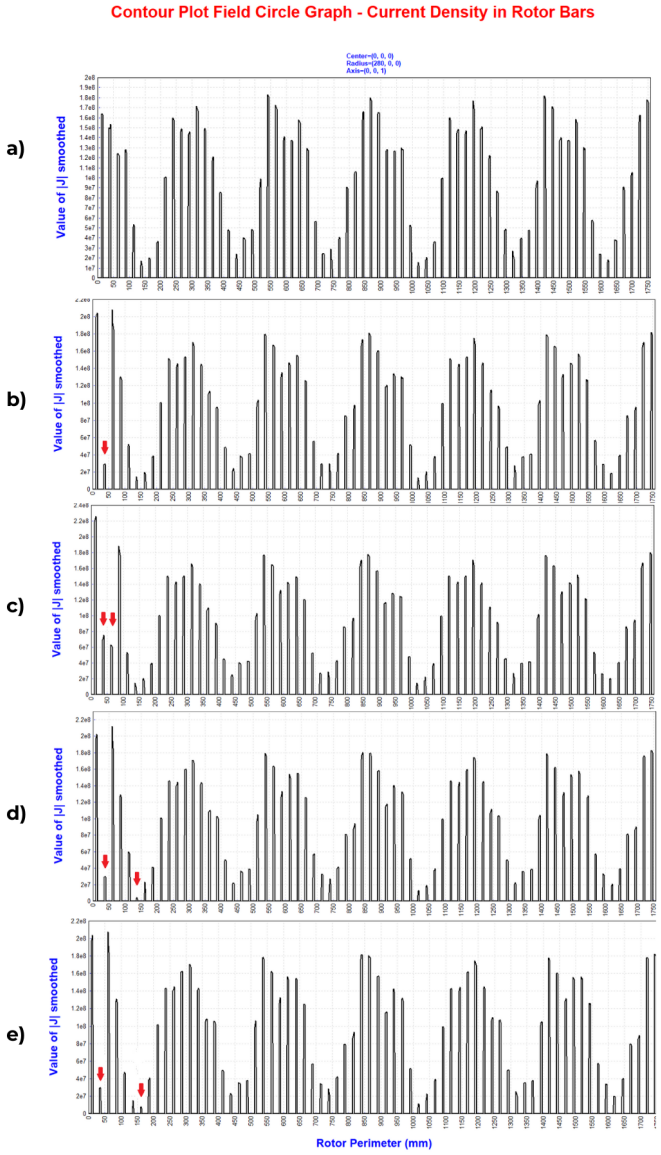

FIGURE 7.3: Absolute current density values of rotor bars at motor start-up (20 ms) under nominal operation for studied cases: a) Healthy, b) 1 broken bar, c) 2 adjacent broken bars, d) 2 non-adjacent broken bars (1-5), and e) 2 non-adjacent broken bars (1-6). Broken bars are indicated by red arrows.

7.4.2 Time-domain Current

Figures 7.4 to 7.6 illustrate the time-domain stator current waveforms for various operating conditions of the motor, including nominal load (11 kNm), half load (5.5 kNm), and no load (100 Nm). The waveforms represent the current response for the healthy motor, as well as for motors with different configurations of rotor bar breakages.

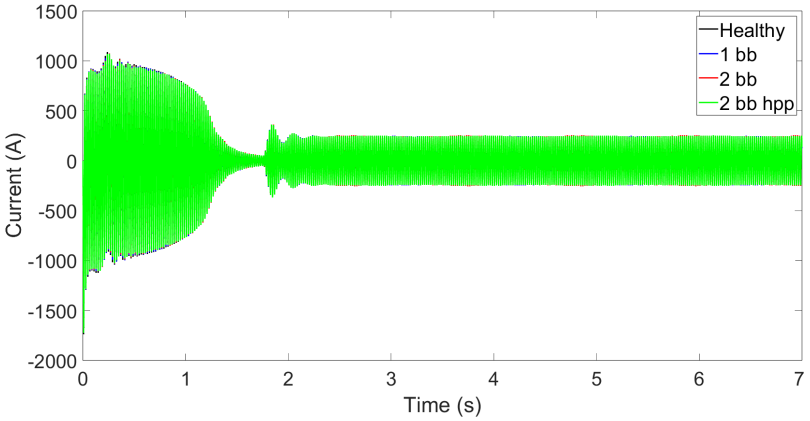

FIGURE 7.4: Time-Domain Stator Current Signal under Nominal Load (11 kNm)

In all three figures, the motor exhibits the same initial starting current and reaches steady-state operation at the same time. Slight asymmetries are visible in the nominal load case (Figure 7.4), becoming less pronounced under half load (Figure 7.5), and virtually indistinguishable under no load (Figure 7.6), where all cases appear identical.

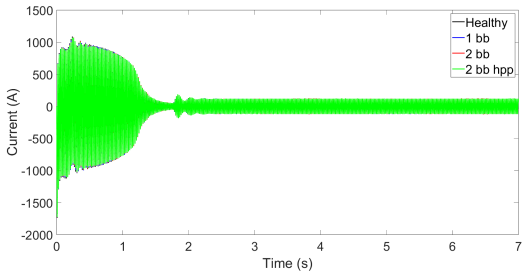

FIGURE 7.5: Time-Domain Stator Current Signal under Half Load (5.5 kNm)

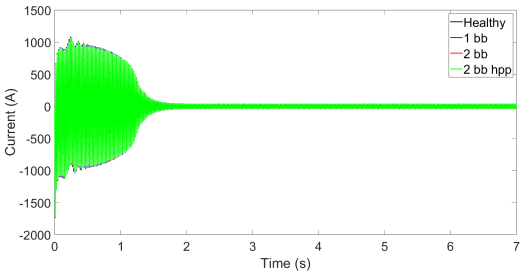

FIGURE 7.6: Time-Domain Stator Current Signal under No Load (100 Nm)

The main difference between the figures lies in the steady-state current drawn by the motor: the current is significantly higher under nominal load, decreases under half load, and is lowest under no load conditions. This observation highlights how the motor's current demand is directly influenced by the load it needs to overcome, with the effects of rotor faults being most apparent under higher load scenarios. Notably, in the nominal load and half load cases, the load is engaged at 1.75 seconds, which causes a visible disturbance in the current waveforms

at this time before they stabilize into their respective steady-state conditions. This additional disturbance is absent in the no-load scenario, indicating the impact of load engagement on the motor's performance and the resulting current fluctuations.

7.4.3 MCSA Results

The MCSA results are represented in Figures 7.7 to 7.9, where the load impact is also shown. The amplitudes of the main broken bar fault signature at $f_s - 2sf_s$ of the nominal operation (Figure 7.7) are shown in the following table 7.4.

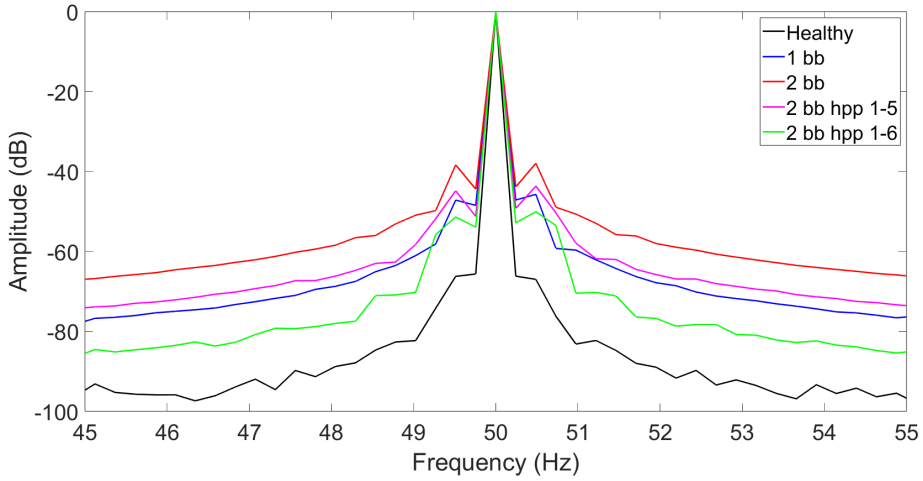

FIGURE 7.7: MCSA under healthy and faulty conditions (11 kNm)

Simulated Cases	$f_s - 2sf_s$
Healthy	-66.24 dB
1 broken bar	-47.16 dB
2 broken bars (adj)	**-38.35 dB**
2 broken bars (1-5)	-44.82 dB
2 broken bars (1-6)	-51.39 dB

TABLE 7.4: MCSA - Left Sideband Amplitudes

The analysis of the right sideband (Figure 7.7) is typically associated with the inertia of the electromechanical system. Therefore, it is not detailed here, although it exhibits similar behavior to the left sideband. The results illustrate how certain faults may be masked, resulting in weak fault signatures with amplitudes even lower than those observed in the case of a single broken bar. Given the empirically established threshold of -42 dB, it is clear that the motor would likely be classified as healthy despite the presence of two non-adjacent broken bars. This highlights the challenges in fault detection using MCSA under these specific conditions, where the severity of the fault might not be accurately represented in the spectral analysis.

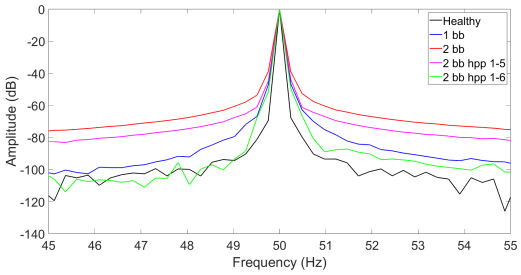

FIGURE 7.8: MCSA under healthy and faulty conditions (5.5 kNm)

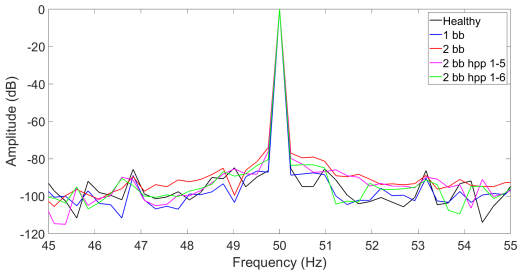

FIGURE 7.9: MCSA under healthy and faulty conditions (100 Nm)

Load Impact

The applied load plays a crucial role in the reliability of MCSA. Specifically, as the load decreases, the rotor current weakens, and the slip frequency reduces. This results in the fault signatures shifting closer to the fundamental frequency, increasing the likelihood of false negative alarms. In the studied industrial IM, which operates at speeds very close to the synchronous speed, broken bars become nearly impossible to detect under no-load conditions (Figure 7.9). As demonstrated in Figure 7.8, MCSA proves entirely ineffective at identifying broken rotor bar faults, regardless of severity, when the motor is operating at half the rated load (5.5 kNm), a scenario that is common in many real-world applications.

7.4.4 Current Analysis during Transients

The Short-Time Fourier Transform (STFT) was applied to all motor scenarios under study to generate the corresponding spectrograms. A window length of 2048 samples was chosen to optimize the performance of the Kaiser filter, with a beta parameter set at 7.95. The signal comprises 14,500 samples with a sampling frequency of 5 kHz.

In the transient analysis under nominal load conditions, the spectrogram of a healthy motor (Figure 7.10) primarily shows the fundamental frequency and the fifth harmonic. However, when a broken bar fault occurs (Figure 7.11), additional harmonic trajectories emerge. Notably, the characteristic V-shaped pattern below the fundamental frequency, defined as $1 - 2sf_s$, becomes evident. Other harmonic trajectories such as $1 + 2sf_s$, $5 - 4sf_s$ and the side-bands of the Rotor Slot Harmonics (RSH) are also clearly observed.

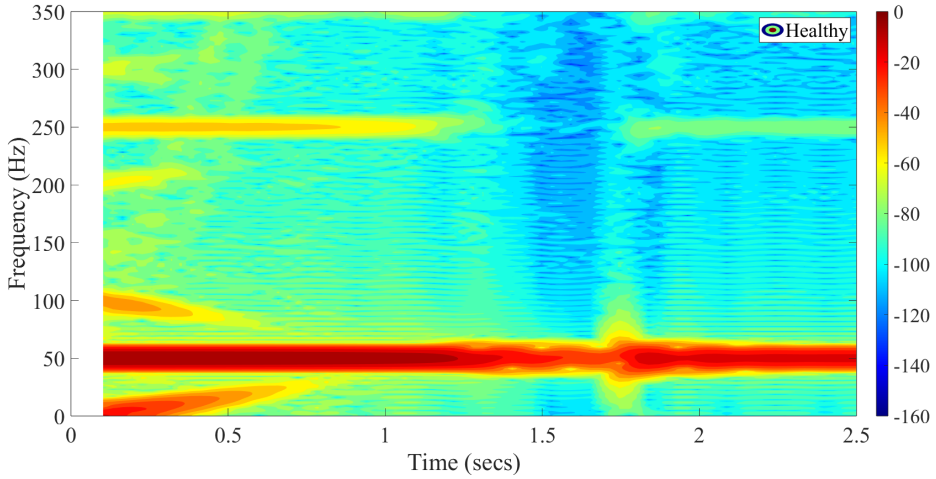

FIGURE 7.10: STFT current spectrogram of studied motor under healthy condition during the start-up transient.

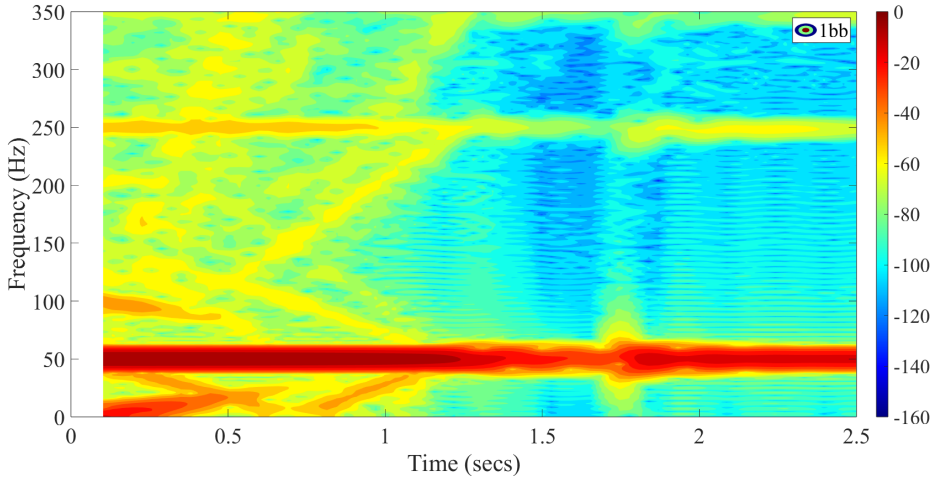

FIGURE 7.11: STFT current spectrogram of studied motor with 1 broken bar during the start-up transient.

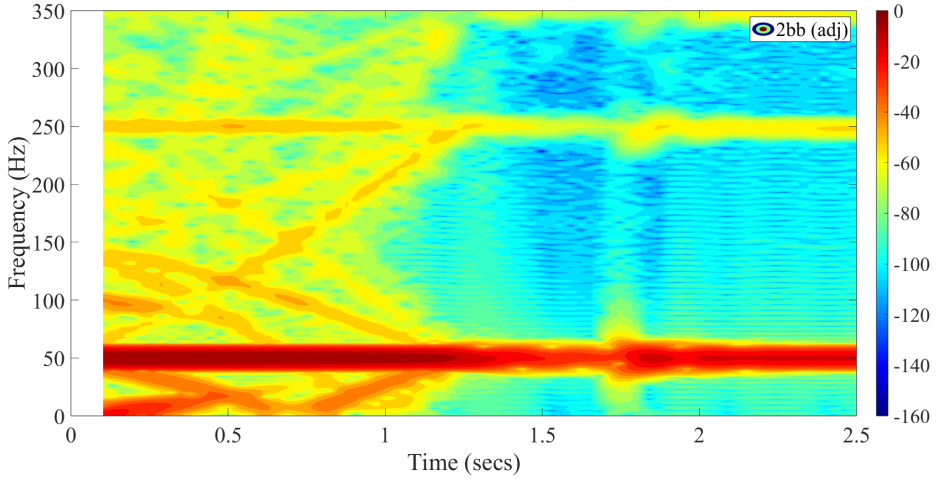

FIGURE 7.12: STFT current spectrogram of motor with 2 adjacent broken bars during the start-up transient.

The amplitude of these harmonic trajectories increases significantly when two adjacent broken bars are present (Figure 7.12). In contrast, for motors with two non-adjacent broken bars, the harmonic trajectories are visible but less pronounced. Specifically, in the case of non-adjacent broken bars positioned at the 1st and 5th slots (Figure 7.13), the trajectories are present but with lower amplitudes. The situation is further exacerbated for the motor with non-adjacent broken bars at the 1st and 6th slots (Figure 7.14), where the harmonic amplitudes are significantly diminished. This observation is critical because in real motors, inherent manufacturing asymmetries can produce similar fault-related signatures even in healthy machines, increasing the risk of misdiagnosis, even with transient analysis.

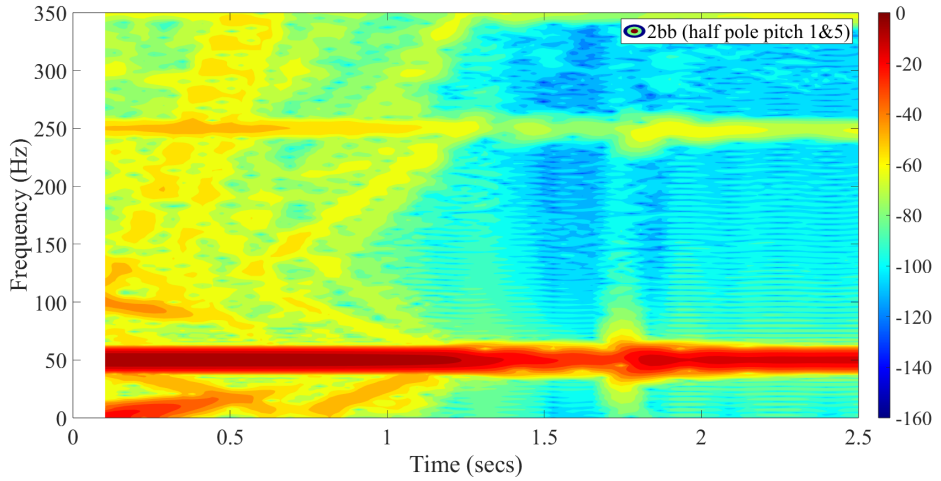

FIGURE 7.13: STFT current spectrogram of studied motor with 2 broken bars (1-5) during the start-up transient.

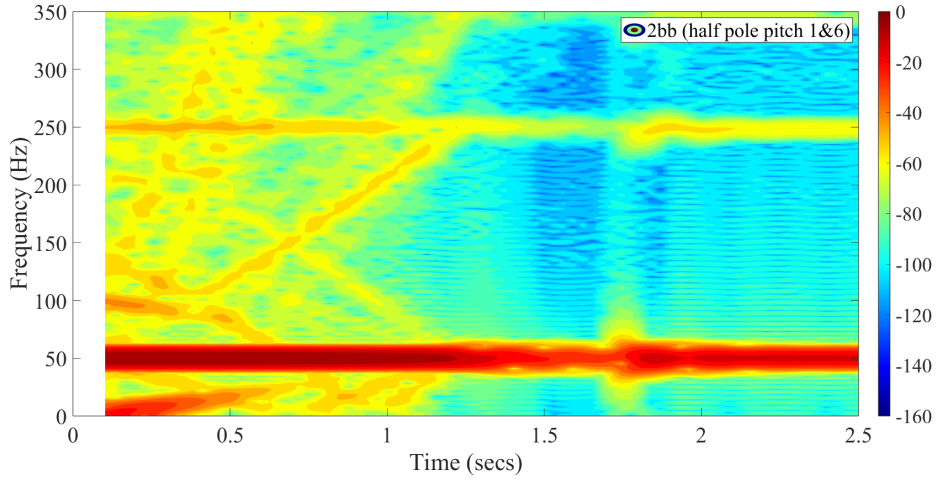

FIGURE 7.14: STFT current spectrogram of studied motor with 2 broken bars (1-6) during the start-up transient.

Load Impact

As illustrated in Figure 7.15, the load impact does not influence the start-up transient since the load is coupled at 1.75 seconds, which is after the transient phase. Consequently, the spectrograms for all load conditions during the start-up phase remain identical to those under nominal conditions. The only noticeable difference occurs after the load is applied, specifically in the half-load scenario, where a slight reduction in disturbance is observed along the fundamental frequency line compared to the nominal load spectrogram. This disturbance is absent in the no-load operation case.

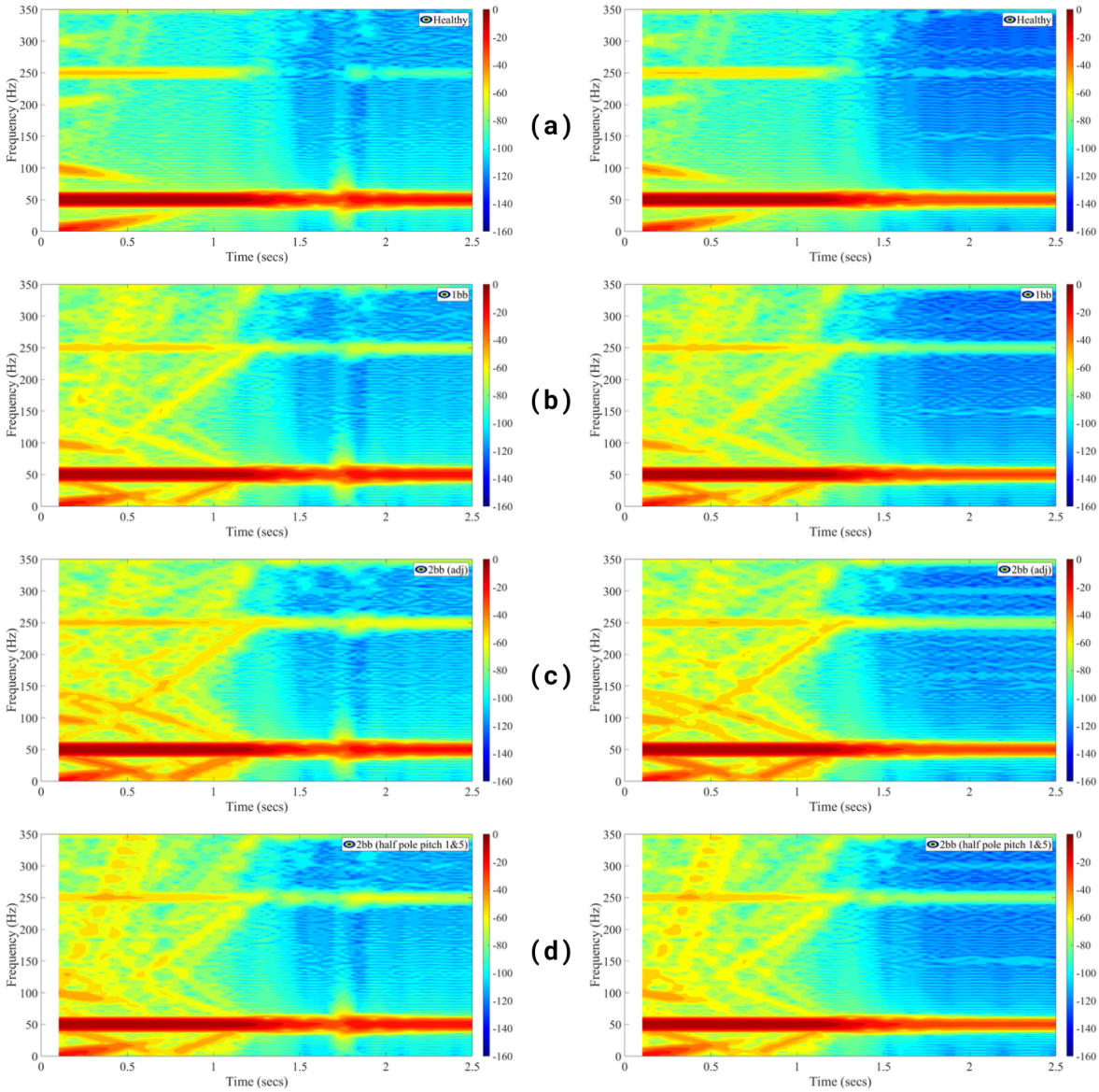

FIGURE 7.15: STFT current spectrogram comparisons of half-load (left) and no-load (right) operation under: a) Healthy operation, b) 1 broken bar fault, c) 2 adjacent broken bars fault, d) 2 non-adjacent broken bars with half pole pitch

7.5 Torque Analysis

7.5.1 Steady State

Analyzing the torque (Figures 7.16 to 7.18), the most significant results were observed under nominal load conditions, where the $2ksf_s$ harmonics were more prominent in faulty scenarios compared to the healthy motor. The amplitudes of the first three strongest signatures observed, are shown in Table 7.5. However, their amplitudes did not exceed the empirical threshold, indicating a weak fault signal. Under lower load conditions, these fault signatures were not present, making it difficult to draw definitive conclusions from the torque analysis in those cases.

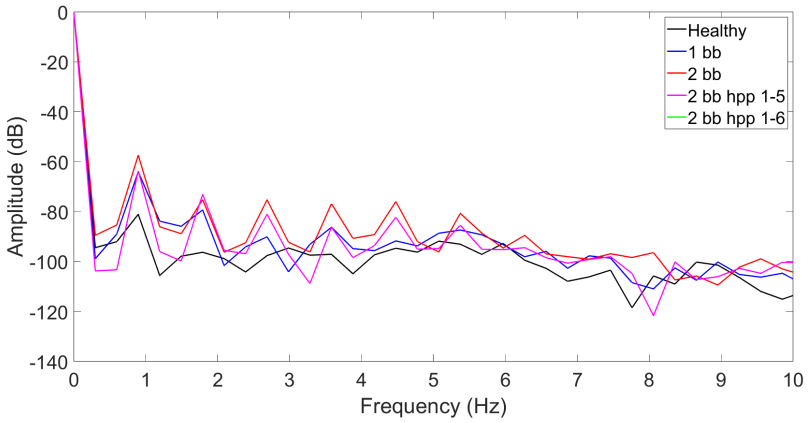

FIGURE 7.16: Torque analysis using FFT in the steady state under healthy and faulty conditions (11 kNm)

Simulated Cases	$4sf_s$	$8sf_s$	$12sfs$
Healthy	-81.07 dB	-96.28 dB	-97.62 dB
1 broken bar	-64.04 dB	-79.33 dB	-90.08 dB
2 broken bars (adj)	**-57.38 dB**	-75.18 dB	**-75.26 dB**
2 broken bars (1-5)	-63.67 dB	**-73.09 dB**	-81.04 dB
2 broken bars (1-6)	-63.66 dB	**-73.1 dB**	-81.04 dB

TABLE 7.5: $2ksf_s$ Amplitudes of Torque Analysis

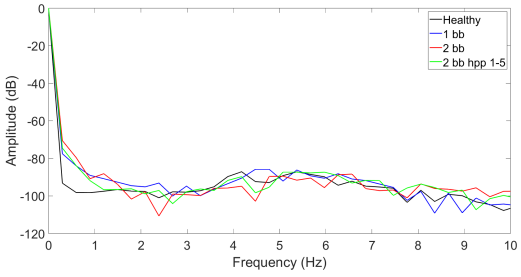

FIGURE 7.17: Torque analysis using FFT in the steady state(5.5 kNm)

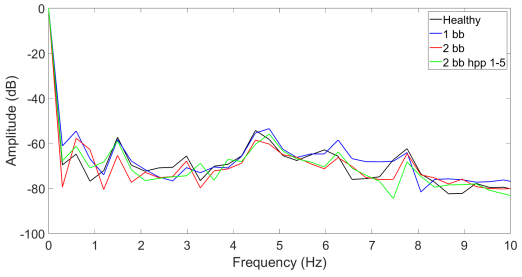

FIGURE 7.18: Torque analysis using FFT in the steady state (100 Nm)

7.5.2 Torque Analysis during Transients

When analyzing the torque's transient, it becomes evident that there is a DC component of the signal at 0 Hz, as well as a 300 Hz harmonic. This 300 Hz harmonic arises from the interaction between the rotor's fundamental harmonic and the 5th stator harmonic (6th order = 250 Hz + 50 Hz = 300 Hz), and is consistently present regardless of rotor health or faults. To be more precise, the triplet of this torque fundamental frequency (900 Hz) is noticeable in all cases, but the 300 Hz harmonic shows distinct behavior depending on the motor's condition. In healthy motor operations, the 300 Hz frequency is less pronounced and fades into the background becoming almost invisible. However, as the severity of the rotor fault increases, this harmonic becomes more prominent.

The spectrograms in Figures 7.19 through 7.23 clearly illustrate this trend. In the healthy motor (Figure 7.19), the 300 Hz harmonic is faint, but as faults are introduced—whether it's a single broken bar (Figure 7.20) or more severe cases like two adjacent broken bars (Figure 7.21)—the intensity of the 300 Hz harmonic increases. This pattern continues with non-adjacent broken bars, where the harmonic becomes even more significant as the fault worsens, as shown in Figures 7.22 and 7.23.

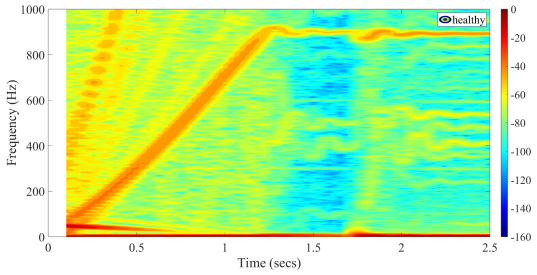

FIGURE 7.19: STFT torque spectrogram of studied motor under healthy condition.

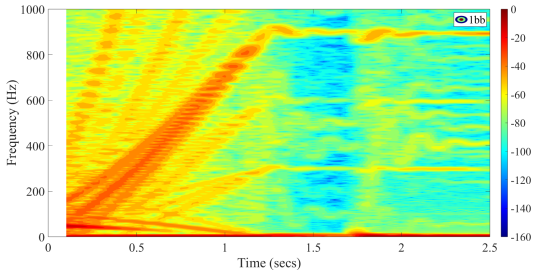

FIGURE 7.20: STFT torque spectrogram of studied motor with 1 broken bar.

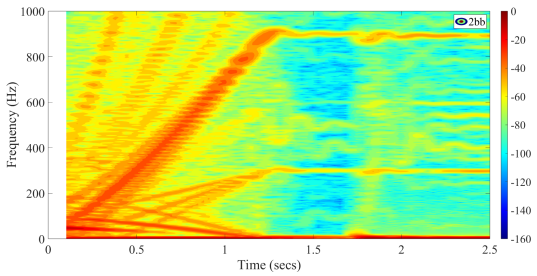

FIGURE 7.21: STFT torque spectrogram of motor with 2 adjacent broken bars.

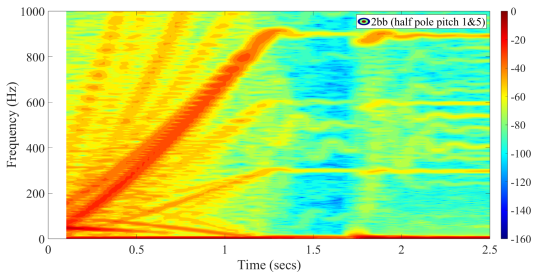

FIGURE 7.22: STFT torque spectrogram of motor with 2 broken bars (1-5).

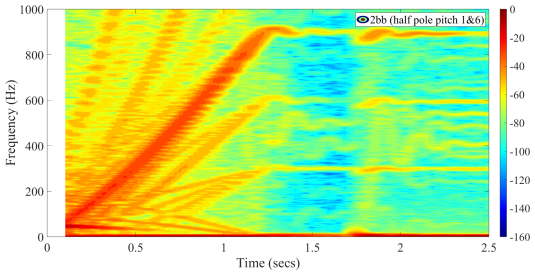

FIGURE 7.23: STFT torque spectrogram of motor with 2 broken bars (1-6).

Load Impact

As previously discussed in the previous section analysing the current transient, the load does not affect the start-up transient. This can be seen in Figure 7.24.

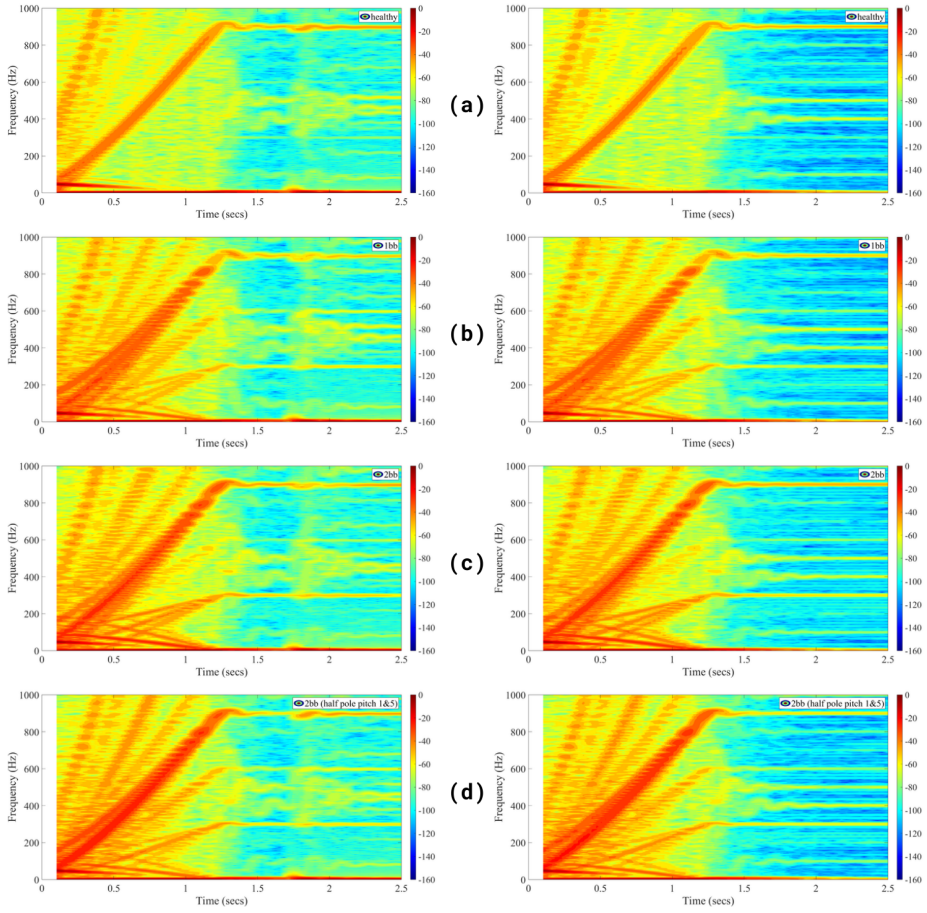

FIGURE 7.24: STFT torque spectrogram comparisons of half-load (left) and no-load (right) operation under: a) Healthy operation, b) 1 broken bar fault, c) 2 adjacent broken bars fault, d) 2 non-adjacent broken bars with half pole pitch

7.6 SFSA

As discussed in Chapter 4, the stray flux exhibits the same characteristic signatures as the current during steady-state operation but also provides additional signatures that are directly related to the rotor's mechanical speed. After processing the induced voltage data from one sensor and applying FFT, the resulting spectrum revealed that the most prominent signatures were those described by equation 4.10, which are specifically linked to the mechanical speed of the rotor. This is illustrated in the nominal load operation in Figure 7.25 and the amplitudes are shown in Table 7.6.

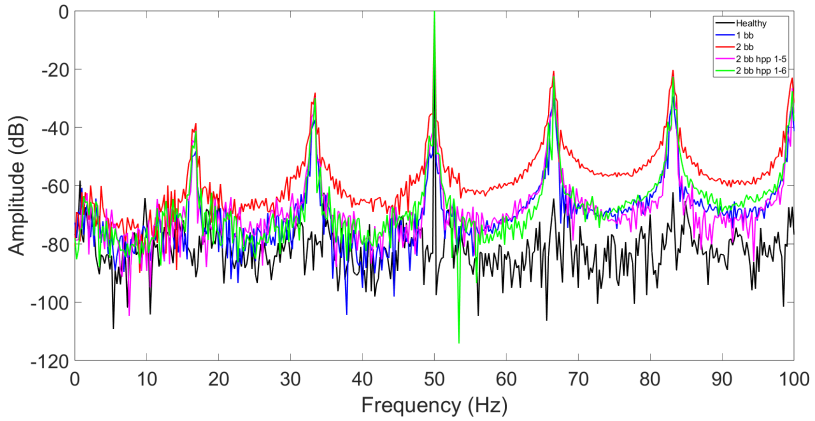

FIGURE 7.25: SFSA under healthy and faulty conditions (11 kNm)

Simulated Cases	$\left[1-2\frac{1-s}{p}\right] f_s$	$\left[1-\frac{1-s}{p}\right] f_s$	$\left[1+\frac{1-s}{p}\right] f_s$	$\left[1+2\frac{1-s}{p}\right] f_s$
Healthy	-91.45 dB	-76.77 dB	-64.49 dB	-62.35 dB
1 broken bar	-48.2 dB	-37.33 dB	-29.86 dB	-29.43 dB
2 broken bars (adj)	**-38.57 dB**	**-28.1 dB**	**-20.63 dB**	**-20.24 dB**
2 broken bars (1-5)	-41.1 dB	-29.76 dB	-22.27 dB	-22.4 dB
2 broken bars (1-6)	-41.31 dB	-29.94 dB	-22.47 dB	-22.66 dB

TABLE 7.6: $\left[n \pm m\frac{1-s}{p}\right] f_s$ Amplitudes of SFSA

In this analysis, the largest harmonic amplitude of the stray flux signature is observed under the condition of two adjacent broken bars, as shown in Table 7.6. Additionally, while the condition of two non-adjacent broken bars also presents a high harmonic amplitude, it remains slightly lower than that of the adjacent broken bar fault, yet still notably high. This indicates that while both fault types significantly impact the harmonic signature, the adjacent broken bars produce the most pronounced effect.

Under half-load (Figure 7.26) and no-load conditions (Figure 7.27), the speed-related harmonics remain present, but as the load decreases, the amplitude of these signals also decreases. Interestingly, in the no-load condition, the healthy motor exhibits greater amplitudes in the

mechanical speed-related harmonics compared to the faulty conditions, highlighting a potential challenge in distinguishing faults under no-load scenarios.

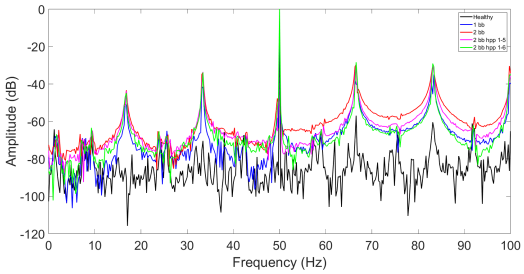

FIGURE 7.26: SFSA under healthy and faulty conditions (5.5 kNm)

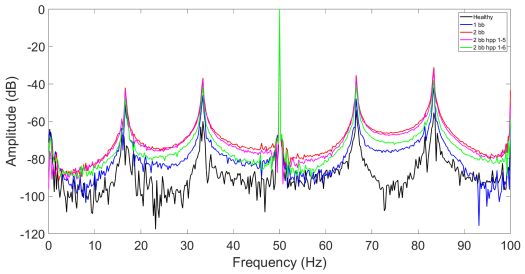

FIGURE 7.27: SFSA under healthy and faulty conditions (100 Nm)

7.6.1 Stray Flux Analysis during Transients

In the analysis of the stray flux transient, mechanical speed-related harmonics are clearly present, with their trajectories visible in the spectrograms. This is one of the key distinctions between the stray flux and current spectrograms. A significant difference between the two is the presence of the 3rd harmonic in the stray flux spectrogram, which is absent in the current spectrogram due to the motor's star-with-neutral connection. As shown in Figures 7.28 to 7.32, there is no marked distinction between the faulty and healthy conditions, making it challenging to differentiate between them based on these particular spectrograms alone.

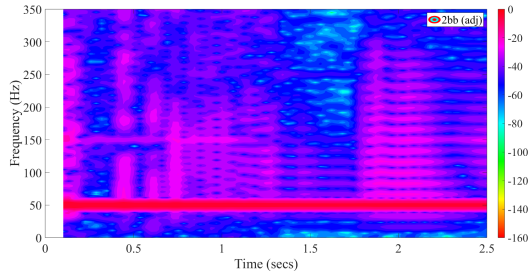

FIGURE 7.28: STFT flux spectrogram of IM under healthy condition.

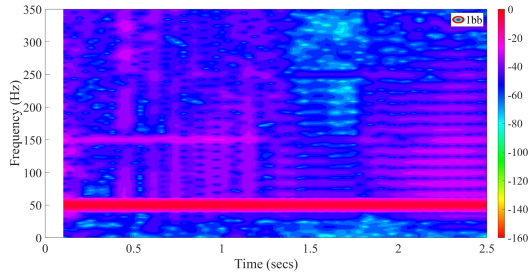

FIGURE 7.29: STFT flux spectrogram of IM with 1 broken bar.

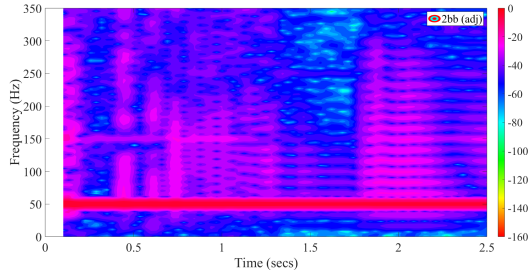

FIGURE 7.30: STFT flux spectrogram of IM with 2 adjacent broken bars.

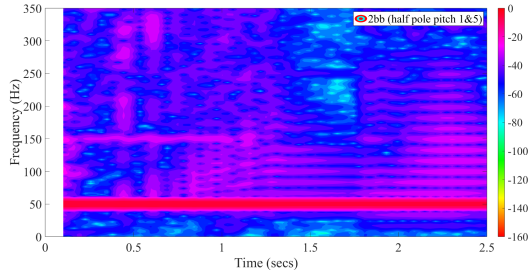

FIGURE 7.31: STFT flux spectrogram of IM with 2 non-adjacent broken bars (1-5).

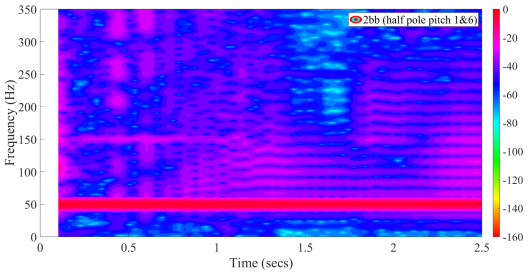

FIGURE 7.32: STFT flux spectrogram of IM with 2 non-adjacent broken bars (1-6).

Load Impact

As expected and shown in Figure 7.33, the load impact on the flux spectrogram is minimal.

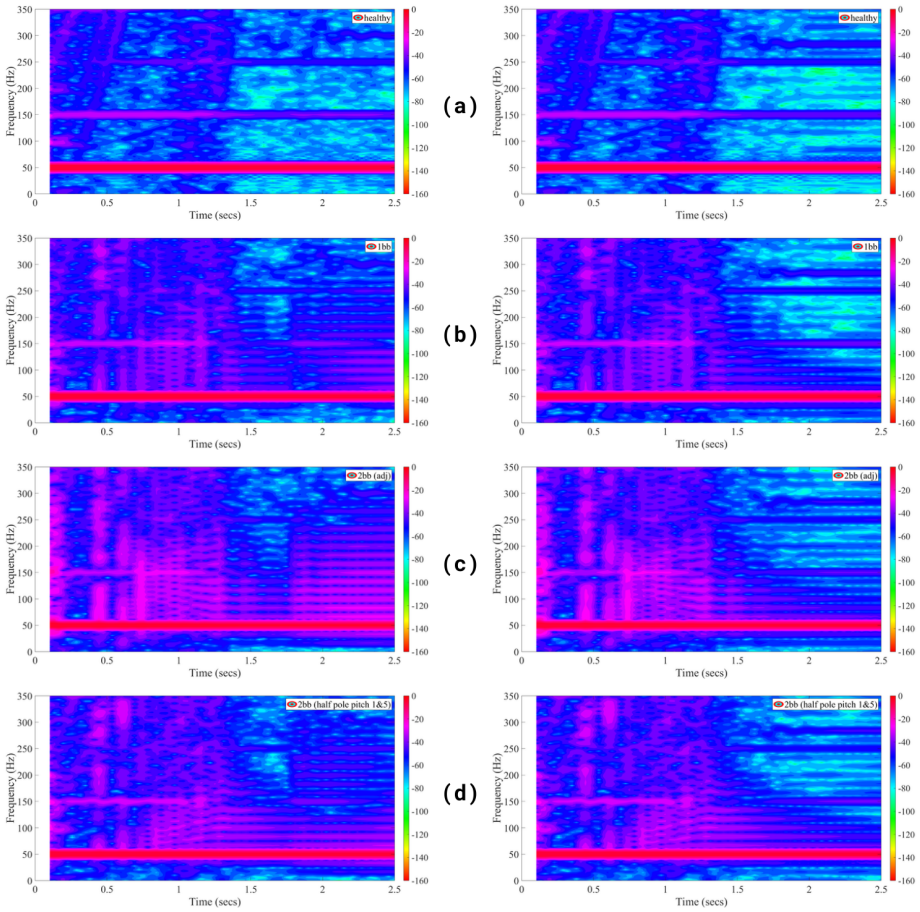

FIGURE 7.33: STFT flux spectrogram comparisons of half-load (left) and no-load (right) operation under: a) Healthy operation, b) 1 broken bar fault, c) 2 adjacent broken bars fault, d) 2 non-adjacent broken bars with half pole pitch

7.7 Zero-Sequence Flux Analysis

The ZSF fundamental frequency, located at $3f_s$, demonstrates a clear advantage over traditional MCSA, and this same superiority extends when comparing ZSF to SFSA. The ZSF is derived from signals captured by three radial stray flux sensors, each with 1000 turns and a diameter of 110 mm, positioned 120 electrical degrees apart. The spectral analysis between 50 Hz and 190 Hz for the induction motor (IM) during nominal operation is presented in Figure 7.34, while the frequency area of the ZSF fundamental is shown in Figure 7.35. The fault-related signature amplitudes around the fundamental frequency are summarized in Table 7.7.

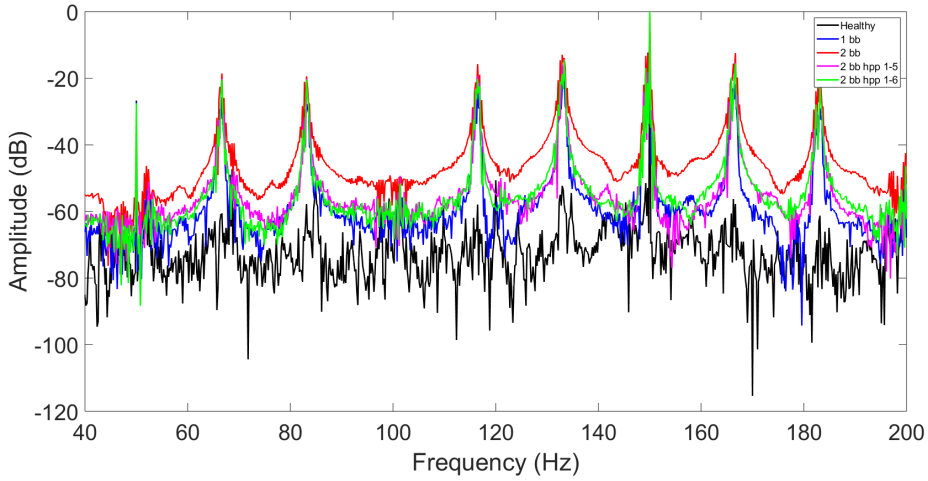

FIGURE 7.34: ZSF spectra of studied IM while at steady state under nominal load

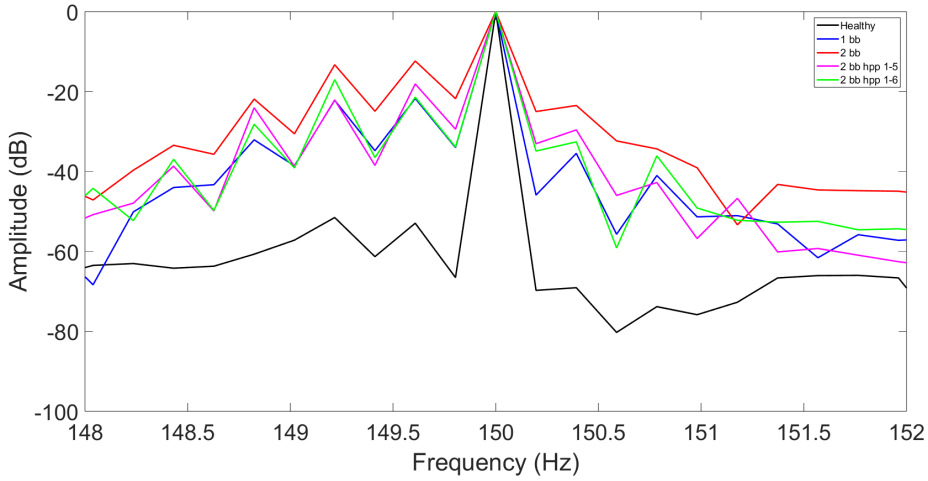

FIGURE 7.35: ZSF results of studied IM while at steady state under nominal load

Simulated Cases	$3f_s - 2sf_s$	$3f_s - 4sf_s$
Healthy	-52.94 dB	-51.52 dB
1 broken bar	-21.74 dB	-22.09 dB
2 broken bars (adj)	**-12.36 dB**	**-13.3 dB**
2 broken bars (1-5)	-18.11 dB	-22.09 dB
2 broken bars (1-6)	-21.41 dB	-17.03 dB

TABLE 7.7: $f_s \pm k\frac{1-s}{p}f_s$ Amplitudes of ZSF

From these results, several key conclusions can be drawn:

- The absolute amplitudes of the fault signatures are significantly higher than those in the stator current, as expected, reinforcing the diagnostic sensitivity of ZSF analysis.
- The increase in amplitude of the fault-related signatures is more pronounced compared to those found in stator current analysis, highlighting the superiority of ZSF in detecting rotor faults.
- Fault signatures close to the fundamental frequency are clearly visible in all faulty cases. Among these, the $3f_s - 4sf_s$ harmonic shows better sensitivity to fault severity. In contrast, the $3f_s - 2sf_s$ signature at can present lower amplitudes, sometimes even weaker than that of a single broken bar, but it remains distinguishable despite lacking monotonicity in amplitude growth.
- The harmonic $f_s \pm k\frac{1-s}{p}f_s$ increases by more than 40 dB when a fault occurs, regardless of the specific fault condition. These harmonics are further accompanied by fault-related sidebands spaced by $2ksf_s$, reinforcing the reliability of these signatures for fault detection.

When analyzing lower load conditions, such as half-load (Figure 7.36), only the $3f_s - 4sf_s$ harmonic remains visible. This is due to the reduced slip, which causes the $3f_s - 2sf_s$ signature to merge with the fundamental harmonic, rendering it indistinguishable. The resulting amplitudes around $3f_s$for the half-load scenario are detailed in Table 7.8. In the no-load condition (Figure 7.8), both signature harmonics are absorbed by the fundamental frequency, leaving no discernible fault-related information. Consequently, no valuable diagnostic insights could be obtained from the no-load analysis, highlighting the limitations of fault detection at extremely low or no-load conditions.

Simulated Cases	$3f_s - 4sf_s$
Healthy	-52.18 dB
1 broken bar	-27.63 dB
2 broken bars (adj)	**-19.75 dB**
2 broken bars (1-5)	-28.85 dB
2 broken bars (1-6)	-22.79 dB

TABLE 7.8: $f_s \pm k\frac{1-s}{p} f_s$ Amplitudes of ZSF under half-load

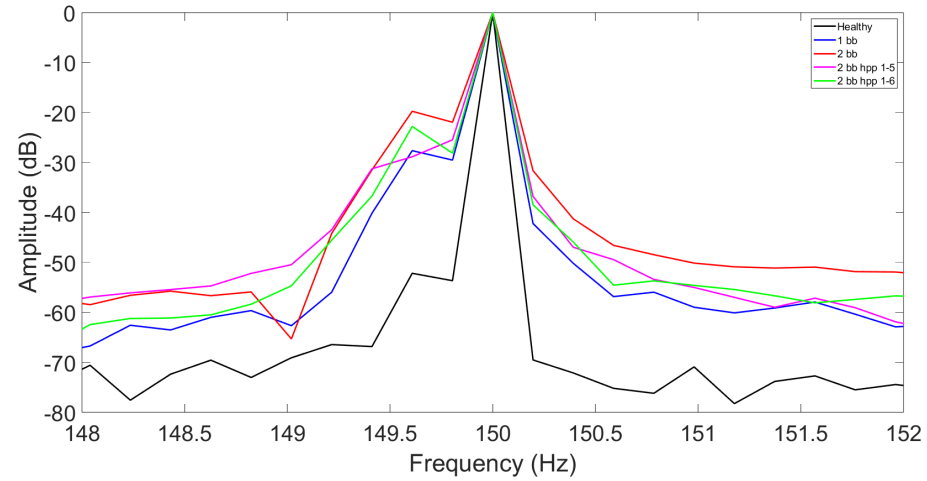

FIGURE 7.36: ZSF results of studied IM while at steady state under half-load

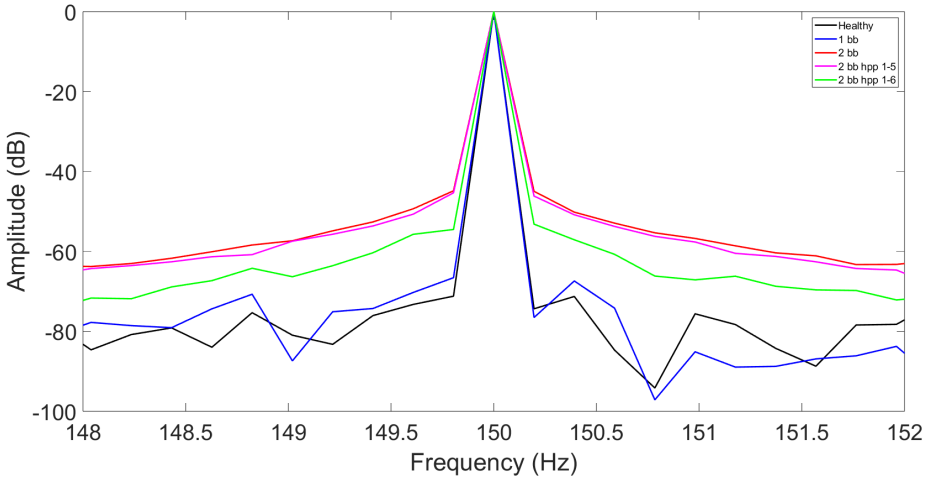

FIGURE 7.37: ZSF results of studied IM while at steady state under no load

7.7.1 ZSF Analysis during Transients

Although the primary aim of this study is to develop a method for steady-state analysis, it is crucial that the method also demonstrates fault sensitivity during the motor's start-up transient. To address this, the ZSF was evaluated under transient conditions as well.

The expected fault trajectories are illustrated in Figure 7.38, highlighting the emergence of broken bar fault side-bands around both the mechanical frequency-induced harmonics and those generated by the stator MMF.

The spectrograms for the analyzed cases are shown in Figures 7.39 to 7.43. The simulation results align well with the predicted trajectories, confirming the method's effectiveness in capturing fault signatures during transient conditions.

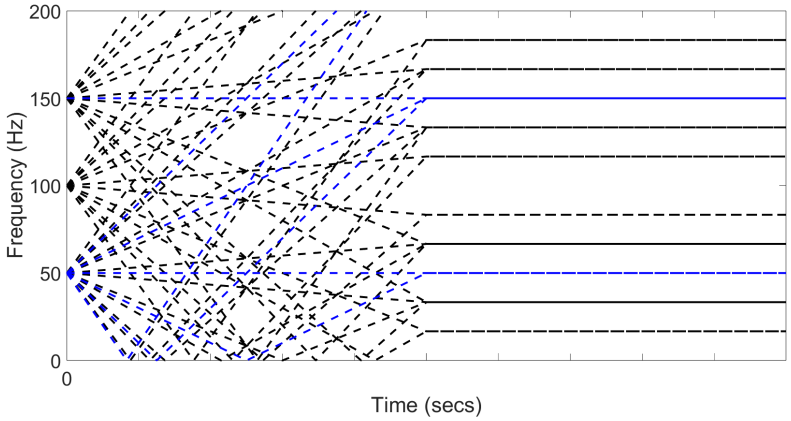

FIGURE 7.38: Expected broken bar fault harmonic trajectories in the ZSF of a 6-pole IM

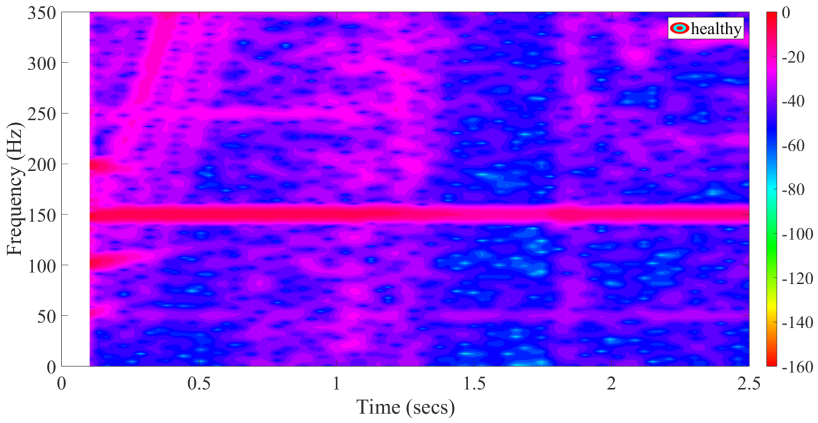

FIGURE 7.39: STFT spectrogram of the ZSF of IM under nominal load and healthy condition

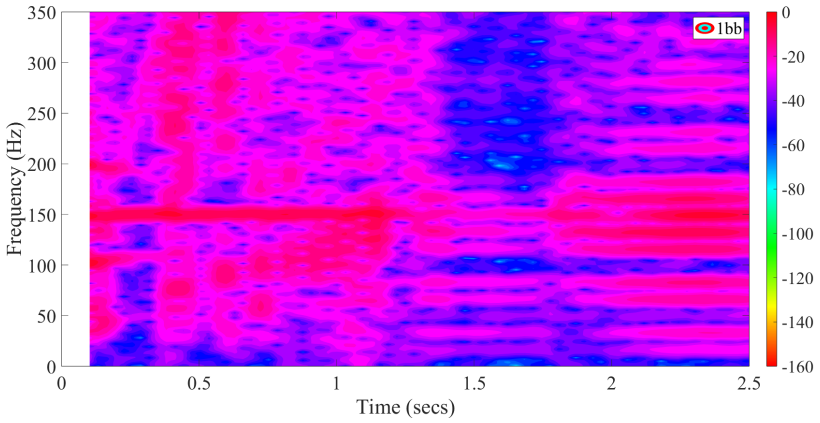

FIGURE 7.40: STFT spectrogram of the ZSF of IM under nominal load and 1 broken bar

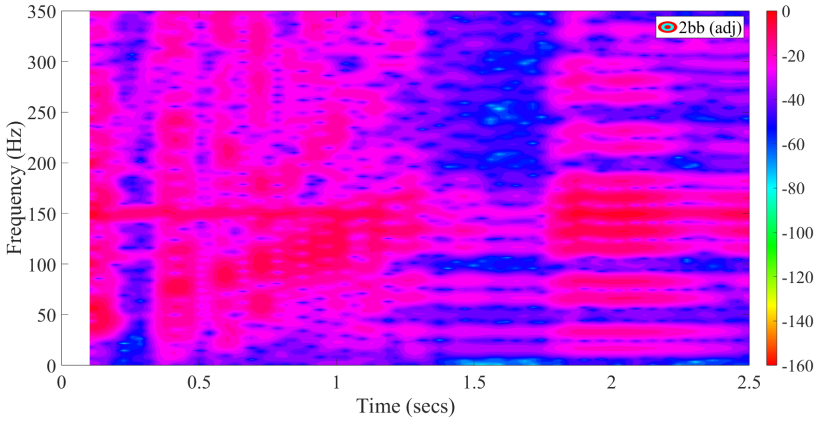

FIGURE 7.41: STFT spectrogram of the ZSF of IM under nominal load and 2 adjacent broken bars

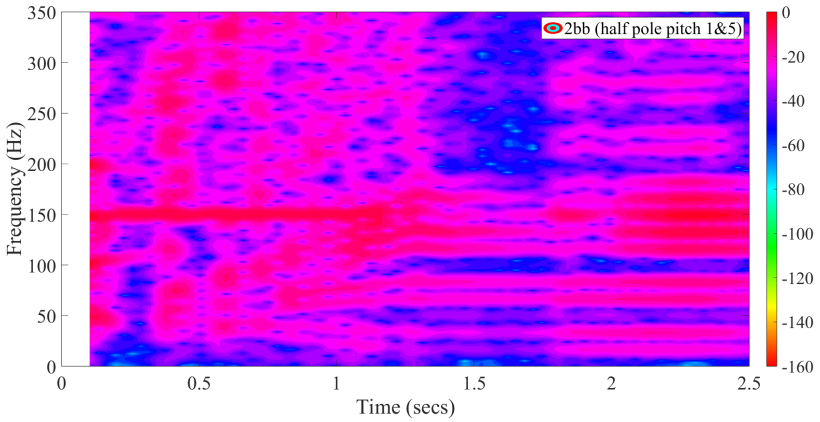

FIGURE 7.42: STFT spectrogram of the ZSF of IM under nominal load and 2 non-adjacent broken bars (1-5)

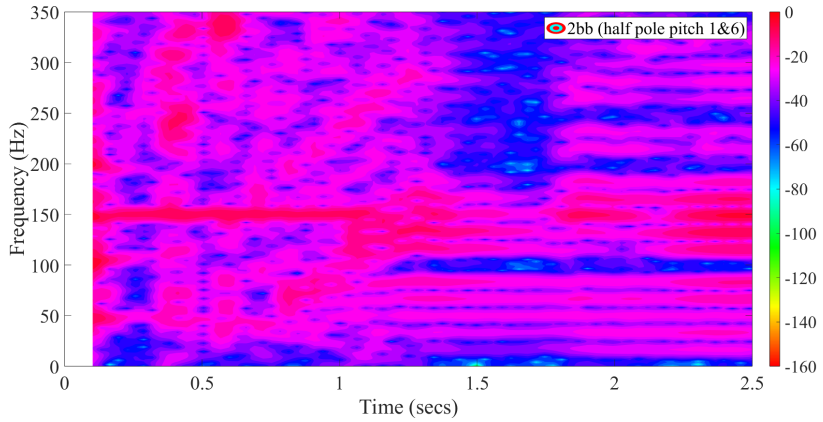

FIGURE 7.43: STFT spectrogram of the ZSF of IM under nominal load and 2 non-adjacent broken bars (1-6)

Load Impact

The spectrograms of the half load and no-load cases are shown below in Figure 7.44:

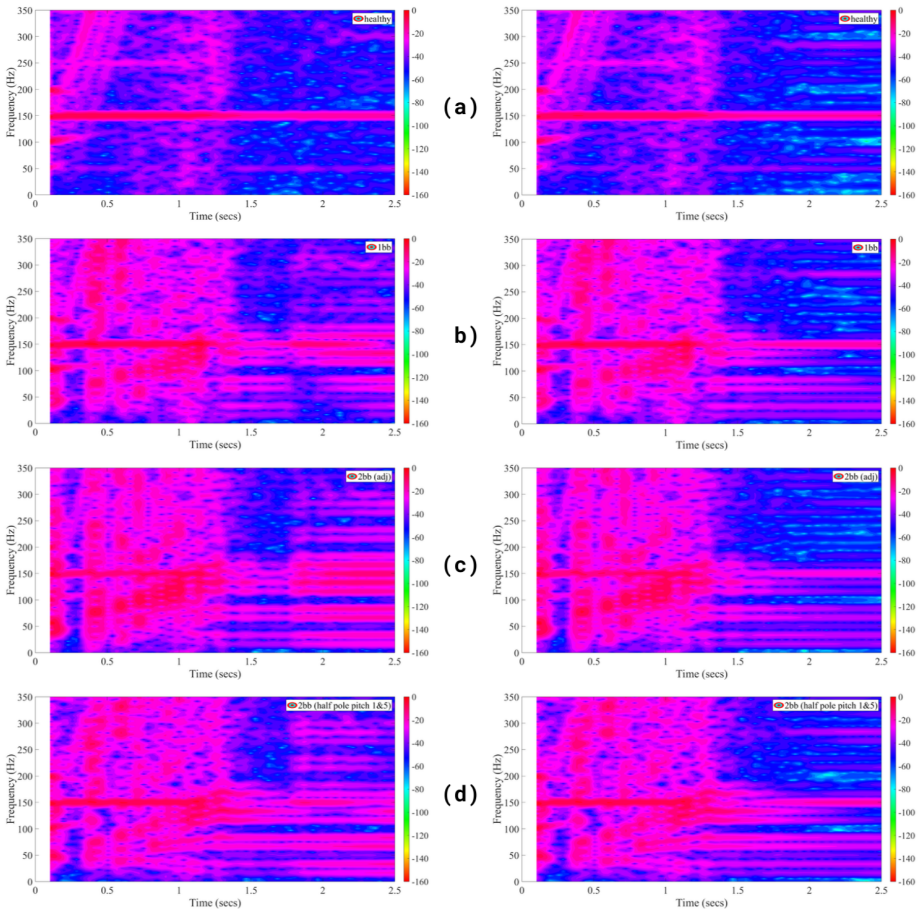

FIGURE 7.44: STFT spectrograms of the ZSF comparing the half-load (left) and no-load (right) operation under: a) Healthy operation, b) 1 broken bar fault, c) 2 adjacent broken bars fault, d) 2 non-adjacent broken bars with half pole pitch

Chapter 8

Conclusions and Future Work

8.1 Conclusions

This thesis presents the Zero-Sequence Flux (ZSF) as a robust diagnostic tool for detecting rotor faults, specifically addressing the challenge of identifying non-adjacent broken rotor bars without generating false negative alarms. The results of this study demonstrate the superiority of ZSF over traditional stator current analysis, both in steady-state and transient conditions. Compared to other diagnostic methods, such as torque analysis and stray flux signature analysis, the ZSF offers a distinct advantage due to its rich spectrum of fault-induced harmonics. The presence of mechanical frequency harmonics associated with broken bar faults, coupled with the enhanced amplitude of the ZSF fundamental frequency, underscores the effectiveness of this method in providing a comprehensive fault detection mechanism. These findings establish the ZSF as a reliable and sensitive diagnostic signal, offering significant improvements in rotor fault detection capabilities.

8.2 Future Work

Building on the foundation laid by this thesis, future research will aim to experimentally validate the proposed ZSF method and investigate the influence of inherent rotor asymmetries on fault diagnosis. Experimental studies will be conducted to assess the practical applicability of the ZSF method in real-world conditions. Additionally, the development and simulation of 3D motor models with higher sampling frequencies will be pursued to further refine and validate the diagnostic approach. These models will enable a more detailed analysis of the electromagnetic field distribution and its impact on fault signatures. Exploring advanced signal processing techniques and machine learning algorithms to enhance the detection and classification of fault conditions is also a promising direction for future work. By expanding the scope of this research, the aim is to solidify the ZSF method as a reliable, versatile, and comprehensive tool for rotor fault diagnostics in industrial applications.

References

[1] Pinjia Zhang et al. "A Survey of Condition Monitoring and Protection Methods for Medium-Voltage Induction Motors". In: *IEEE Transactions on Industry Applications* 47.1 (Jan. 2011), pp. 34–46. ISSN: 1939-9367. DOI: 10.1109/TIA.2010.2090839. URL: https://ieeexplore.ieee.org/document/5620974 (visited on 08/07/2024).

[2] O.V. Thorsen and M. Dalva. "Failure Identification and Analysis for High-Voltage Induction Motors in the Petrochemical Industry". In: *IEEE Transactions on Industry Applications* 35.4 (July 1999), pp. 810–818. ISSN: 1939-9367. DOI: 10.1109/28.777188. URL: https://ieeexplore.ieee.org/document/777188 (visited on 09/25/2024).

[3] Dionysios V. Spyropoulos et al. "The Influence of the Broken Bar Fault on the Magnetic Field and Electromagnetic Torque in 3-Phase Induction Motors". In: *2012 XXth International Conference on Electrical Machines*. 2012 XXth International Conference on Electrical Machines. Sept. 2012, pp. 1868–1874. DOI: 10.1109/ICElMach.2012.6350136. URL: https://ieeexplore.ieee.org/document/6350136 (visited on 09/25/2024).

[4] Konstantinos N. Gyftakis et al. "A Novel Approach for Broken Bar Fault Diagnosis in Induction Motors Through Torque Monitoring". In: *IEEE Transactions on Energy Conversion* 28.2 (June 2013), pp. 267–277. ISSN: 1558-0059. DOI: 10.1109/TEC.2013.2240683. URL: https://ieeexplore.ieee.org/document/6458995 (visited on 09/25/2024).

[5] Maëva Garcia and José Antonino-Daviu. "Efficiency Assessment of Induction Motors Operating under Different Fault Conditions". In: *2018 IEEE International Conference on Industrial Technology (ICIT)*. 2018 IEEE International Conference on Industrial Technology (ICIT). Feb. 2018, pp. 1837–1842. DOI: 10.1109/ICIT.2018.8352464. URL: https://ieeexplore.ieee.org/document/8352464 (visited on 09/25/2024).

[6] Gang Niu, Xun Dong, and Yuejian Chen. "Motor Fault Diagnostics Based on Current Signatures: A Review". In: *IEEE Transactions on Instrumentation and Measurement* 72 (2023), pp. 1–19. ISSN: 0018-9456, 1557-9662. DOI: 10.1109/TIM.2023.3285999. URL: https://ieeexplore.ieee.org/document/10151958/ (visited on 09/03/2024).

[7] Gennadi Y. Sizov et al. "Analysis and Diagnostics of Adjacent and Nonadjacent Broken-Rotor-Bar Faults in Squirrel-Cage Induction Machines". In: *IEEE Transactions on Industrial Electronics* 56.11 (Nov. 2009), pp. 4627–4641. ISSN: 1557-9948. DOI: 10.1109/TIE.2008.2011341. URL: https://ieeexplore.ieee.org/document/4738347 (visited on 09/25/2024).

[8] Emiliano Sisinni et al. “Industrial Internet of Things: Challenges, Opportunities, and Directions”. In: *IEEE Transactions on Industrial Informatics* 14.11 (Nov. 2018), pp. 4724–4734. ISSN: 1551-3203, 1941-0050. DOI: 10.1109/TII.2018.2852491. URL: https://ieeexplore.ieee.org/document/8401919/ (visited on 09/03/2024).

[9] Mohammad Rezazadeh Mehrjou et al. “Rotor Fault Condition Monitoring Techniques for Squirrel-Cage Induction Machine—A Review”. In: *Mechanical Systems and Signal Processing* 25.8 (Nov. 1, 2011), pp. 2827–2848. ISSN: 0888-3270. DOI: 10.1016/j.ymssp.2011.05.007. URL: https://www.sciencedirect.com/science/article/pii/S0888327011002032 (visited on 09/25/2024).

[10] Konstantinos N. Gyftakis and Joya C. Kappatou. “Evaluation of the Broken Bar Fault Detectability Depending on the Rotor Bar Number”. In: *IECON 2013 - 39th Annual Conference of the IEEE Industrial Electronics Society*. IECON 2013 - 39th Annual Conference of the IEEE Industrial Electronics Society. Nov. 2013, pp. 2798–2803. DOI: 10.1109/IECON.2013.6699574. URL: https://ieeexplore.ieee.org/document/6699574 (visited on 09/25/2024).

[11] Renato Yabiku et al. “A Comparative Study between Copper and Aluminum Induction Squirrel Cage Constructions”. In: *2010 Record of Conference Papers Industry Applications Society 57th Annual Petroleum and Chemical Industry Conference (PCIC)*. 2010 Record of Conference Papers Industry Applications Society 57th Annual Petroleum and Chemical Industry Conference (PCIC). Sept. 2010, pp. 1–9. DOI: 10.1109/PCIC.2010.5666832. URL: https://ieeexplore.ieee.org/document/5666832 (visited on 09/25/2024).

[12] M. Riera-Guasp et al. “Influence of Nonconsecutive Bar Breakages in Motor Current Signature Analysis for the Diagnosis of Rotor Faults in Induction Motors”. In: *IEEE Transactions on Energy Conversion* 25.1 (Mar. 2010), pp. 80–89. ISSN: 0885-8969. DOI: 10.1109/TEC.2009.2032622. URL: http://ieeexplore.ieee.org/document/5350691/ (visited on 08/08/2024).

[13] Kenneth Edomwandekhoe and Xiaodong Liang. “Advanced Feature Selection for Broken Rotor Bar Faults in Induction Motors”. In: *2018 IEEE/IAS 54th Industrial and Commercial Power Systems Technical Conference (I&CPS)*. 2018 IEEE/IAS 54th Industrial and Commercial Power Systems Technical Conference (I&CPS). May 2018, pp. 1–10. DOI: 10.1109/ICPS.2018.8369981. URL: https://ieeexplore.ieee.org/document/8369981 (visited on 08/08/2024).

[14] Muhammad Irfan et al. “An Assessment on the Non-Invasive Methods for Condition Monitoring of Induction Motors”. In: *Fault Diagnosis and Detection*. IntechOpen, May 31, 2017. ISBN: 978-953-51-3204-2. DOI: 10.5772/67917. URL: https://www.intechopen.com/chapters/54865 (visited on 08/08/2024).

[15] Gholam Reza Agah et al. “Broken Rotor Bar and Rotor Eccentricity Fault Detection in Induction Motors Using a Combination of Discrete Wavelet Transform and Teager–Kaiser

Energy Operator". In: *IEEE Transactions on Energy Conversion* 37.3 (2022), pp. 2199–2206. URL: https://ieeexplore.ieee.org/abstract/document/9743320/ (visited on 09/25/2024).

[16] Jesus Joaquin Yanez-Borjas et al. "Experimental Validation of the Broken Rotor Bar Fault Evolution in Line-Fed Induction Motors". In: *2018 IEEE International Autumn Meeting on Power, Electronics and Computing (ROPEC)*. IEEE, 2018, pp. 1–7. URL: https://ieeexplore.ieee.org/abstract/document/8661426/?casa_token=L4xIlHTChWQAAAAA:v0_rtPvrZU2tNh9631E (visited on 09/25/2024).

[17] Vanessa Fernandez-Cavero et al. "Detection of Broken Rotor Bars in Nonlinear Startups of Inverter-Fed Induction Motors". In: *IEEE Transactions on Industry Applications* 57.3 (2021), pp. 2559–2568. URL: https://ieeexplore.ieee.org/abstract/document/9380705/ (visited on 09/25/2024).

[18] Dionysios V. Spyropoulos et al. "Extraction of Frequency Information for the Reliable Screening of Rotor Electrical Faults Via Torque Monitoring in Induction Motors". In: *IEEE Transactions on Industry Applications* 57.6 (Nov. 2021), pp. 5949–5958. ISSN: 1939-9367. DOI: 10.1109/TIA.2021.3112137. URL: https://ieeexplore.ieee.org/abstract/document/9536403 (visited on 09/25/2024).

[19] Chunhua Liu. "Emerging Electric Machines and Drives — An Overview". In: *IEEE Transactions on Energy Conversion* 33.4 (Dec. 2018), pp. 2270–2280. ISSN: 1558-0059. DOI: 10.1109/TEC.2018.2852732. URL: https://ieeexplore.ieee.org/document/8402098 (visited on 09/25/2024).

[20] S. Chapman. "Electric Machinery Fundamentals". In: 1991. URL: https://www.semanticscholar.org/paper/Electric-Machinery-Fundamentals-Chapman/d203373cbd7cce570f25c69f96f5bf77 (visited on 01/15/2024).

[21] G. Ferraris. "Atti Della Reale Academia Delle Science Di Torino". In: *Atti della R. Academia delle Science di Torino. XXIII: 360* 375 (1888).

[22] EEP-Electrical Engineering Portal and Edvard Csanyi. *Induction Machines - Historical Touch*. EEP - Electrical Engineering Portal. Mar. 15, 2011. URL: https://electrical-engineering-portal.com/induction-machines-historical-touch (visited on 09/30/2024).

[23] Matteo Carbonieri, Nicola Bianchi, and Luigi Alberti. "Induction Motor Analysis Using Magnetostatic Finite Element Simulations Considering Skewing". In: *2019 IEEE International Electric Machines & Drives Conference (IEMDC)*. IEEE, 2019, pp. 147–153. URL: https://ieeexplore.ieee.org/abstract/document/8785381/?casa_token=feBzTIRjYvYAAAAA:fyb4_06tS70FLrL8RpydUja-D-5JoNQt1ANhSUYiQvDL5g0e3ZOUhNMbGvnpVwqQMsNBqcYizw (visited on 09/25/2024).

[24] Alamy Limited. *Rotor and Stator of Electric Motor Isolated on White Background. 3d Illustration Stock Photo - Alamy*. URL: https://www.alamy.com/rotor-and-stator-of-electric-motor-isolated-on-white-background-3d-illustration-image438795885.html (visited on 09/30/2024).

[25] Austin H. Bonnett and George C. Soukup. "Rotor Failures in Squirrel Cage Induction Motors". In: *IEEE transactions on industry applications* 6 (1986), pp. 1165–1173. URL: https://ieeexplore.ieee.org/abstract/document/4504850/ (visited on 09/25/2024).

[26] Alamy Limited. *Squirrel Cage Rotor Exploded View 3D Rendering Isolated on White Background Stock Photo - Alamy*. URL: https://www.alamy.com/squirrel-cage-rotor-exploded-view-3d-rendering-isolated-on-white-background-image470552745.html (visited on 09/30/2024).

[27] Anibal T. De Almeida, Fernando JTETE Ferreira, and Joao AC Fong. "Standards for Efficiency of Electric Motors". In: *IEEE Industry Applications Magazine* 17.1 (2010), pp. 12–19. URL: https://ieeexplore.ieee.org/abstract/document/5635306/ (visited on 09/25/2024).

[28] *Figure 3. Rotor Slot Shape Classification According to NEMA Standard*. ResearchGate. URL: https://www.researchgate.net/figure/Rotor-slot-shape-classification-according-to-NEMA-standard_fig3_366415208 (visited on 09/30/2024).

[29] Alamy Limited. *Rotor for Electric Motor, Assembled Sheets, 3d Illustration Isolated on White Background Stock Photo - Alamy*. URL: https://www.alamy.com/rotor-for-electric-motor-assembled-sheets-3d-illustration-isolated-on-white-background-image471568374.html (visited on 09/30/2024).

[30] Alamy Limited. *Stator for Electric Motor Stock Photo - Alamy*. URL: https://www.alamy.com/stator-for-electric-motor-image555050120.html (visited on 09/30/2024).

[31] *Stator Coil Manufacturer & Supplier*. Electric Motor Coil Company. URL: https://www.emccltd.ca/stator-coil-manufacturer/ (visited on 09/30/2024).

[32] *Cross-section of Slots in Form-wound Multi-turn Coils*. ResearchGate. URL: https://www.researchgate.net/figure/Cross-section-of-slots-in-form-wound-multi-turn-coils_fig4_336013183 (visited on 09/30/2024).

[33] *Induction vs DC Brushless*. Jan. 14, 2021. URL: https://www.atechtraining.com/induction-vs-dc-brushless (visited on 09/30/2024).

[34] Alamy Limited. *Rotor Copper Coil for Electric Motor Isolated on White Background 3D Rendering Stock Photo - Alamy*. URL: https://www.alamy.com/rotor-copper-coil-for-electric-motor-isolated-on-white-background-3d-rendering-image470552676.html (visited on 09/30/2024).

[35] net_va. *3 Phase Motor Parts : A Comprehensive Guide*. Aug. 20, 2022. URL: https://www.xinnuomotor.com/3-phase-motor-parts (visited on 09/30/2024).

[36] Κωνσταντίνος Γυφτάκης. "Ηλεκτρομαγνητική ανάλυση σφαλμάτων σε επαγωγικούς κινητήρες και ανάπτυξη νέων μεθόδων διάγνωσης αυτών". Oct. 2015. URL: http://hdl.handle.net/10889/9780 (visited on 09/06/2024).

[37] kamalkant. *Torque Slip Characteristics of Three Phase Induction Motor*. Mango Engineer. URL: https://www.mangoengineer.in/2024/03/Torque-Slip-Characteristics-of-Induction-Motor.html (visited on 09/30/2024).

[38] Electrical Technology. *What Is the Equivalent Circuit of Induction Motor?* ELECTRICAL TECHNOLOGY. Apr. 4, 2022. URL: https://www.electricaltechnology.org/2022/04/equivalent-circuit-induction-motor.html (visited on 09/30/2024).

[39] *Losses in a Motor - Power Stages in an Induction Motor*. URL: https://www.electricaltechnology.org/2022/07/power-stages-losses-induction-motor.html (visited on 09/30/2024).

[40] Rahman Saidur. "A Review on Electrical Motors Energy Use and Energy Savings". In: *Renewable and sustainable energy reviews* 14.3 (2010), pp. 877–898. URL: https://www.sciencedirect.com/science/article/pii/S1364032109002494?casa_token=tijHemVJ0BcAAAAA:xoVpFoosHprvP85N1nBSefS7--0EUKYBVCKuuzscqy3XsPIzF-7ueeKfe_J2WMmozMNIet3FCQ (visited on 09/25/2024).

[41] Anibal T. De Almeida, Fernando JTETE Ferreira, and Joao AC Fong. "Standards for Efficiency of Electric Motors". In: *IEEE Industry Applications Magazine* 17.1 (2010), pp. 12–19. URL: https://ieeexplore.ieee.org/abstract/document/5635306/ (visited on 09/25/2024).

[42] S. Nandi, H.A. Toliyat, and X. Li. "Condition Monitoring and Fault Diagnosis of Electrical Motors—A Review". In: *IEEE Transactions on Energy Conversion* 20.4 (Dec. 2005), pp. 719–729. ISSN: 0885-8969. DOI: 10.1109/TEC.2005.847955. URL: http://ieeexplore.ieee.org/document/1546063/ (visited on 09/03/2024).

[43] Jangho Yun and Sang Bin Lee. "Influence of Aluminum Die-Cast Rotor Porosity on the Efficiency of Induction Machines". In: *IEEE Transactions on Magnetics* 54.11 (Nov. 2018), pp. 1–5. ISSN: 0018-9464, 1941-0069. DOI: 10.1109/TMAG.2018.2841912. URL: https://ieeexplore.ieee.org/document/8388748/ (visited on 09/03/2024).

[44] *(5) Case Study: Rotor Porosity in New Motor Causes Motor Failure – Cast Aluminum | LinkedIn*. URL: https://www.linkedin.com/pulse/case-study-rotor-porosity-new-motor-causes-failure-cast-brian-james/ (visited on 09/30/2024).

[45] *Figure 1. Static Eccentricity of the Rotor.* ResearchGate. URL: https://www.researchgate.net/figure/Static-eccentricity-of-the-rotor_fig1_350599714 (visited on 09/30/2024).

[46] Greg C. Stone et al. "Electrical Insulation for Rotating Machines: Design, Evaluation, Aging, Testing, and Repair". In: Wiley, July 11, 2014. ISBN: 978-1-118-88666-3. DOI: 10.1002/9781118886663. URL: https://onlinelibrary.wiley.com/doi/book/10.1002/9781118886663 (visited on 09/03/2024).

[47] Fernando JTE Ferreira, Ge Baoming, and Aníbal T. de Almeida. "Reliability and Operation of High-Efficiency Induction Motors". In: *2015 IEEE/IAS 51st Industrial & Commercial Power Systems Technical Conference (I&CPS)*. IEEE, 2015, pp. 1–13. URL: https://ieeexplore.ieee.org/abstract/document/7266412/?casa_token=lvo_S6lXMJoAAAAA:

AiA5WOxXHpNp_RKpj-SJkmAlax2T0V2WFX8VeXaRqcIS_ZGJGb_hPEHptFQB84_hswBUqIC1yA (visited on 09/25/2024).

[48] Lucia Frosini and Ezio Bassi. "Stator Current and Motor Efficiency as Indicators for Different Types of Bearing Faults in Induction Motors". In: *IEEE Transactions on Industrial electronics* 57.1 (2009), pp. 244–251. URL: https://ieeexplore.ieee.org/abstract/document/5166499/ (visited on 09/25/2024).

[49] O.V. Thorsen and M. Dalva. "Failure Identification and Analysis for High-Voltage Induction Motors in the Petrochemical Industry". In: *IEEE Transactions on Industry Applications* 35.4 (July 1999), pp. 810–818. ISSN: 1939-9367. DOI: 10.1109/28.777188. URL: https://ieeexplore.ieee.org/document/777188 (visited on 09/09/2024).

[50] "Report of Large Motor Reliability Survey of Industrial and Commercial Installations, Part II". In: *IEEE Transactions on Industry Applications* IA-21.4 (July 1985), pp. 865–872. ISSN: 1939-9367. DOI: 10.1109/TIA.1985.349533. URL: https://ieeexplore.ieee.org/document/4158072 (visited on 09/09/2024).

[51] Martin Kaufhold et al. "Electrical Stress and Failure Mechanism of the Winding Insulation in PWM-inverter-fed Low-Voltage Induction Motors". In: *IEEE Transactions on industrial electronics* 47.2 (2000), pp. 396–402. URL: https://ieeexplore.ieee.org/abstract/document/836355/ (visited on 09/25/2024).

[52] Thomas W. Dakin. "Electrical Insulation Deterioration Treated as a Chemical Rate Phenomenon". In: *Transactions of the American Institute of Electrical Engineers* 67.1 (Jan. 1948), pp. 113–122. ISSN: 2330-9431. DOI: 10.1109/T-AIEE.1948.5059649. URL: https://ieeexplore.ieee.org/document/5059649 (visited on 09/04/2024).

[53] C. Sciascera et al. "Lifetime Consumption and Degradation Analysis of the Winding Insulation of Electrical Machines". In: *8th IET International Conference on Power Electronics, Machines and Drives (PEMD 2016)*. 8th IET International Conference on Power Electronics, Machines and Drives (PEMD 2016). Apr. 2016, pp. 1–5. DOI: 10.1049/cp.2016.0231. URL: https://ieeexplore.ieee.org/document/7739419 (visited on 09/04/2024).

[54] Voitto I. J. Kokko. "Ageing Due to Thermal Cycling by Start and Stop Cycles in Lifetime Estimation of Hydroelectric Generator Stator Windings". In: *2011 IEEE International Electric Machines & Drives Conference (IEMDC)*. 2011 IEEE International Electric Machines & Drives Conference (IEMDC). May 2011, pp. 318–323. DOI: 10.1109/IEMDC.2011.5994867. URL: https://ieeexplore.ieee.org/document/5994867 (visited on 09/04/2024).

[55] G.C. Montanari and L. Simoni. "Aging Phenomenology and Modeling". In: *IEEE Transactions on Electrical Insulation* 28.5 (1993), pp. 755–776. ISSN: 00189367. DOI: 10.1109/14.237740. URL: http://ieeexplore.ieee.org/document/237740/ (visited on 09/04/2024).

[56] *Different Types of Faults of Induction Motors. | Download Scientific Diagram*. URL: https://www.researchgate.net/figure/Different-types-of-faults-of-induction-motors_fig1_337926577 (visited on 09/30/2024).

[57] Renato Yabiku et al. "A Comparative Study between Copper and Aluminum Induction Squirrel Cage Constructions". In: *2010 Record of Conference Papers Industry Applications Society 57th Annual Petroleum and Chemical Industry Conference (PCIC)*. IEEE, 2010, pp. 1–9. URL: https://ieeexplore.ieee.org/abstract/document/5666832/?casa_token=L8Kxd_TPzlkAAAAA:S3vP8cCKUpUvxzjjgSizpv1QAMfJotoXtKH4DCkFwhXFMXVzCsT_0m0Mq6HuRtONJDXW7vpZ6w (visited on 09/25/2024).

[58] "Diagnosis and Fault Tolerance of Electrical Machines, Power Electronics and Drives". In: ed. by Antonio J. Marques Cardoso. Institution of Engineering and Technology, Oct. 19, 2018. ISBN: 978-1-78561-532-0. DOI: 10.1049/PBPO126E. URL: https://digital-library.theiet.org/content/books/po/pbpo126e (visited on 09/07/2024).

[59] Chanseung Yang et al. "Reliable Detection of Induction Motor Rotor Faults Under the Rotor Axial Air Duct Influence". In: *IEEE Transactions on Industry Applications* 50.4 (July 2014), pp. 2493–2502. ISSN: 1939-9367. DOI: 10.1109/TIA.2013.2297448. URL: https://ieeexplore.ieee.org/document/6701218 (visited on 09/08/2024).

[60] *AI Techniques in Induction Machines Diagnosis Including the Speed Ripple Effect*. URL: https://ieeexplore.ieee.org/document/658729 (visited on 09/08/2024).

[61] H. Henao, H. Razik, and G.-A. Capolino. "Analytical Approach of the Stator Current Frequency Harmonics Computation for Detection of Induction Machine Rotor Faults". In: *IEEE Transactions on Industry Applications* 41.3 (May 2005), pp. 801–807. ISSN: 1939-9367. DOI: 10.1109/TIA.2005.847320. URL: https://ieeexplore.ieee.org/document/1433005 (visited on 09/08/2024).

[62] S. Nandi et al. "Selection Criteria of Induction Machines for Speed-Sensorless Drive Applications". In: *Conference Record of the 2001 IEEE Industry Applications Conference. 36th IAS Annual Meeting (Cat. No.01CH37248)*. Conference Record of the 2001 IEEE Industry Applications Conference. 36th IAS Annual Meeting (Cat. No.01CH37248). Vol. 2. Sept. 2001, 1131–1138 vol.2. DOI: 10.1109/IAS.2001.955627. URL: https://ieeexplore.ieee.org/document/955627 (visited on 09/09/2024).

[63] A. Ferrah et al. "The Effect of Rotor Design on Sensorless Speed Estimation Using Rotor Slot Harmonics Identified by Adaptive Digital Filtering Using the Maximum Likelihood Approach". In: *IAS '97. Conference Record of the 1997 IEEE Industry Applications Conference Thirty-Second IAS Annual Meeting*. IAS '97. Conference Record of the 1997 IEEE Industry Applications Conference Thirty-Second IAS Annual Meeting. Vol. 1. Oct. 1997, 128–135 vol.1. DOI: 10.1109/IAS.1997.643018. URL: https://ieeexplore.ieee.org/document/643018 (visited on 09/09/2024).

[64] D.G. Dorrell, W.T. Thomson, and S. Roach. "Analysis of Airgap Flux, Current and Vibration Signals as a Function of the Combination of Static and Dynamic Airgap Eccentricity in 3-Phase Induction Motors". In: *IAS '95. Conference Record of the 1995 IEEE Industry Applications Conference Thirtieth IAS Annual Meeting*. IAS '95. Conference Record of the 1995

IEEE Industry Applications Conference Thirtieth IAS Annual Meeting. Vol. 1. Oct. 1995, 563–570 vol.1. DOI: 10.1109/IAS.1995.530349. URL: https://ieeexplore.ieee.org/document/530349 (visited on 09/09/2024).

[65] A. Stavrou, H. Sedding, and J. Penman. "Current Monitoring for Detecting Inter-Turn Short Circuits in Induction Motors". In: *IEEE International Electric Machines and Drives Conference. IEMDC'99. Proceedings (Cat. No.99EX272)*. IEEE International Electric Machines and Drives Conference. IEMDC'99. Proceedings (Cat. No.99EX272). May 1999, pp. 345–347. DOI: 10.1109/IEMDC.1999.769110. URL: https://ieeexplore.ieee.org/document/769110 (visited on 09/09/2024).

[66] Konstantinos N Gyftakis et al. "A novel approach for broken bar fault diagnosis in induction motors through torque monitoring". In: *IEEE Transactions on Energy Conversion* 28.2 (2013), pp. 267–277.

[67] J. Penman et al. "Condition Monitoring of Electrical Drives". In: *IEE Proceedings B-Electric Power Applications*. Vol. 3. 133. 1986, pp. 142–148. URL: https://www.infona.pl/resource/bwmeta1.element.ieee-art-000004648184 (visited on 09/09/2024).

[68] Andrian Ceban, Remus Pusca, and Raphaël Romary. "Study of Rotor Faults in Induction Motors Using External Magnetic Field Analysis". In: *IEEE Transactions on industrial electronics* 59.5 (2011), pp. 2082–2093. URL: https://ieeexplore.ieee.org/abstract/document/5966340/ (visited on 09/09/2024).

[69] Jose Antonino-Daviu et al. "Evaluation of the Detectability of Rotor Faults and Eccentricities in Induction Motors via Transient Analysis of the Stray Flux". In: *2017 IEEE Energy Conversion Congress and Exposition (ECCE)*. 2017 IEEE Energy Conversion Congress and Exposition (ECCE). Oct. 2017, pp. 3559–3564. DOI: 10.1109/ECCE.2017.8096633. URL: https://ieeexplore.ieee.org/document/8096633 (visited on 09/09/2024).

[70] Galina Mirzaeva, Khalid Imtiaz Saad, and Mohsen Ghaffarpour Jahromi. "Comprehensive Diagnostics of Induction Motor Faults Based on Measurement of Space and Time Dependencies of Air Gap Flux". In: *IEEE Transactions on Industry Applications* 53.3 (May 2017), pp. 2657–2666. ISSN: 1939-9367. DOI: 10.1109/TIA.2016.2628718. URL: https://ieeexplore.ieee.org/document/7744603 (visited on 09/13/2024).

[71] J. Yun et al. "Airgap Search Coil-Based Detection of Damper Bar Failures in Salient Pole Synchronous Motors". In: *2018 IEEE Energy Conversion Congress and Exposition (ECCE)*. 2018 IEEE Energy Conversion Congress and Exposition (ECCE). Sept. 2018, pp. 5791–5796. DOI: 10.1109/ECCE.2018.8557640. URL: https://ieeexplore.ieee.org/document/8557640 (visited on 09/13/2024).

[72] Alamy Limited. *Industrial Electric Motor Isolated on White. 3d Illustration Stock Photo - Alamy*. URL: https://www.alamy.com/industrial-electric-motor-isolated-on-white-3d-illustration-image433670778.html (visited on 09/30/2024).

[73] Konstantinos N. Gyftakis, Panagiotis A. Panagiotou, and Sang Bin Lee. "The Role of the Mechanical Speed Frequency on the Induction Motor Fault Detection via the Stray Flux". In: *2019 IEEE 12th International Symposium on Diagnostics for Electrical Machines, Power Electronics and Drives (SDEMPED)*. 2019 IEEE 12th International Symposium on Diagnostics for Electrical Machines, Power Electronics and Drives (SDEMPED). Aug. 2019, pp. 201–207. DOI: 10.1109/DEMPED.2019.8864863. URL: https://ieeexplore.ieee.org/document/8864863 (visited on 09/10/2024).

[74] Daniel Morinigo-Sotelo et al. "Reliable Detection of Broken Rotor Bars in Induction Motors via MUSIC and ZSC Methods". In: *2016 XXII International Conference on Electrical Machines (ICEM)*. 2016 XXII International Conference on Electrical Machines (ICEM). Sept. 2016, pp. 2881–2886. DOI: 10.1109/ICELMACH.2016.7732932. URL: https://ieeexplore.ieee.org/document/7732932 (visited on 09/13/2024).

[75] Konstantinos N. Gyftakis and Joya C. Kappatou. "The Zero-Sequence Current as a Generalized Diagnostic Mean in Δ-Connected Three-Phase Induction Motors". In: *IEEE Transactions on Energy Conversion* 29.1 (Mar. 2014), pp. 138–148. ISSN: 1558-0059. DOI: 10.1109/TEC.2013.2292505. URL: https://ieeexplore.ieee.org/document/6678694 (visited on 09/11/2024).

[76] Jose A. Antonino-Daviu et al. "Fault Diagnosis in Electric Motors through the Analysis of Currents and Stray Fluxes". In: *2023 International Conference on Electromechanical and Energy Systems (SIELMEN)*. IEEE, 2023, pp. 1–7. URL: https://ieeexplore.ieee.org/abstract/document/10290820/ (visited on 09/13/2024).

[77] S. S. Bhavikatti. *Finite Element Analysis*. New Age International, 2005. URL: https://books.google.com/books?hl=en&lr=&id=YzecxxuNJPwC&oi=fnd&pg=PA2&dq=finite+element+analysis&ots=__eO9KX3E_&sig=wNmIoyWuu3hAZHhTUveLYvRBHp4 (visited on 09/25/2024).

[78] Peter Vas. *Artificial-Intelligence-Based Electrical Machines and Drives: Application of Fuzzy, Neural, Fuzzy-Neural, and Genetic-Algorithm-Based Techniques*. Vol. 45. Oxford university press, 1999. URL: https://books.google.com/books?hl=en&lr=&id=16Ai4r7qjuIC&oi=fnd&pg=PA4&dq=Artificial-Intelligence-Based+Electrical+Machines+and+Drives:+Application+of+Fuzzy,+Neural,+Fuzzy%E2%80%93Neural,+and+Genetic-AlgorithmBased+Techniques&ots=si9ao5mbbk&sig=iI7mDQKhJo_jK1rNkq3l-pD7GX4 (visited on 09/14/2024).

[79] Jian-Ming Jin. *The Finite Element Method in Electromagnetics*. John Wiley & Sons, 2015. URL: https://books.google.com/books?hl=en&lr=&id=DFi-BgAAQBAJ&oi=fnd&pg=PP1&dq=the+finite+element+analysis+method+for+electromagnetic&ots=nIb0v0f7p1&sig=EKD8gDY4lHMS9pDbnHNTG_2FOX8 (visited on 09/14/2024).